

UCSF

UC San Francisco Electronic Theses and Dissertations

Title

Multi-dimensional MR Spectroscopic Imaging of Gliomas at different field strengths

Permalink

<https://escholarship.org/uc/item/37t729mb>

Author

Li, Yan

Publication Date

2008-06-19

Peer reviewed|Thesis/dissertation

Multi-dimensional MR Spectroscopic Imaging of Gliomas at different field strengths

by

Yan Li

DISSERTATION

Submitted in partial satisfaction of the requirements for the degree of

DOCTOR OF PHILOSOPHY

in

Bioengineering

in the

GRADUATE DIVISION

of the

UNIVERSITY OF CALIFORNIA, SAN FRANCISCO

AND

UNIVERSITY OF CALIFORNIA, BERKELEY

Copyright 2008

By

Yan Li

Dedicated to my parents, Renqi Li and Yu Hu,
and my husband, Ji Li

Acknowledgements

To Sarah Nelson, for accepting me as a student of the Bioengineering program, offering me the opportunity to study in her laboratory, being such a wonderful mentor, guiding me on my scientific research, and providing all the advice and encouragement during my Ph.D. studies,

to John Kurhanewicz and Soonmee Cha, for sitting in on my qualifying exam committee, reading my thesis, and teaching me spectroscopy and how to interpret images,

to Dan Vigneron, for being my academic advisor in the Bioengineering program, chairing my qualifying exam, and providing valuable advice and comments on my research,

to Ying Lu, for sitting in on my qualifying exam committee and teaching me statistics,

to Sharmila Majumdar, for sitting in on my qualifying committee,

to Susan Chang, for help with the clinical discussions,

to Esin Ozturk-Isik and Janine Lupo for their friendship, useful discussions on research, and continual support and encouragement all along,

to Duan Xu and Albert Chen, for their help with the sequence development,

to Xiaojuan Li, Michael Lee and Joseph Osorio for helping me adjust to the new lab,

to Mark Albert, for helping me during my qualifying exam,

to Radhika Srinivasan, Helene Retiney, Jason Crane and Eugene Ozhinsky for providing support with my project,

to Inas Khayal, Matt Zierhut, Kate Hammond, Ilwoo Park, Rebeca Choy, Forrest Crawford, Suja Saraswathy, Pieter Pels, Paul Di Camillo, Colleen Mcgue and Wei Bian for being friendly labmates,

to Bert Jimenez and Niles Bruce, for their help with patient scans,

to my parents, Renqi Li and Yu Hu, for their love, encouragement and support,

to my husband, Ji Li, for his love and endless support,

THANK YOU ALL VERY MUCH.

Grant funding for the thesis project was provided by UC Discovery Grant LSIT-10107 and ITL-BIO 04-10148 in conjunction with GE Healthcare, and NIH grants R01 CA059880 and P50 CA97257

Abstract

Multi-dimensional MR Spectroscopic Imaging of Gliomas at different field strengths

by

Yan Li

Proton magnetic resonance spectroscopy (MRS) has been widely used for the assessment of brain metabolites in gliomas. Compared with previous studies that have used 1.5 T and a quadrature head coil, the use of the field strength of 3 T with an 8-channel coil was able to provide an increase in signal-to-noise ratio (SNR) and better spectral resolution. The improved SNR could be used to either decrease acquisition time or improve spatial resolution.

A general marker of brain tumors is the elevation of choline containing compound (Cho) and the reduction of N-acetyl aspartate (NAA). Our study has shown that the variations in metabolite intensity between tumor and normal brain in patients with gliomas are caused by both changes in absolute metabolite concentrations and increases in T_2 relaxation times for Cho and creatine (Cr). Longer T_2 relaxation value of Cho in gliomas means that the ratio of Cho/NAA that is observed in long echo spectra is larger than that in short echo spectra, which suggests that the contrast in metabolite ratios between tumor and normal tissue would be greater at longer echo times.

Although more metabolites are observed at short echo times (<40ms), peak overlap and complex coupling patterns make it difficult to isolate individual components. A J-resolved MRSI sequence with localization in three spatial dimensions was implemented within a clinically feasible scan time at 3 T (23 min). It allows simultaneous detection of Cho, Cr, NAA, glutamate, myo-Inositol and lactate at 3 T, as well as evaluation of T_2 values of singlets.

With the availability of the improved hardware and techniques, in vivo ^1H -MRS can offer new possibilities at the even higher field strength, 7 T. Our study has demonstrated that brain metabolite SNR was improved at 7 T relative to 3 T, but the increase in SNR observed in our initial studies was less than linear with respect to B_0 , primarily due to differences in linewidth. Furthermore, the differences in relaxation times mean that longer TR and shorter TE are needed at 7 T in order to take advantage of the gain in SNR due to increased B_0 .

Table of Contents

Acknowledgements	iv
Abstract	vi
Table of Contents	viii
List of Tables	x
List of Figures	xi
Chapter 1: Introduction	1
Chapter 2: Background	6
2.1 <i>Brain Tumors</i>	6
Neurohistology.....	7
Pathology	8
Treatment	10
2.2 <i>MR Basics</i>	11
NMR Magnetization	11
Excitation and Signal Detection.....	12
Relaxation	13
Localization.....	15
Spin Echo	16
Contrast.....	17
2.3 <i>MRS</i>	18
Principles.....	18
Acquisition of Proton MRS Data.....	21
Data Reconstruction.....	24
Metabolites.....	25
Chapter 3: Considerations in applying 3D PRESS H-1 brain MRSI with an eight-channel phased-array coil at 3 T	31
3.1 <i>Rationale</i>	31
3.2 <i>Methods</i>	33
Simulated Data.....	33
MR Data.....	34
Study Population.....	35
Postprocessing and Analysis.....	36
3.3 <i>Results</i>	38
Chemical Shift Artifact in the Simulation	38
Chemical Shift Artifact in the Phantom.....	39
Coil and Field Strength Comparison.....	41

Field Strength Comparison for Patients.....	42
Comparison of 12x12x8 and 16x16x8 Phase Encoding Arrays	44
3.4 Discussion.....	45
Chapter 4: Comparison of T₁ and T₂ metabolite relaxation times and metabolite concentrations in glioma and normal brain at 3 T	50
4.1 Rationale.....	50
4.2 Methods.....	54
Study population.....	54
MR Data.....	54
Postprocessing and Analysis.....	56
4.3 Results.....	61
Metabolite T ₁ Relaxation times.....	63
Metabolite T ₂ Relaxation times.....	63
Metabolite Levels Corrected for Relaxation Times.....	65
Differences in Metabolite Ratios With & Without Corrections	68
4.4 Discussion.....	69
Chapter 5: Three-dimensional J-resolved H-1 magnetic resonance spectroscopic imaging of volunteers and patients with brain tumors at 3 T.....	76
5.1 Rationale.....	76
5.2 Methods.....	78
Simulated Data.....	78
MR Data.....	78
Study Population.....	80
Postprocessing and Analysis.....	80
5.3 Results.....	84
5.4 Discussion.....	92
Chapter 6: Proton spectroscopy of human brain at 3 T and 7 T comparing of signal-to-noise ratios, spectral linewidths and relaxation times	97
6.1 Rationale.....	97
6.2 Methods.....	98
Study Population.....	98
MR Data.....	99
Postprocessing and Analysis.....	100
Statistics	102
6.3 Results.....	102
6.4 Discussion.....	107
Chapter 7: Summary	111
References.....	115

List of Tables

Table 2.1 WHO classification of glioma	8
Table 2.2 Grading of Astrocytoma	9
Table 2.3 Conditions for different types of weighted imaging.....	17
Table 2.4 Major metabolites observed in proton spectra from the brain.....	26
Table 3.1 SNR of metabolites with an 8-channel coil and a quadrature head coil at 1.5 T and 3 T.	42
Table 4.1 Patient population involved in the study.....	56
Table 4.2 Concentrations of Cho, Cr and NAA as corrected using empirical T_1 and T_2 relaxation times and expressing in mM by QUEST and LCMODEL.	67
Table 4.3 Levels of mI, mIG, Glu and Gln as quantified by QUEST and LCModel.....	67
Table 4.4 Relative metabolite ratios	69
Table 4.5 Normalized metabolite levels	69
Table 5.1 Relative metabolite levels quantified by LCModel without corrections for relaxation times.....	91
Table 5.2 T_2 relaxation times of metabolites (ms) from six volunteers and four primary brain tumor patients.	92
Table 6.1 Methodology and population involved in the study.	98
Table 6.2 T_1 and T_2 relaxation values of Cho, Cr and NAA at 3 T and 7 T.....	102
Table 6.3 SNRs of metabolites at 3 T and 7 T.....	106

List of Figures

Figure 2.1 T_1 (left) and T_2 (right) curves for different types of brain tissues	14
Figure 2.2 The relationship between T_1 and T_2 relaxation and molecular tumbling rate. 14	
Figure 2.3 Refocusing of dephased isochromats with the spin echo sequence.	16
Figure 2.4 T_1 -weighted pre/post-contrast (a, b), T_2 -weighted (c) images from a Grade IV glioma	17
Figure 2.5 spectrum of a molecule with two types of protons and associated probabilities of spin arrangements.	20
Figure 2.6 Diagram of a PRESS sequence.....	22
Figure 2.7 Volume selective 3D CSI based on PRESS	23
Figure 2.8 Normal brain spectra from a 1-cm ³ voxel acquired with PRESS sequence with TE = 35 ms and TE = 135 ms at a TR of 2 s.	25
Figure 2.9 Choline metabolism.....	27
Figure 2.10 Biosynthesis and hydrolysis of phosphatidylcholine.	27
Figure 3.1 The effects of the PRESS selected volumes of resonances corresponding to Cho and NAA with/without VSS and Overpress.....	32
Figure 3.2 H-1 PRESS MRSI applied for studies of chemical shift artifact from a simulation and the phantom.	37
Figure 3.3 Simulation of H-1 PRESS MRSI with different overpress factors..	39
Figure 3.4 The top images were scanned (a) without VSS and with an overpress factor of 1.0, (b) with an overpress factor of 1.2 only, and (c) with 40 mm VSS and an overpress factor of 1.2. The bottom spectra (d) and (e) correspond to the top images (a) and (c), respectively.	40
Figure 3.5 Chemical shift artifact observed with an 8-channel coil at 1.5 T (left) and 3 T (right), with/without 40 mm VSS and an overpress factor of 1.2 measured in a uniform phantom.....	41
Figure 3.6 MRSI for a patient with a Grade IV glioma at the same noise scale for acquisitions at 1.5 T (left) and 3 T (right).....	43

Figure 3.7 SNR of metabolites with an 8-channel coil at 1.5 T and 3 T from the normal voxels of eight primary brain tumor patients.....	44
Figure 3.8 (a) MRSI data from a glioma patient with (b) 16x16x8 and (c) 12x12x8 phase encoding array.....	45
Figure 4.1 The influence of spin-echoes on spin-spin coupling as illustrated for the coupled spins A and X when both spins experience a 180° pulse (a) and when only spin A experiences a 180° pulse (b).....	51
Figure 4.2 2D J-resolved spectra for a molecule with two types of protons.	52
Figure 4.3 Comparison of Glu detection with conventional PRESS and TE-averaged PRESS at 3 T	53
Figure 4.4 Simulation of TE-averaged PRESS spectra of Glu (black) and Gln (grey) with different T ₂ relaxation times..	59
Figure 4.5 Single voxel 2D J-resolved spectra acquired from a volunteer and a GBM patient.....	62
Figure 4.6 T ₂ relaxation times of metabolites (ms).....	64
Figure 4.7 TE-averaged spectra quantified by LCModel (middle row) and QUEST (third row) corresponding to the image in a volunteer (a), Grade III (b) and Grade IV (c) patients.	65
Figure 4.8 Scatter plots of Cho, Cr and NAA calculated from LCModel vs. QUEST for all the voxels in the study. Metabolite concentrations on x-axis represent those from LCModel, while y-axis for the same spectra quantified by QUEST.	66
Figure 4.9 Metabolite concentrations of Cho, Cr and NAA quantified by LcModel and QUEST after T ₁ and T ₂ corrections for each class.	66
Figure 5.1 Flyback echo-planar trajectory	77
Figure 5.2 Glu and Gln simulation using GAMMA along with the increase of TE.....	83
Figure 5.3 Simulated (a) and phantom (b) TE-averaged PRESS spectra of Glu (black) and Gln (grey).....	84
Figure 5.4 Single voxel 2D J-resolved spectra from a 100 mM Lac phantom with two localizations.	85
Figure 5.5 3D J-resolved MRSI acquired from the head phantom.	86

Figure 5.6 The TE-averaged spectrum of a standard head phantom along with the spectra of metabolic phantoms.....	87
Figure 5.7 3D J-resolved MRSI acquired from a volunteer.....	89
Figure 5.8 3D J-resolved MRSI acquired from a patient with glioma.....	90
Figure 5.9 T ₂ maps of Cho, Cr and NAA from a volunteer.....	92
Figure 6.1 2D J-resolved spectra acquired at 3 T (left) and 7 T (right).....	103
Figure 6.2 T ₂ fits for Cho, Cr and NAA data from a volunteer acquired at 7 T using mono-exponential function.	104
Figure 6.3 Representative T ₁ -dependent spectra acquired using spectral-spatial pulse at TE of 90 ms (right) and the corresponding voxel location (top left) from a volunteer. .	105

Chapter 1: Introduction

It is estimated that 43,800 new cases of primary brain and central nervous system tumors are diagnosed in the United States in 2005 [1]. Gliomas, which are derived from the glial cells, account for the majority of primary brain tumors, and vary from benign to malignant. Among all the gliomas, Grade IV gliomas or Glioblastoma Multiforme (GBM) are both the most common and the most malignant, with average survival of one year. While low grade gliomas have a better prognosis, they often undergo a malignant transformation during the development of recurrence. Both primary and recurrent malignant gliomas infiltrate the adjacent brain tissue, and recurrence typically occurs within 2 cm of the original tumor site. The primary therapies for gliomas include surgical resection, radiation therapy, and chemotherapy. Proper diagnosis and grading, correct localization and appropriate characterization of brain tumors are of a great importance for all phases of treatment planning and selection.

Magnetic resonance imaging (MRI) is a non-invasive clinical modality for detecting and evaluating brain tumors due to its superior ability to generate contrast within soft tissues. Conventional MRI that is used to investigate the patients includes T_1 -weighted and T_2 -weighted images. The lesion is hyperintense in T_2 -weighted images and hypointense in T_1 -weighted images because its water content is higher than in normally myelinated white matter. The T_2 hyperintense lesions may encompass active tumor but fail to distinguish it from edema, gliosis, inflammation and cyst. The use of intravenous paramagnetic contrast, such as gadolinium diethyltriamine penta-acetic acid (Gd-DTPA),

is also commonly used in an attempt to differentiate active tumor from edematous regions. Unfortunately the hyperintense lesions in post-contrast T₁-weighted images only represent the regions where blood-brain barrier (BBB) is compromised and may not include all of the tumor. In practice, low grade gliomas rarely enhance because BBB remains intact. Thus, additional methods are needed to identify the tumor regions and to define the presence and extent of the brain tumors.

Proton magnetic resonance spectroscopy (MRS) is a powerful noninvasive tool for investigating normal and abnormal metabolism. In vivo single-voxel ¹H-MRS and multi-voxel magnetic resonance spectroscopic imaging (MRSI) have been shown to be of value in the application of brain tumors for assessing the spatial extent and metabolic characterization of primary brain tumors [2-7]. Biochemical profiles of brain tumors for the major metabolites have been studied previously [8-10]. Choline containing compounds (Cho), creatine (Cr), N-acetyl aspartate (NAA), lactate (Lac) and lipid (Lip), which are observed in spectra acquired with long echo times (~100 ms), are important metabolic markers. A general marker of brain tumors is the elevation of Cho, which is due to increased membrane synthesis in neoplasms, and the reduction of the neuronal marker NAA. The CNI (Cho/NAA index) allows comparison between subjects and has been used to identify the spatial extent of the metabolic abnormality in brain tumors [11]. Furthermore, Cr reflects cellular bioenergetics; Lac is a marker of anaerobic metabolisms; and Lip, likely a marker of necrosis, is highly associated with high-grade tumors. These markers together have been used in the investigation of diagnosis, grading, therapy and prognosis for patients with brain tumor. Although more signals can be detected in spectra with short echo time but peak overlap may make it difficult to isolate individual

components, even at 3 T. Specific spectra-editing sequences for the unobstructed detection of these metabolites with complex coupling, such as glutamate (Glu), glutamine (Gln) and myo-inositol (mI), have been most commonly studied nowadays and have been utilized to evaluate the impacts of these metabolites in the diseases.

Although ratios of metabolites to Cr or to normal tissue from the same patient are widely considered, the question arises as to whether the changes in patients are really due to altered tissue concentrations or different metabolite relaxation times. Because of the restrictions on clinical scan time, the repetition time (TR) of spectral acquisition is often set at 1~2 s, which does not allow full relaxation of metabolites and results in signal saturation. Signals for metabolites with relatively short T_2 relaxation times weight the signal decay in the long TE acquisitions differently. Correcting for the losses in relaxation times is important for metabolite quantification.

With the availability of the improved hardware and techniques, in vivo MRS has been performed at higher field strengths, which offer the potential of higher signal-to-noise ratio (SNR) and improved spectral resolution. In addition, the use of the multi-channel radiofrequency coils also provide the additional raise in SNR, which is because each coil element only detects tissue noise from a limited tissue volume and that the signals can be combined to provide an extended spatial coverage. The reconstruction for the combined data requires an acquisition of the calibration sequence to obtain estimates of coil sensitivities. The increased SNR benefited from both higher field strengths and multi-channel coils could be utilized to provide finer spatial resolution or larger coverage with the same acquisition time, or reduce the total acquisition time. Other possibilities at

high field are to use the improved spectral resolution to obtain more reliable quantification and improved detection of metabolites other than Cho, Cr and NAA.

This study has been focused on the development, optimization and application of acquisition, post-processing, and quantification methods for in vivo MRS data with the objective of increasing the information that can be obtained from patients with brain tumors using this non-invasive technique in conjunction with conventional MR imaging. This has included the assessment of advantages in making a transition to new hardware using higher field strength and new radiofrequency coils, implementation of new proton spectroscopy acquisition methods and understanding how metabolite levels differ in tumors relative to normal tissue. This thesis is organized as follows:

Chapter 2 provides a brief overview of relevant background on brain tumors and the basis of MR techniques, as well as presenting the current MRS acquisition, processing and quantification techniques;

Chapter 3 describes the benefits of a 3 T scanner and an 8-channel phased array head coil for acquiring 3-D point resolved spectral selection (PRESS) H-1 MRSI data from the brain of volunteers and patients with brain tumors relative to those using 1.5 T and a quadrature head coil [12]. Issues that were of concern included differences in chemical shift artifacts, line broadening due to increased susceptibility at the higher field strengths, and the increased complexity of the post-processing software due to the need for combining signals from the multi-channel data.

Chapter 4 discusses metabolite characteristics based on the longitudinal and transverse relaxation times of singlets, such as Cho, Cr and NAA, and metabolite concentrations in

gliomas using single voxel 2D J-resolved PRESS sequence, and examines the importance of the correction of relaxation times for absolute metabolite quantification [13];

Chapter 5 introduces new acquisition and post-processing methods for interpretation of 2D J-resolved PRESS MRSI data with three spatial dimensions and develops strategies for improving the quantification of metabolites from these spectra by using prior information concerning the J-coupling of metabolites such as Glu, mI and Lac, as well as obtaining T_2 values of Cho, Cr and NAA [14];

Chapter 6 compares the spectra acquired at 3 T with those at 7 T on SNR, spectral linewidth and relaxation times, and details the parameters that may comprise the data quality for the spectra acquired at higher field [15];

Chapter 7 summarizes the major results of this study and proposes future studies.

Chapter 2: Background

This chapter reviews the basic characterization of brain tumors, specially the primary gliomas, which is the main subject in this project. It is then followed by the basic MR techniques, as well as MRI and MRS principles for the studies in the patients with primary brain tumors.

2.1 Brain Tumors

The brain is the control center of the whole body and is responsible for all kinds of behaviors. The cerebrum is divided into four lobes, designated as frontal, parietal, occipital and temporal, based upon prominent gyri, which refer to bugles or eminences on the surfaces of cerebral cortex, and sulci, the spaces separating the gyri. Cerebral lobes are not only anatomically different, but also vary in functional elements, which could assist in establishing functional localization through empirical observation in clinic resulting from mass effects in patients with primary brain tumors. The incidence rate of all primary brain and central nervous system (CNS) tumors including non-malignant and malignant ones is about 15 cases per 100,000 person every year [1]. Of all, gliomas are the most common type. In this section, we are going to first discuss the brain neurohistology, followed by pathology and classification of brain tumor, and then present the current treatments.

Neurohistology

The principle cells in the CNS are neurons and glial cells. Neurons are typically composed of a cell body, a dendrite and an axon. The axons of neurons in the brain are myelinated by oligodendrocytes and are a major component of white matter. The cell bodies of neurons are in the gray matter. Glial cells, which serve as connective tissues in the nervous system, provide an interface between neurons and brain fluids. There are four main types of glial cells in the CNS, including astrocytes, oligodendrocytes, microglia and ependymal cells. Glial fibrillary acidic protein (GFAP) is a marker for astrocytes. Astrocytes project foot processes which attach to the basement membrane of blood capillaries, neurons and synapses. They are important in controlling the microenvironment of nerve cells and maintaining the integrity of the blood-brain barrier (BBB). The BBB is an anatomic and physiologic separation of blood from the CNS extracellular fluid and blocks all molecules except glucose and amino acids that cross cell membrane by means of diffusion and active transportation. Oligodendrocytes are the myelin-forming cells in the CNS. One oligodendrocyte can myelinate many axons of neurons. Microglia is derived from monocytes and functions as a phagocyte. Ependymal cells are the ciliated cells that line the ventricles of the brain and the choroids plexus, a specialized structure that secretes cerebrospinal fluid (CSF). The CSF is a colorless acellular fluid. It flows through ventricles into the subarachnoid space, and ultimately absorbed by arachnoid villi into the superior sagittal sinus. It protects the CNS from concussive injuries, transports hormones and removes the wastes. Tight junctions between the epithelial cells of the choroids plexus form the blood-CSF barrier.

Pathology

Neoplasms of the brain include primary and metastatic tumors with the primary tumors accounting for two-thirds of them. The World Health Organization (WHO) classified primary tumors of the nervous system into five categories including tumors from neuroepithelial tissue, peripheral nerves, meninges, lymphocytes and hemopoietic cells and the sellar regions [16]. Glioma is a type of neuroepithelial tumors that makes up 40% of primary brain tumors [1].

Grades of Gliomas

Gliomas are derived from glial cells and include astrocytomas, oligodendrogliomas and mixed gliomas, such as oligoastrocytomas, and ependymomas. They are further categorized according to grade. The WHO classification as illustrated in Table 2.1 is the most common grading system. The incidence of gliomas varies through the age. Low-grade gliomas (Grade II) peak in young adults, while high grade gliomas (Grade III and Grade IV) are predominant in older patients.

Table 2.1 WHO classification of glioma

WHO Grade	WHO Designation
I	Pilocytic astrocytoma, Subependymal giant cell astrocytoma, Pleomorphic xanthoastrocytoma, Subependymoma
II	Astrocytoma, Oligoastrocytoma, Oligodendroglioma, Mixed oligoastrocytoma, Ependymoma
III	Anaplastic astrocytoma, Anaplastic oligodendroglioma, Anaplastic oligoastrocytoma, Anaplastic ependymoma
IV	Glioblastoma Multiforme (GBM)

Astrocytomas are the most common type of gliomas and are graded based on microscopic appearance of astrocytomas by the St. Anne-Mayo (SAM) criteria, given in

Table 2.2. This is based on the presence or absence of four histologic features: nuclear atypia, mitosis, vascular proliferation and necrosis [17]. The SAM grading method is adapted to the WHO classification and correlates with survival rate. Pilocytic astrocytomas, classified as a WHO Grade I astrocytoma, are the most common brain tumors of the posterior fossa in children. They are benign and rarely undergo neoplastic transformation. Low-grade astrocytomas, Grade II astrocytoma, have the best outcome of all the infiltrative astrocytomas with a median survival of 5 to 10 years, whereas Glioblastoma Multiforme (GBM) which makes up 50% of gliomas is the most malignant with a median survival of only 9 to 12 months.

Table 2.2 Grading of Astrocytoma

WHO Grade	WHO Designation	Histologic Criteria (St. Anne-Mayo)
I	Pilocytic astrocytoma	Not applicable
II	Astrocytoma	One criterion: usually nuclear atypia
III	Anaplastic astrocytoma	Two criteria: usually nuclear atypia and mitosis
IV	Glioblastoma Multiforme (GBM)	Three or four criteria: nuclear atypia, mitosis, vascular proliferation, and/or necrosis

Oligodendrogliomas are more common in adults and men. They often histologically mixed with cells that are morphologically astrocytic and are then termed as mixed oligoastrocytoma. The combination of 1p/1q deletion in oligodendrogliomas is a significant predictor of overall survival, and is also correlated with marked chemosensitivity and prolonged recurrence-free survival. Despite being clinically less aggressive than other gliomas, oligodendrogliomas have a tendency to grow into the surrounding brain tissue and are often more difficult to remove surgically.

Ependymomas are rare tumors and account for 4-6% of all primary brain and CNS gliomas. They mainly affect subjects up to at age of 20 years old and are the third most common histologic type of brain tumors in children. Ependymoma may cause significant swelling of the ventricle or hydrocephalus, resulting in nonspecific symptoms of increased intracranial pressure (ICP). In general, around half of the patients that are diagnosed as ependymoma live for at least five years.

Treatment

Neurosurgical therapy, radiation therapy (RT) and chemotherapy are three standard types of treatments for brain tumors.

Surgery is usually the first step of the treatment plan. The goal here is to decrease the tumor burden, minimize symptoms, as well as preserving brain functions. However, gliomas are infiltrative in nature and often localize close to a critical structure, which makes it impossible for total resection and leaves behind significant residual tumors.

Ionizing radiation damages the tumor cell's DNA, and is commonly used directly after surgery. The normal tissues surrounding the tumor lesion have a limited tolerance to radiation which restricts the dose that can be applied and hence limits its effectiveness. Tumor cells also tend to be hypoxic due to the outgrowth of their blood supply, which makes them resistant to radiation.

Chemotherapy can be given before surgery to reduce the tumor burden or after surgery to destroy the remaining tumor cells. In a recent study, the combination of Temozolomide (TMZ) with RT has been shown to significantly improve survival time in newly diagnosed GBM compared to those with RT alone [18].

2.2 MR Basics

Magnetic resonance imaging (MRI) is an important diagnostic imaging technique that is routinely applied in clinical setting. MRI is based on the phenomena called nuclear magnetic resonance (NMR) that was discovered in the 1930's by Isidor Rabi. Felix Bloch and Edward Mills Purcell further extend this technique into the use on liquids and solids in 1946, for which they shared the Nobel Prize in physics in 1952. The first whole-body MRI scanner was completed in 1977 by Raymond Damadian. The number of MRI scanners in a clinical environment is now estimated to be over 20,000 and more than million MRI examinations are performed every year. In this section, we present the basic concepts of MR, including magnetization, excitation, signal detection, relaxation, localization techniques and image contrast.

NMR Magnetization

NMR is based on the interaction between atom and an external magnetic field. The nucleus has an intrinsic *nuclear spin* or *nuclear spin angular momentum*, J , which is the vector sum of the *nuclear spin quantum number*, I . The spin quantum number takes on multiples of $\frac{1}{2}$ values and can + or – such that

$$I = 0, \pm\frac{1}{2}, \pm 1, \pm\frac{3}{2} \dots \quad (2.1)$$

Nuclei with zero spin angular momentum are NMR-inactive. For NMR spectroscopy of biomolecules, the most important nuclei with $I = \frac{1}{2}$ are ^1H , ^{13}C , ^{15}N and ^{31}P . Because of its natural and biological abundance, protons are widely used to obtain signals for imaging.

Nuclei with nonzero spin angular momentum also possess *nuclear magnetic dipole moments* or *magnetic moments*, μ , as defined by

$$\mu = \gamma I \quad (2.2)$$

in which γ , gyromagnetic ratio, is a characteristic constant for a given nucleus. When placed inside an external magnetic field B_0 , the spins precess about B_0 at the frequency of

$$\omega_0 = \gamma B_0 \quad (2.3)$$

which is known as the Larmor frequency, and the spin vectors align themselves with B_0 . Therefore, spins at different orientation have different energy interaction with B_0 given by

$$E = -\mu \cdot B_0 \quad (2.4)$$

This results in $2I+1$ equally spaced energy levels, which are known as the *Zeeman levels*. At equilibrium, the different energy levels are unequally distributed because more spins occupy the low-energy level. The relative population is given by the *Boltzmann distribution*. The transition between two energy levels can be stimulated by electromagnetic radiation and the energy difference is

$$\Delta E = \gamma \hbar B_0 \quad (2.5)$$

which is proportional to B_0 . The frequency of the electromagnetic radiation is exactly the Larmor frequency ω_0 , also known as the resonant frequency.

Excitation and Signal Detection

The *bulk magnetic moment*, M , is the vector sum of magnetic momentum μ and describes the collective behavior of a spin system under an external magnetic field B_0 . At thermal equilibrium, the small population excess in the lower energy level gives rise to M_0 along

with B_0 , but no net magnetization in the transverse component because of random phases of the individual magnetic momentum. On the application of radiofrequency (RF) pulse (B_1 field) perpendicular to the B_0 field, the bulk magnetic moment is turned towards the transverse plane. The angle between B_0 and M is called flip angle, and is determined by

$$\alpha = \gamma B_1 \tau \quad (2.6)$$

where τ represents the length of time that the B_1 field is applied. The excitation frequency ω_{rf} is determined by the resonance condition. Immediately after the application of the RF pulse, the bulk magnetic moment starts to precess at its Larmor frequency. Based on the Faraday's Law of electromagnetic induction and the principle of reciprocity, this rotating magnetization could be detected as a weak oscillating voltage by the receiver coil surrounding the sample. This electrical signal is the so-called NMR signal.

Relaxation

When the RF pulse is turned off, the spin system will re-establish its equilibrium, referred as relaxation, through the interaction with the thermal molecular environment. Relaxation rates depend on a large number of factors, including overall rotational correlation times, internal molecular motions and magnetic field. Figure 2.1 shows the longitudinal and transverse relaxation curves using the values from different human brain tissues [19, 20].

The longitudinal relaxation time, or spin-lattice relaxation time, T_1 , is the time for magnetization to return to 63% of its original length. It describes the overall loss of energy from excitation, which is transferred into the surroundings in the form of heat. T_1 relaxation is fastest when the motion of the nucleus (tumbling rate) matches that of the Larmor frequency as illustrated in Figure 2.2. Thus higher magnetic fields are associated

with longer T_1 times. The difference between the tumbling rate of macromolecules and ω_0 is smaller than that of metabolites, which means that T_1 times are relatively longer in metabolites.

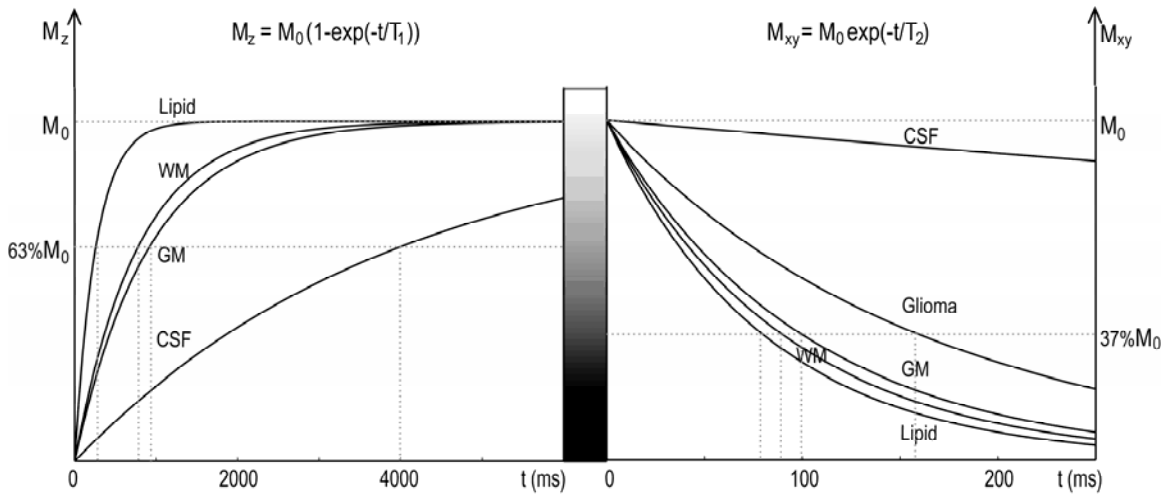


Figure 2.1 T_1 (left) and T_2 (right) curves for different types of brain tissues

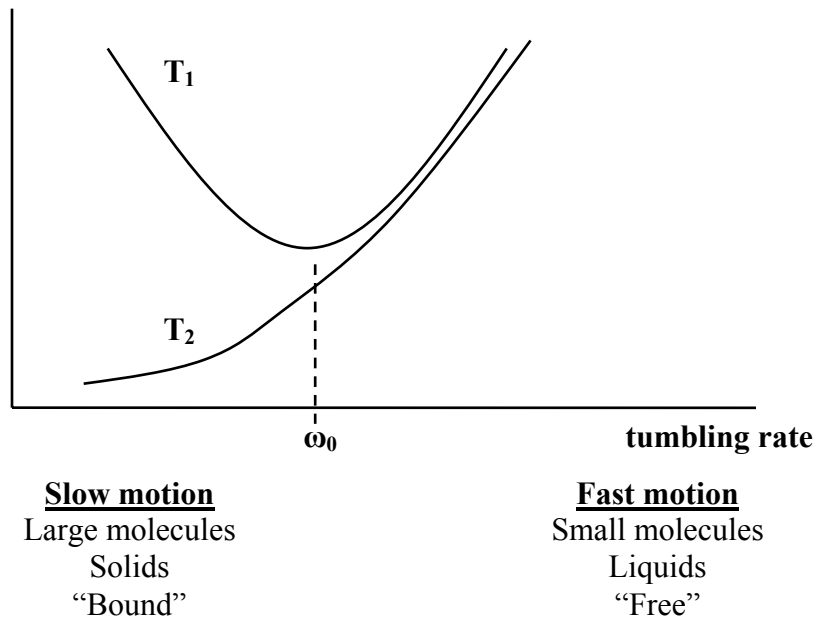


Figure 2.2 The relationship between T_1 and T_2 relaxation and molecular tumbling rate.

The transverse relaxation time, or spin-spin relaxation time, T_2 , is the time for the transverse magnetization to decay 37% of its initial value. The energy transfers from spins to spins rather than being lost to the surrounding lattice, which results in the loss of the transverse component. As the natural motional frequency of the protons increases, T_2 is prolonged (Figure 2.2). Thus T_2 values reflect the restriction of molecular motion of the spin. The decay of the transverse magnetization following a 90° RF pulse is determined by T_2^* , which accounts for the effects of both T_2 decay and inhomogeneities. Thus biological macromolecules have short T_2 and broad linewidths.

Localization

For a spatially heterogeneous object, localization is required to differentiate its origin and is typically achieved by using three orthogonal linear gradients through slice selection, frequency encoding and phase encoding. A frequency selective RF pulse with a central frequency ω_0 is applied simultaneously with a linear gradient to excite a slice of tissue. The thickness of the selective slice is defined as

$$\Delta z = \frac{BW_{rf}}{\gamma G_z / 2\pi} \quad (2.7)$$

where BW_{rf} is the bandwidth of the RF pulse and G_z is the gradient strength on the z direction. After the slice selection, the other two dimensions are spatially encoded by applying a phase-encoding gradient which generates a linear spatial phase variation and applying a frequency-encoding gradient during the signal readout which creates a linearly varying precession frequency across the object. Repetitive excitations with varying phase-encoding strength at the same frequency encoding gradient result in the sampling

of k-space with multiple lines parallel to the frequency-encoded dimension, which is then transformed back into spatial domain via Fourier Transform (FT).

Spin Echo

Spin echo is one of the fundamental building blocks of numerous NMR experiments. It is produced by the two RF pulses, consisting of a 90° excitation pulse and 180° refocusing pulse. As illustrated in Figure 2.3, spin echo sequence reverses the dephasing resulting from magnetic field inhomogeneities, susceptibility and chemical shift, which cause spins precess with different precession frequency.

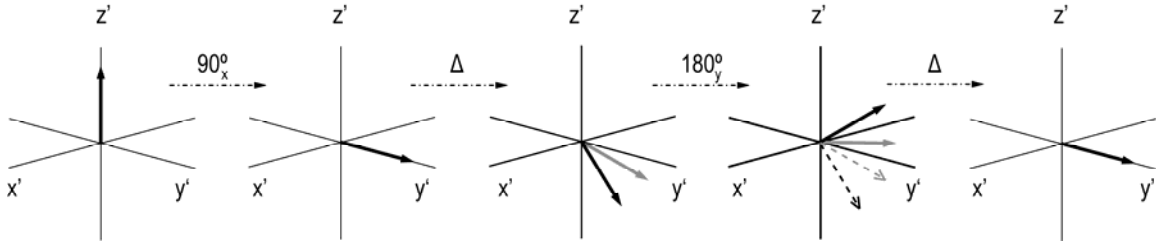


Figure 2.3 Refocusing of dephased isochromats with the spin echo sequence.

The time that the echo forms, 2Δ in Figure 2.3, is called the echo time (TE), and the time between two consecutive 90° RF pulses is called repetition time (TR). The signal intensity of the spin system is described by

$$S = \rho \left(1 - e^{-TR/T_1} \right) e^{-TE/T_2} \quad (2.8)$$

where ρ is the density of the spin population. Since the amplitude of a spin echo is T_2 -weighted, it is useful for generating image contrast and estimating T_2 values.

Contrast

As shown in Figure 2.1, the T_1 and T_2 relaxation times differ in different type of normal tissues and healthy and diseased section of the same tissue, which makes it is possible differentiate the tissue type. According to Equation (2.8), the image contrast could be generated for T_1 -weighted, T_2 -weighted and proton density-weighted images by varying pulse sequence parameters, such as TE and TR (Table 2.3).

Table 2.3 Conditions for different types of weighted imaging

TR	TE	Imaging weighting
Short	Short	T_1 -weighthed
Long	Long	T_2 -weighted
Long	Short	Proton density-weighted

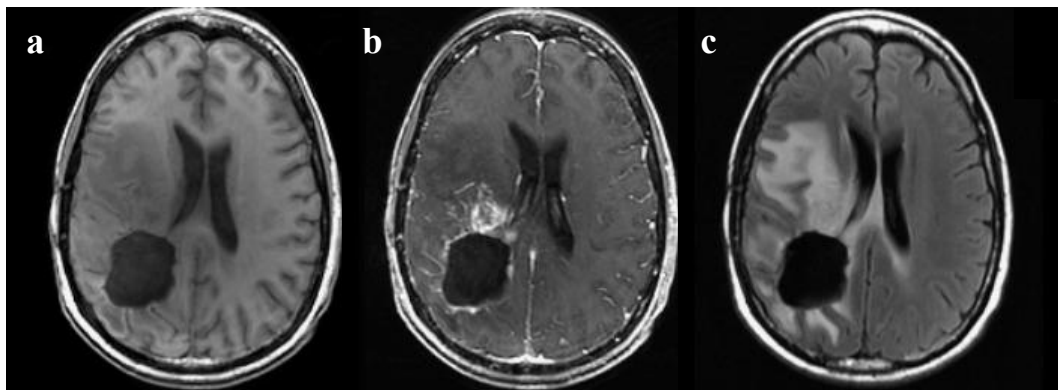


Figure 2.4 T_1 -weighted pre/post-contrast (a, b), T_2 -weighted (c) images from a Grade IV glioma

A typical MR exam for brain tumor patients includes pre- and post-contrast T_1 -weighted and T_2 -weighted images (Figure 2.4). The gadolinium diethyltriamine pentaacetic acid (Gd-DTPA) is a paramagnetic contrast agent that shortens both T_1 and T_2 values of tissues but the T_1 shortening effect is dominant. It causes high signal intensity

on T₁-weighted image where the BBB is absent or broke down, which is commonly seen in high grade gliomas. Lesions with longer T₂ are brighter in T₂-weighted image, however, these T₂ hyperintense lesions fail to distinguish among edema, gliosis, inflammation, cyst and active tumors.

2.3 MRS

Both MRI and MR spectroscopy (MRS) are applications of the NMR phenomenon, but MRI is primarily based on signal coming from protons in water while MRS is obtained by differentiating chemical composition of small metabolites. Over the years, in vivo MRS has been applied using various nuclei, such as ¹H, ³¹P and ¹³C, in different types of organs at a variety of magnetic field strengths (1.5, 2, 3, 4 and 7 T). When MRS is combined with methods for spatial localization such as volume selection and phase encoding, it is able to provide biochemical information that can be directly correlated with regions of the anatomy as depicted by conventional MR images. In this section, we describe the principles, data acquisition, data reconstruction and major metabolites in the brain.

Principles

The MR spectrum detects a collection of spin interactions, including chemical shift and spin-spin coupling or J-coupling. The chemical shift indicates the local electronic environment, and J-coupling provides a direct spectral manifestation of the chemical

bond. These interactions allow us to differentiate different molecules and hence study changes in the chemical composition of different substances.

Chemical Shift

Under an external magnetic field, NMR theory predicts that the spins precess about B_0 at the Larmor frequency (Equation 2.3), which depends on gyromagnetic ratio and external field strength. In practice, a spin system may have a range of resonance frequencies. This phenomenon is due to chemical shift effects. In the presence of an external magnetic field, the negative-charged electrons also interact with the field and can vary the local magnetic fields on a submolecular distance scale by either shielding or deshielding. As a result, the effective magnetic field that a nucleus experiences is

$$B_i = B_0(1 - \sigma_i) \quad (2.9)$$

where σ_i is a chemical shield term caused by the electrons that oppose or shield the external magnetic field. According to the Larmor equation, the resonance frequency for the nucleus is

$$\omega_i = \gamma B_0(1 - \sigma_i) \quad (2.10)$$

This indicates that the resonant frequency is dependent on its molecular environment and external field strength. To report chemical shifts without the effects of magnetic field strength, a parts per million (ppm) scale is introduced, defined by

$$\delta_i = \frac{\omega_i - \omega_{ref}}{\omega_{ref}} \times 10^6 \quad (2.11)$$

In a proton system, tetramethylsilane (TMS) is used for the chemical shift δ reference ω_{ref} and assigned a value of $\delta = 0.0$ ppm. TMS exhibits greater shielding than most other

organic molecules and its peak does not interfere with other common peaks. Effects that influence chemical shift include pH and temperature.

Spin Coupling

Previously we have stated that the chemical shift is caused by the electrons surrounding the nucleus. The bonding electrons between the nuclear spins can also influence each other's effective magnetic field. This phenomenon is called spin-spin coupling or J-coupling. It describes an interaction between electrons and the adjacent nucleus through a small number of chemical bonds. This effect is observable if the distance is less than or equal to three bond lengths, this effect is observable.

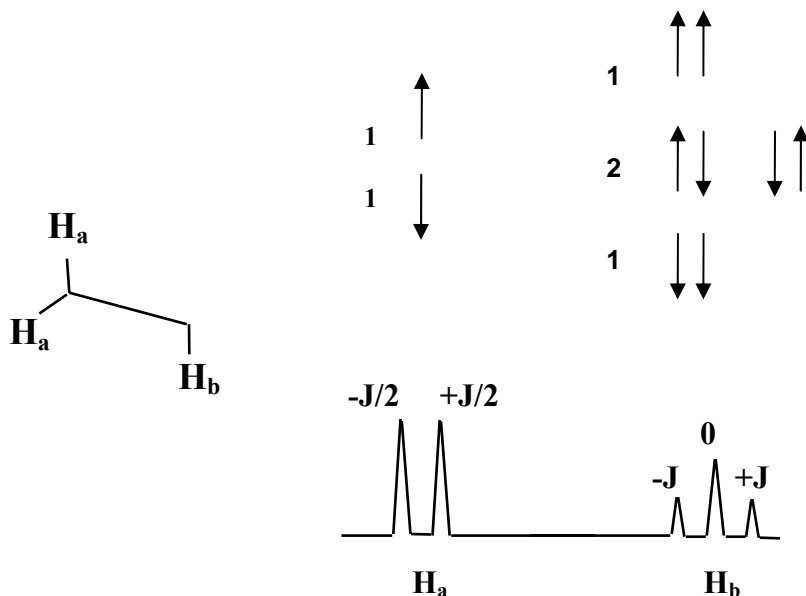


Figure 2.5 spectrum of a molecule with two types of protons and associated probabilities of spin arrangements.

Unlike chemical shift, the J-coupling is independent of the applied magnetic field. For a spin $\frac{1}{2}$ system, such as protons, each can have one of two possible spin orientations in the applied field, either spin-up or spin-down, thus the magnetic field sensed by the adjacent protons can have one of two possible values. This results in the observation that n protons will split the adjacent protons into (n+1) peaks. An example of a molecule with three spin $\frac{1}{2}$ nuclei, one type A and two type B, is shown in Figure 2.5.

Acquisition of Proton MRS Data

MRS measures the localized signals coming from small metabolites with concentrations tens of thousands of times smaller than that of water and lipid, which makes sensitivity and signal-to-noise ratio (SNR) critical for such acquisition. A single-voxel or multiple-voxel MR spectroscopy pulse sequence consists of water suppression, out volume suppression and localization techniques.

Localization

Localization distinguishes the signal from within a volume of interest (VOI) with minimal contribution from outside of the defined volume. Point resolved spectral selection (PRESS) is one localization technique that has commonly been used to obtain MRS data [21]. Three slice-selective RF pulses, 90° - 180° - 180° , excite three intersecting orthogonal planes and pulse sequence diagram is illustrated in Figure 2.6. Other localization techniques for spectroscopy acquisition include stimulated echo acquisition mode (STEAM) and image-selected in vivo spectroscopy (ISIS).

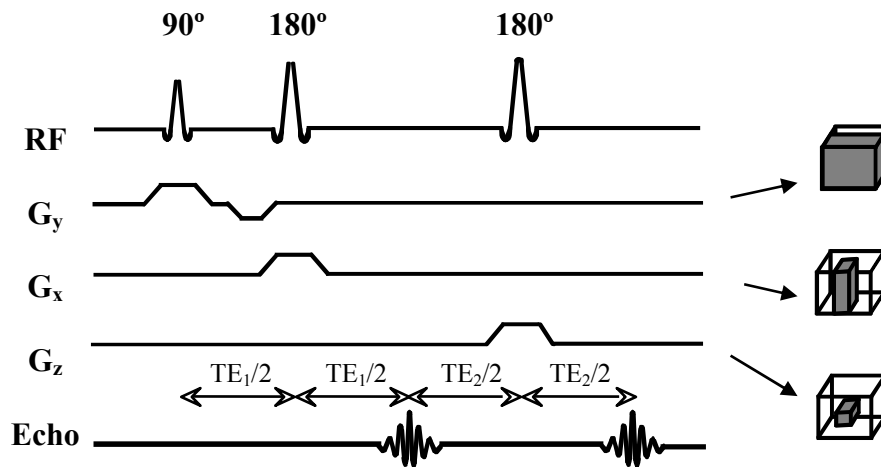


Figure 2.6 Diagram of a PRESS sequence.

Water and Lipid Suppression

Since the concentration of water is much higher than that of small metabolites, it is necessary to suppress the predominant water signals and thus makes it easy to observe weak signals from metabolites. Water suppression is most commonly achieved by eliminating the water signal prior to excitation and collection of the metabolite signals, such as chemical shift selective (CHESS) pulse. CHESS destroys the water signal by means of a spectral selective 90° pulse and followed by a dephasing pulse [22]. Multiple repetitions of CHESS pulses that are frequently used in practice can produce a better water suppression [23]. BASING (band selective inversion with gradient dephasing) pulse is a more improved technique using the frequency selective RF Basing 180° pulse for both water and lipid suppression [24]. Another way for water suppression is to only excite the frequency of interest, such as spectral-spatial pulses [25] with the metabolites of interest only in the pass band and water/lipid in the stop band.

To eliminate unwanted lipid signals from outside the VOI and preserve the metabolic information, outer volume saturation (OVS), saturation bands that surround the excitation volume and especially cover these regions that contain high lipid, is commonly used [26]. Compared with traditional OVS, very selective suppression (VSS) that was used in this project offers larger excitation bandwidth and narrow transition bands. These benefit for better lipid suppression, less chemical shift artifact and sharpen the edges of the PRESS-selected box [27].

Chemical Shift Imaging

Chemical shift imaging (CSI), also referred to magnetic resonance spectroscopic imaging (MRSI), is a method that collects spectroscopic data from multiple adjacent voxels within a large VOI.

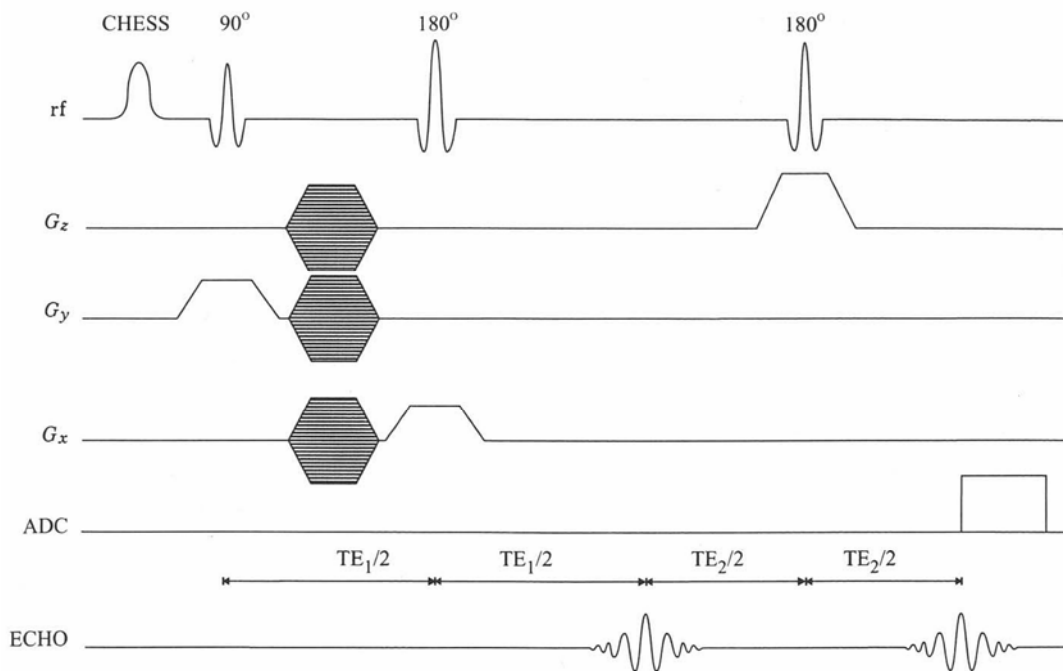


Figure 2.7 Volume selective 3D CSI based on PRESS

Spatial localization is mostly done by phase encoding in one, two or three dimensions. Figure 2.7 is a simplified sketch of a 3D CSI sequence using PRESS localization.

The most recent innovation in spectroscopic imaging techniques is the implementation of fast CSI sequences, which evolved from concepts related to spatial encoding when sampling an MR signal during the readout. Echo planar spectroscopic imaging (EPSI) sequences were applied in this project and will be described in a later chapter.

Data Reconstruction

The MR signal which is acquired in time domain is termed as free induction decay (FID) and requires a number of processing steps to present a useful spectrum with interpretable biochemical information. The data processing is initiated with offset correction, apodization and zero filling in the time domain. The time domain data are then transformed into the frequency domain using a Fast Fourier Transform (FFT), and k-space transforms are applied to generate a 3D array of spectra in the spatial domain. Following Fourier Transform (FT), frequency/phase corrections, baseline correction and estimation of peak heights or peak areas are performed in the frequency domain. The spectroscopic data in this project was processed using in-house software [28]. To obtain absolute quantification of metabolites concentration, it is necessary to correct for the effects of T_1 and T_2 values. The automated procedures for absolute quantification that were used in this project include LCMoDel (linear combination of Model) package [29]

and QUEST (quantitation based on quantum estimation) quantitation algorithm [30] and describe in a later chapter.

Metabolites

An example of ^1H MRS of in vivo normal human brain from a 3 T MR scanner is illustrated in Figure 2.8. The major metabolites that are observed in long echo time (~ 100 ms) include choline-containing compounds (Cho), creatine (Cr), N-acetyl aspartate (NAA), lactate (Lac) and lipid (Lip). Shorter TE sequences (~ 35 ms) yield additional information from metabolites with short T_2 , such as glutamate (Glu), glutamine (Gln), myo-Inositol (mI) and glycine (Gly), in the spectrum. Table 2.4 lists these brain metabolic compounds with its corresponding chemical shifts and clinical significances, as discussed below.

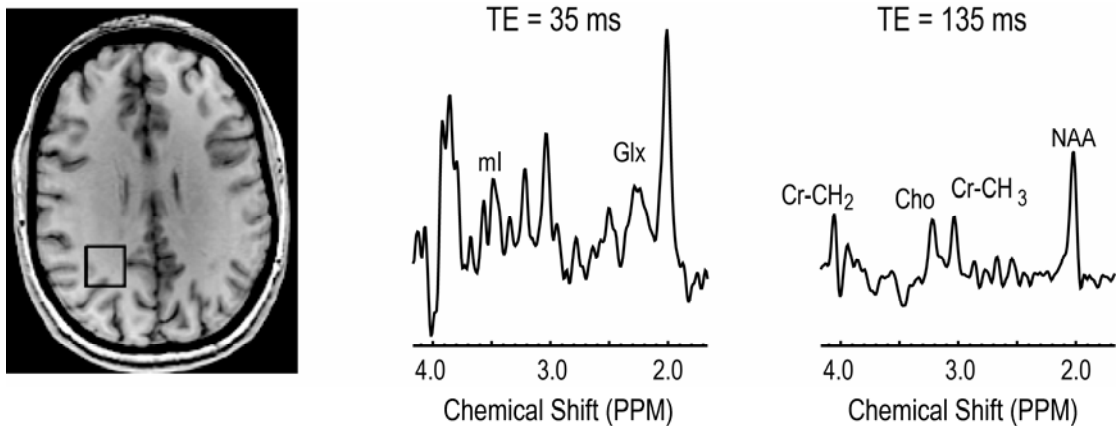
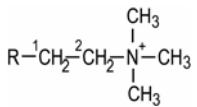
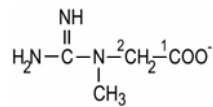
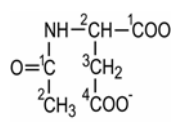
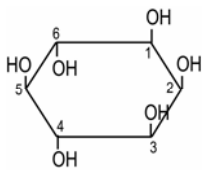
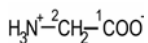
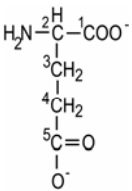
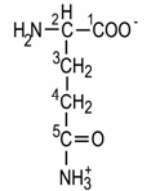
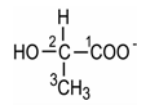
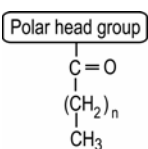


Figure 2.8 Normal brain spectra from a 1-cm^3 voxel acquired with PRESS sequence with TE = 35 ms and TE = 135 ms at a TR of 2 s.

Table 2.4 Major metabolites observed in proton spectra from the brain.

Compound	Chemical Structure	Group	Multiplicity	C S (ppm)	Importance
Cho		N(CH ₃) ₃	singlet	3.2	Cell membrane marker
Cr		² CH ₂ N(CH ₃)	singlet singlet	3.9 3.0	Energy metabolism
NAA		² CH ₃	singlet	2.0	Neuronal marker
mI		¹ CH, ³ CH ⁴ CH, ⁶ CH	doublet of doublet triplet	3.5 3.6	Glial cell marker, Osmolyte
Gly		² CH	singlet	3.5	Neurotransmitter (inhibitory)
Glu		² CH ³ CH ₂ ⁴ CH ₂	doublet of doublet multiplet multiplet	3.7 2.1 2.3	Neurotransmitter (excitatory)
Gln		² CH ³ CH ₂ ⁴ CH ₂	triplet multiplet multiplet	3.7 2.1 2.4	<i>De novo</i> synthesis for Glu
Lac		² CH ³ CH ₃	quartet doublet	4.0 1.3	Anaerobic metabolism
Lip		(CH ₂) _n CH ₃ (CH ₂) _n CH ₃		1.3 0.9	Necrosis or aliasing from subcutaneous lipid

Choline containing compounds

Choline is the precursor of various biologically metabolites as illustrated in Figure 2.9 and its role in phospholipid metabolism (Figure 2.10) has been widely studied by NMR. First, choline is actively transported into the cell and then phosphorylated to phosphatidylcholine (PtdCho), the most important membrane lipid, through Kennedy pathway. PtdCho can be breakdown through several ways to regenerate choline and phosphocholine (PC) as well as producing glycerophosphocholine (GPC), which is subsequently hydrolyzed into glycerol 3-phosphate (G-3-P) and choline.

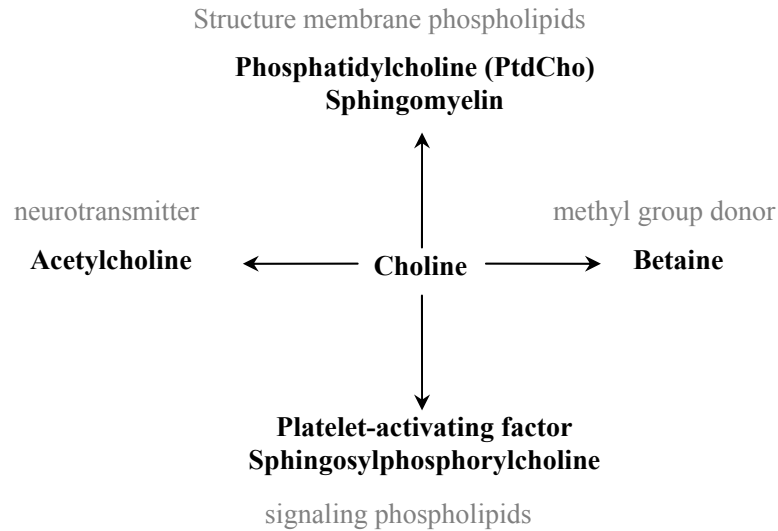


Figure 2.9 Choline metabolism

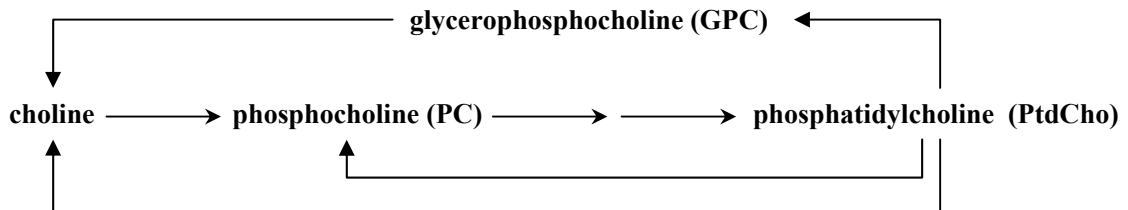


Figure 2.10 Biosynthesis and hydrolysis of phosphatidylcholine.

The Cho peak resonates at 3.22 ppm in proton spectra and represents total choline brain stores, including choline, PC, GPC and acetylcholine. In vivo studies of all human tumors have reported increased total choline levels in tumors compared to normal tissue due to increased cell density and membrane turnover. It has been shown that PC is elevated when a tissue is in its growth phase, while an increase in GPC correlated with the breakdown of cell membranes [31, 32]. Increased PC relative to GPC has been observed in tumor cells [33, 34]. When the patient receives successful treatment, total choline levels are reduced or absent.

Total Creatine

The total creatine, resonating as singlets at both 3.0 and 3.9 ppm, includes Cr and phosphocreatine (PCr), which are impossible to be distinguished from each other in in vivo proton spectra. Cr and PCr are involved in ATP metabolism (Equation 2.12) and thus the level of the total creatine is a marker for cellular bioenergetics. The singlet of the total creatine at 3.0 ppm which has relatively longer T_1 and T_2 is frequently used as a baseline reference level for other metabolites since it is relatively unaffected in most disease. However, studies have shown that the level of the total creatine is not constant but reduced in astrocytomas [8].



N-acetyl aspartate

NAA is found only in brain and spinal cord and possibly functions as an osmolyte. It is synthesized and stored in neurons but hydrolyzed in oligodendrocytes [35]. Since NAA is

a neuronal marker, any pathology with a loss of neurons or function results in reduced NAA levels, such as gliomas. The NAA peak resonating at 2.02 ppm in proton spectra originates from the methyl protons of both NAA and N-acetylaspartylglutamate (NAAG). NAAG is known to act as a neurotransmitter and has protective effects in many of other conditions by stimulating the release of neuroprotective growth factors and inhibiting the release of neurotransmitters, such as Glu [19, 36].

Glutamate and Glutamine

Both Glu and Gln are amino acids. Glu is the main excitatory neurotransmitter in the brain while Gln is an important energy source in mitochondria. Glu is synthesized from Gln or α -ketoglutarate in neurons, and to avoid Glu excitotoxicity, the normal extracellular level of Glu is maintained by the re-absorption of neurons or uptake of astrocytes, where Glu is converted to Gln. Gln can be safely transported back to neurons for reconversion and thus plays a role in detoxification. Instead of taking up Glu, glioma cells have been shown to secrete Glu, resulting in an increase in the level of extracellular Glu. This stimulates tumor cell proliferation and causes excitotoxic damage to normal brain which surrounds the tumor mass and facilitates tumor expansion [37, 38]. Gln is not only a precursor for Glu, but is also a suppressor of apoptosis. Thus it may protect the cells from external stimuli such as radiation therapy as well as contributing to tumor proliferation [39]. The Glx (sum of Glu and Gln peaks) was found to be significantly higher in low oligodendrogliomas than in low-grade astrocytomas [10]. This may be due to the key enzymes of glutamate metabolism and glutamate transporters being present predominantly on oligodendrocytes.

Myo-Inositol and Glycine

mI is predominantly located within astrocytes and is a precursor for the phosphatidylinositol (PI) second messenger system [40] and is also presumed to act as an osmoregulator. The mI peaks often overlap with the peak of glycine (Gly) which is an inhibitory neurotransmitter and resonates as a singlet at 3.56 ppm, even at 3 T. Elevated mIG (sum of mI and Gly) [8] and its ratio to Cr [41] have been observed in low-grade astrocytomas but decreased levels in high grade.

Lactate & Lipid

Lac is the end product of anaerobic glucose metabolism and is expected to indicate hypoxia or poor perfusion within the lesion. Lac is usually not seen in normal brain tissue due to its low concentration but increased Lac has been seen in high grade gliomas. Lac is also an important marker in tumor prognosis and monitoring efficacy of treatments.

The lipids in cell membrane do not significantly contribute to the Lip resonance in proton spectra due to its very short T_2 relaxation. The presence of these Lip resonances in spectra is correlated with mobile lipids, such as adipose or cytoplasmic droplets. The Lip peak may be detected at 1.3 ppm and comes from CH_2 groups in long alkyl chains, because of necrosis or aliasing from subcutaneous lipid. The lipid methylene signal is typically associated with high-grade gliomas [42] and may be useful in grading.

In proton spectra, the methyl group of Lac (1.3 ppm) often overlaps with the methylene groups of Lip. Spectral editing using J-difference methods have been applied to separate Lac from Lip for the quantification of Lac [43, 44]. The methods are sensitive to motion and to phase and frequency variations between the two acquisitions.

Chapter 3: Considerations in applying 3D PRESS H-1 brain MRSI with an eight-channel phased-array coil at 3 T

This chapter evaluates the benefits of using 3 T and multi-channel radiofrequency coils for 3D ¹H MRSI relative to 1.5 T with a quadrature head coil. Issues that are of concern include differences in chemical shift artifacts, line broadening due to increased susceptibility at the higher field strengths and the increased complexity of the post-processing software due to the need for combining signals from the multi-channel data.

3.1 Rationale

The resonant frequencies are different for the protons of the different metabolites. In the readout direction, the difference in chemical shift between water and fat creates a misregistration artifact, seen as a bright or dark band in MR images, which is referred to as chemical shift artifact. Chemical shift artifacts also occur in the slice selection direction resulting in spatial misregistration for metabolite ratios. These errors are dependent on the bandwidth of the selection pulses, the size of the selected region and the resonant frequency, and will become more prominent as the field strength increases. Figure 3.1 (a) shows the spatial variations between Cho and NAA on the edge of the PRESS selected volume. One way to reduce the effect of the chemical shift artifact is to prescribe a PRESS box larger than the region of interest (ROI) (overpress) and to use

very selective suppression (VSS) pulses [27] to suppress signals arising from beyond the ROI (see in Figure 3.1 (b)). Although VSS pulses and overpress have been applied at 1.5 T to reduce chemical shift artifact [27], it was not clear whether the corresponding pulses that had been designed for use at 3 T could cope with the increased magnitude of the effect.

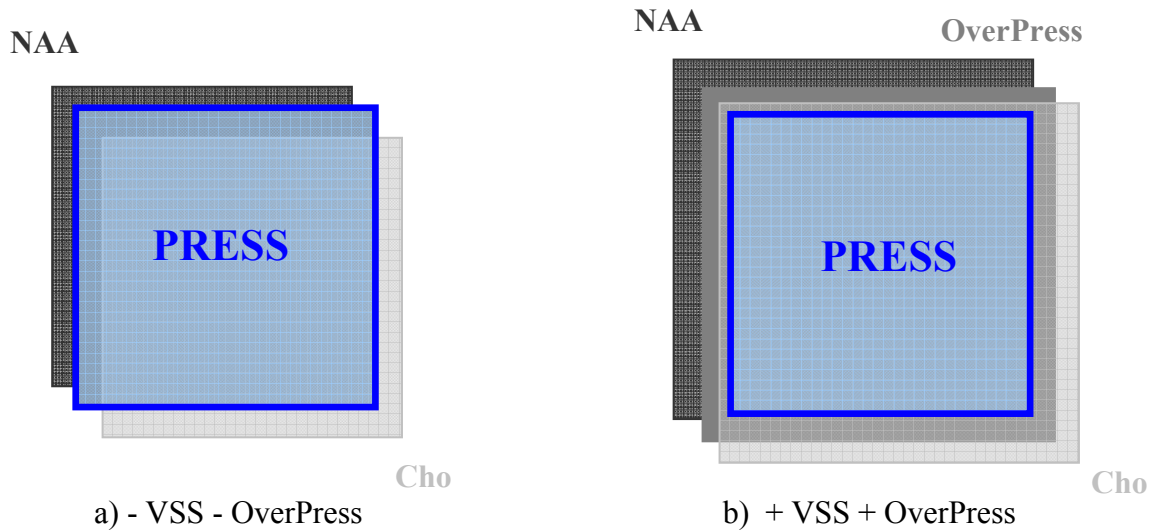


Figure 3.1 The effects of the PRESS selected volumes of resonances corresponding to Cho and NAA with/without VSS and Overpress.

Previous studies using single voxel and spectroscopic imaging of human brain have been applied at 3 T [45-48] and have provided an increase in SNR and spectral resolution relative to studies at 1.5 T [49-51] but with variable magnitude of the response concerning the effect. Concerns have also been expressed as to whether changes in longitudinal and transverse relaxation times of metabolites [52, 53] or increased susceptibility effects in patients with brain tumors would compromise data quality. While the use of phased arrays for MR spectroscopy has been demonstrated previously [54-57],

methods for combining the data from multi-channel radiofrequency coils have not yet been fully explored in a clinical setting.

The current section aims to determine which parameters are important for obtaining reliable spectra from patients with brain tumors at 3 T and to compare the data that are obtained with similar findings at 1.5 T. The issues that were considered includes: the chemical shift artifact for different VSS and overpress factors, the variations in linewidth at 1.5 T versus 3 T, the differences in SNR between the quadrature head coil and the 8-channel phased array coil, and how the details of the data acquisition and post-processing influence the quality of the spectra. These parameters were explored through simulations, as well as acquisitions from phantoms, normal volunteers and patients with brain tumors.

3.2 Methods

Simulated Data

Spectral data were simulated to assess the effects of VSS suppression pulses and overpress factors as described previously [28]. The overpress factor is defined as the ratio of the linear dimension of the excited volume to the prescribed volume. The objects of simulation were a uniform phantom and an elliptical normal brain. The spectra were created using Lorentzian peak shapes with linewidths of 2 Hz, 512 spectral points, and spectral width of 1000 Hz for 1.5 T, and Lorentzian peak shapes with linewidths of 4 Hz, 1024 spectral points, and spectral width of 2000 Hz for 3 T spectra. Water suppression was set as 20:1. Cho, Cr, NAA and Lac relative ratios were 0.5:0.5:1:0.25, respectively. The PRESS volume selection pulses were simulated with bandwidths based upon the

default values used in the product pulse sequences on the 3 T MR scanner. These were 933 Hz for the 180° pulse and 2400 Hz for the 90° pulse. The pulse profiles were simulated to be either ideal (rectangular) or based upon empirical profiles of the selected volume acquired on a uniform phantom. The sizes of the selected volumes were the same for all simulated data. VSS suppression pulses were simulated as having a rectangular profile of either 30 or 40mm in thickness and the efficacy of suppression was assumed to be 90%. The overpress factors considered were 1.0, 1.1, 1.2 and 1.3, with a phase encoding matrix of 16x16x8.

MR Data

Empirical data were obtained from a head phantom, 6 volunteers, and 12 patients using either a standard transmit/receiver quadrature head coil or an 8-channel receive-only phased array coil on 1.5 T and 3 T GE Excite scanners (GE Healthcare Technologies, Waukesha, WI). The MR scans included the acquisition of both anatomic and spectroscopic imaging data.

Anatomical MR images comprised T₁-weighted sagittal scout images (TR/TE = 54/2 at 1.5 T or 70/2 at 3 T), axial FLuid Attenuated Inversion Recovery (FLAIR) (TR/TE/TI = 10002/123/2200 at 1.5 T or 10002/127/2200 ms at 3 T) and T₁-weighted SPOiled GRAdient echo (SPGR) images (TR/TE = 8/2 ms at 1.5 T or 26/3 ms at 3 T).

The 3D H-1 MRSI data were obtained using PRESS volume selection, VSS outer volume suppression and CHESS water suppression with TR/TE = 1100/144 ms. The PRESS volume selection employed pulses with bandwidths of 933 Hz for the 180° pulse and 2400 Hz for the 90° pulse. Overpress factors of either 1.0 or 1.2 and VSS pulses of

width 40mm were prescribed around the prescribed volume. Six additional graphic VSS bands were applied adjacent to the subcutaneous lipid layer to further improve suppression. For the studies performed with the 8-channel coil, proton density weighted GRE images were acquired using the manufacturer-provided parallel imaging calibration sequence to obtain estimates of coil sensitivities (TR/TE = 150/2 ms). The manufacturer's linear autoshim procedure was applied at 1.5 T and their higher-order shimming procedure was performed before spectral acquisition at 3 T. The spectral data were acquired with 512 spectral points, and 1000 Hz spectral width at 1.5 T, and with 1024 spectral points and 2000 Hz spectral width at 3 T. Spectral array sizes were 12x12x8 (acquisition time of about 9 minutes) or 16x16x8 (acquisition time of about 17 minutes) acquired with k-space sampling restricted to an elliptical region of k-space and Fields Of View (FOV) corresponding to a nominal spatial resolution of 1 cc [42]. The excited volumes were positioned in similar regions for each of the data sets that were going to be compared.

Study Population

Phantom spectra were acquired with the standard quadrature head coil and 8-channel phased array head coil at both field strengths, with and without VSS and overpress factors of 1.0 and 1.2. Six healthy volunteers (three males and three females, median age of 27 years) were scanned at 1.5 T and 3 T. To test the reproducibility of such data, the phantom and three of the volunteers were scanned a second time at another 3 T scanner from the same manufacturer with a similar 8-channel coil. A total of twelve patients with different kinds of primary brain tumors were involved in the study. Eight of the patients

were scanned at 1.5 T and 3 T field strengths using the 8-channel coil. All of these spectra were acquired with a 16x16x8 spectral array. The other four patients were initially scanned with the 8-channel coil at 3 T with a 12x12x8 array and with a 16x16x8 spectral array at a follow up scan obtained two months later.

Postprocessing and Analysis

The spectra were quantified using previously published methodology [28]. Spectral arrays from the 8-channel coil were each processed individually and the signals combined using in-house developed software that weights the data by their coil sensitivities. The theory of the combination for eight channel data was based upon a SENSE reconstruction with a reduction factor R of 1.0 as described in a previous paper [58]. The spectral data were apodized by a 2 Hz and 4 Hz Lorentzian filter at 1.5 T and 3 T, as a compromise between reducing noise and distinguishing between overlapping peaks. The peak parameters of the metabolites were computed automatically for each voxel within the excited region using in-house software.

For the empirical data, the 3D H-1 MRSI data were referenced to the 3D SPGR image by assuming that there was no movement between the image and spectra acquisition. The FLAIR image was aligned to the corresponding 3D SPGR image. Segmentation of the brain images was performed automatically on the 3D SPGR images using a program that is based on a Markov random field model [59]. The segmented white matter mask was then used to identify voxels which had at least 90% normal appearing white matter. These were the voxel used for comparative analyses in the volunteer and patient data.

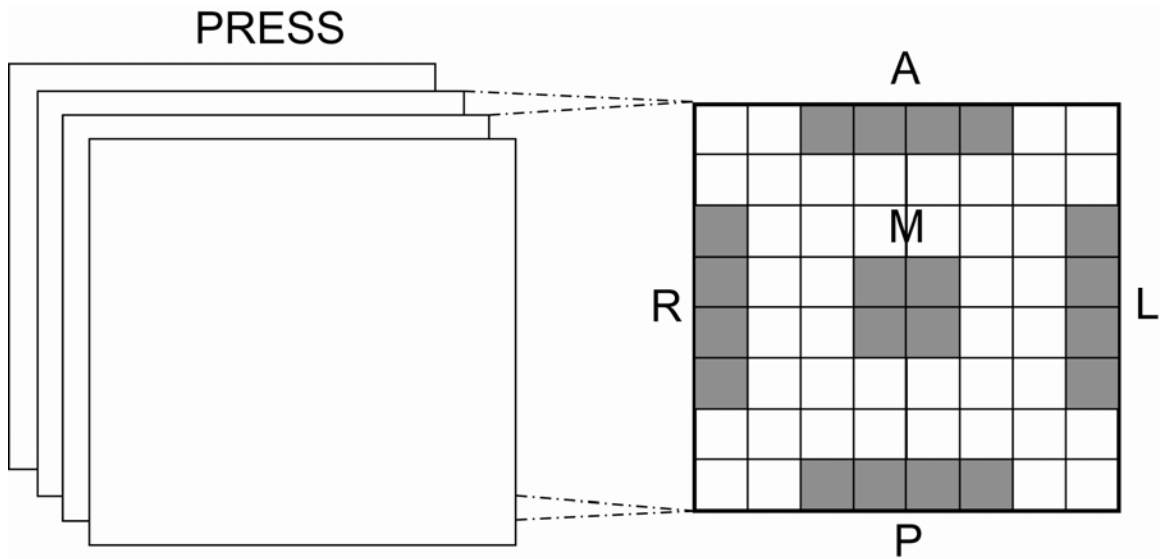


Figure 3.2 H-1 PRESS MRSI applied for studies of chemical shift artifact from a simulation and the phantom. The size of the excited volume was 80mm x 80 mm x 40 mm in all data sets. Chemical shift artifact on the right (R), left (L), anterior (A) and posterior (P) sides were calculated from the average of the central two slices. The middle voxels (M) were used as controls, which have the least chemical shift artifact.

For the study of chemical shift artifact effects in the simulated and phantom data, the mean value of the Cho/NAA ratio were calculated from the center and the right, left, anterior and posterior of the middle two slices (Figure 3.2). The normal voxels for patient data were defined by restricting the analysis to voxels outside of T_2 abnormalities at both 1.5 T and 3 T. To avoid errors in identification of normal voxels, the edges of the PRESS box and ventricles were excluded from the calculation. To eliminate errors due to susceptibility or other artifacts, voxels were only included if the estimated linewidths of all of their peaks were between 2 and 10 Hz. The SNR of individual metabolites were estimated by dividing the heights of the peaks, Cho, Cr and NAA, by the standard deviation of the noise from the peak-free region at the right end of the spectrum [28].

Wilcoxon rank sum tests were applied to evaluate differences in SNR with a P value of 0.05 being considered significant.

3.3 Results

Chemical Shift Artifact in the Simulation

The simulations assumed that the chemical shift artifact was half as much at 1.5 T as at 3 T. The mean Cho/NAA height ratio for the phantom simulation with the ideal profile at 3 T were 0.25 versus 2.50, 0.42 versus 0.91, 0.53 versus 0.53, and 0.53 versus 0.44 on the right and left (R-L) edges with overpress factors of 1.0, 1.1, 1.2 and 1.3, respectively, and 0.32/1.48, 0.40/0.93, 0.45/0.69 and 0.47/0.57 (R-L) for empirical profiles (Figure 3.3). These values were compared with the true ratio of 0.5 in the simulated phantom. For simulated brain spectra at an overpress factor of 1.0, 1.1, 1.2 and 1.3, respectively, the mean Cho/NAA height ratios with ideal profiles were 0.17/1.53, 0.36/0.71, 0.52/0.48 and 0.56/0.45 (R-L), compared with 0.27/1.22, 0.37/0.82, 0.44/0.64 and 0.47/0.56 for empirical profiles. The 40 mm VSS suppression pulses provided better lipid suppression for the simulated brain data than 30 mm VSS at both 1.5 T and 3 T. The chemical shift artifact decreased with the overpress factor and it was observed that an overpress factor of 1.3 was needed to entirely eliminate the chemical shift artifact for the empirical profiles at 3 T. Because of the concern that we would be exciting subcutaneous lipids for the in vivo situation, we selected overpress factors of 1.2 and VSS pulses of 40 mm for the phantom and in vivo human studies.

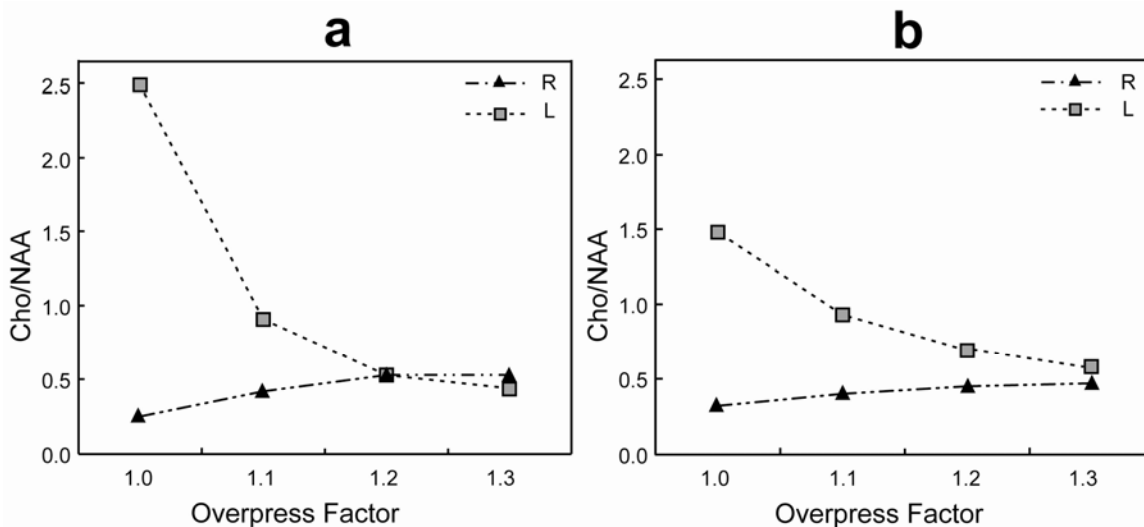


Figure 3.3 Simulation of H-1 PRESS MRSI with different overpress factors. The changes in mean Cho/NAA height value in the R-L direction of the spectra with (a) ideal profiles and (b) empirical profiles are shown. Chemical shift artifact decreases with increases in the overpress factor. An overpress factor of 1.2 is needed to eliminate the chemical shift artifact with ideal profiles at 3 T, and a factor of 1.3 is needed with empirical profiles.

Chemical Shift Artifact in the Phantom

Phantom data with an overpress factor of 1.0 clearly showed the chemical shift artifact on the edges of the PRESS box. The 3D MRSI with and without VSS and with overpress factors of 1.0 and 1.2, acquired with an 8-channel coil at 3 T, are shown in Figure 3.4. The spectra from the top right corner have low Cho/NAA and Cr/NAA ratios, while the opposite corner have higher levels (Figure 3.4 (d)). Application of VSS and an overpress factor of 1.2 significantly reduces the chemical shift artifact as seen by the differences in relative levels of Cho and NAA on the far right column of spectra in Figure 3.4 (e) versus Figure 3.4 (d), as well as offering a much sharper edges on the image (Figure 3.4 (c)).

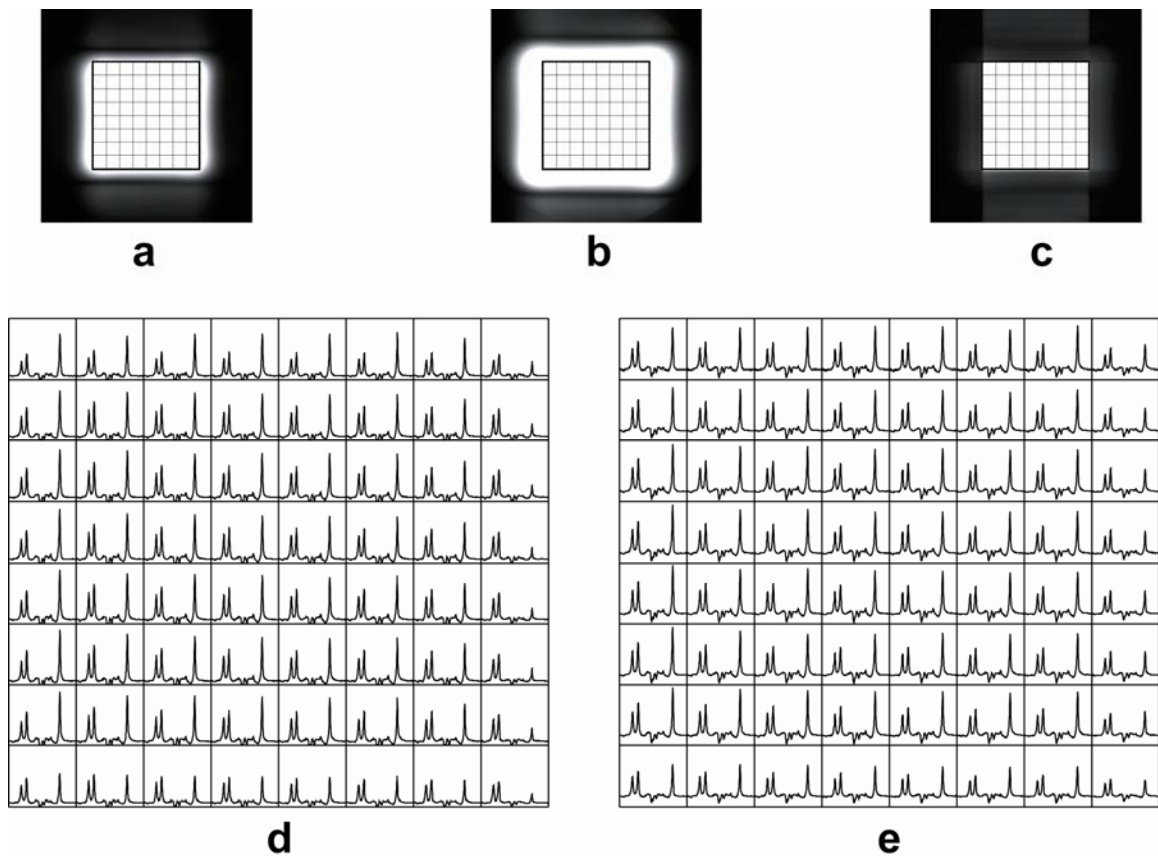


Figure 3.4 The top images were scanned (a) without VSS and with an overpress factor of 1.0, (b) with an overpress factor of 1.2 only, and (c) with 40 mm VSS and an overpress factor of 1.2. The bottom spectra (d) and (e) correspond to the top images (a) and (c), respectively.

The chemical shift artifact with an 8-channel coil at 1.5 T and 3 T are illustrated in Figure 3.5. At 1.5 T, the mean Cho/NAA height ratio was 0.33 versus 0.63 on the right and left (R-L) edges, and 0.38 versus 0.49 on the anterior and posterior (A-P) edges of the PRESS box without VSS pulses and with an overpress factor of 1.0, but were 0.40/0.52 (R-L) and 0.44/0.45 (A-P) when the VSS pulses and an overpress factor of 1.2 were used. The ratio expected from knowledge of the metabolite concentrations in the phantom was 0.5. Corresponding values at 3 T were 0.35/1.61 (R-L), and 0.35/0.65 (A-P)

without VSS pulses and with an overpress factor of 1.0 compared with 0.46/0.75 (R-L) and 0.45/0.55 (A-P) with VSS pulses and an overpress factor of 1.2. These results are consistent with the simulated data in that the chemical shift artifact at 3 T is much larger, and that the lower bandwidth in the R-L direction (180° pulse) caused larger errors. Applying VSS pulses with an overpress factor of 1.2 significantly reduced the artifact. Similar results were obtained from the quadrature head coil.

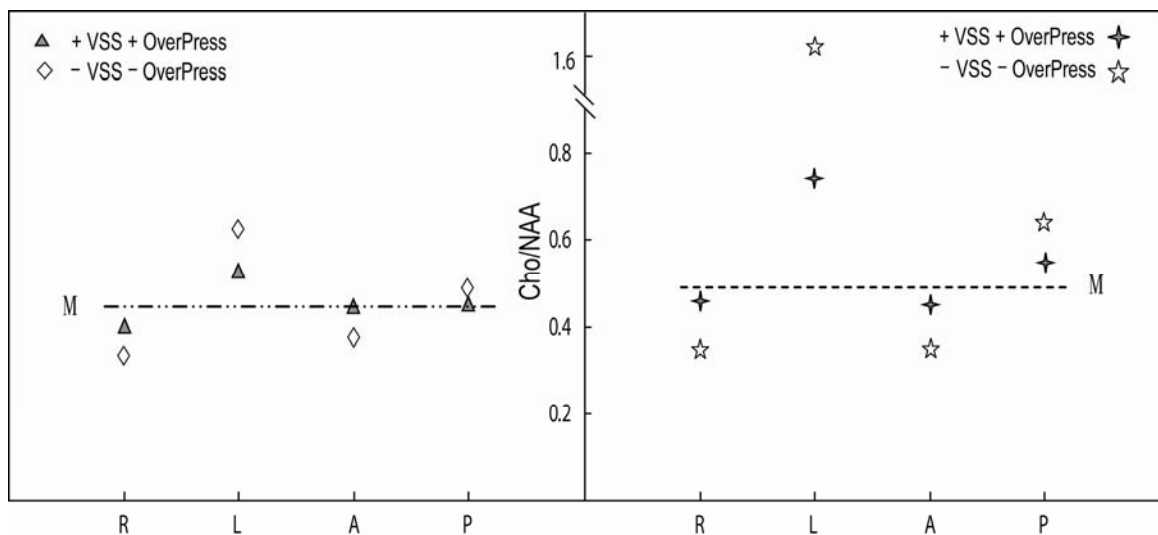


Figure 3.5 Chemical shift artifact observed with an 8-channel coil at 1.5 T (left) and 3 T (right), with/without 40 mm VSS and an overpress factor of 1.2 measured in a uniform phantom. The labels, R, L, A and P represent right, left, anterior and posterior voxels of the PRESS box, respectively, and M represents central voxels, as shown in Figure 3.2. VSS and overpress significantly reduce chemical shift artifact in the phantom data.

Coil and Field Strength Comparison

The SNR of spectra obtained from the phantom (with VSS pulses and an overpress factor of 1.2) and volunteers with the 8-channel coil and the quadrature head coil at 1.5 T and 3

T are given in Table 3.1. The SNR at 3 T with the 8-channel coil was on average 1.96 times higher in the phantom but only around 1.53 times higher for volunteers at 3 T relative to 1.5 T. The SNR in the 8-channel coil was on average 52% higher than in the quadrature head coil at 1.5 T, and 71% higher relative to the quadrature head coil at 3 T. For the volunteer data, the SNR at 3 T with the 8-channel coil was around 2.33 times the SNR for data acquired at 1.5 T with the quadrature head coil. The spectra of the phantom and three volunteers that were obtained on the two different 3 T scanners with 8-channel coils demonstrated similar SNR values and linewidths.

Table 3.1 SNR of metabolites with an 8-channel coil and a quadrature head coil at 1.5 T and 3 T.

	8-Channel Coil			Quadrature Coil		
	Cho	Cr	NAA	Cho	Cr	NAA
Phantom						
1.5 T	105	153	234	78	108	162
3 T	220	297	428	136	183	254
3 T/1.5 T	2.09	1.94	1.83	1.75	1.70	1.57
Volunteers (n=6)						
1.5 T	31	26	59	21	17	38
3 T	47	41	89	27	24	53
3 T/1.5 T	1.52	1.58	1.51	1.29	1.41	1.39

Field Strength Comparison for Patients

An example of MRSI from a patient with Grade IV glioma at 1.5 T and 3 T is shown in Figure 3.6. Note that the spectra are scaled by the estimated standard deviation of the noise in each dataset. The 3 T spectra demonstrated higher SNR and better quality as compared with 1.5 T data in both normal and tumor voxels. The differences in SNR at 3

T and 1.5 T with the 8-channel coil for the eight patients studied with the 8-channel coil with a 16x16x8 phase encode array were 1.44 for Cho, 1.50 for Cr and 1.55 for NAA as shown in Figure 3.7. These values are consistent with those observed in normal volunteers. If taken together, the SNRs of Cho, Cr and NAA from segmented normal appearing white matter (NAWM) for the total six volunteers and eight patients were 31 ± 10 , 24 ± 7 and 56 ± 17 at 1.5 T, and 50 ± 13 , 41 ± 10 and 91 ± 24 at 3 T, which are consistent with the results shown in Table 3.1 and Figure 3.7. When corrected for filtering, the estimated linewidths for Cho, Cr, and NAA at 1.5 T were 4.5 ± 1.2 Hz, 4.3 ± 1.0 Hz and 5.2 ± 1.4 Hz at 1.5 T, and at 3 T were 6.5 ± 1.4 Hz, 6.1 ± 1.2 Hz and 6.9 ± 1.3 Hz (mean \pm standard deviation). This means that, when expressed in terms of parts per million, the spectral resolution was better at 3 T relative to 1.5 T.

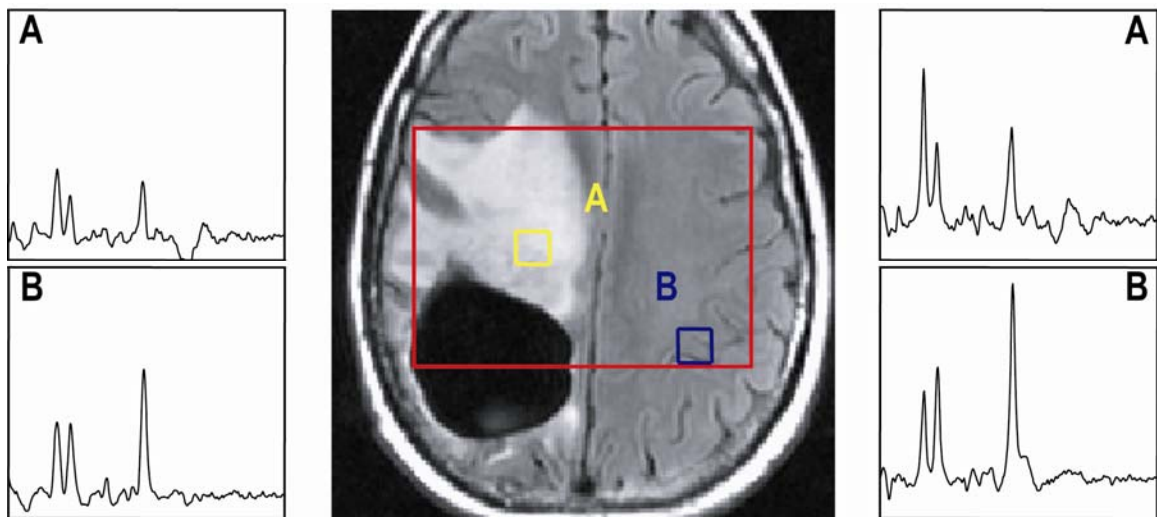


Figure 3.6 MRSI for a patient with a Grade IV glioma at the same noise scale for acquisitions at 1.5 T (left) and 3 T (right). Voxel A comes from the tumor region, which has higher Cho and lower NAA, and voxel B is from the normal region. The vertical scales of all four spectra were adjusted to equalize the noise level of the different spectra. The spectra at 3 T have higher SNR in both tumor and normal voxels.

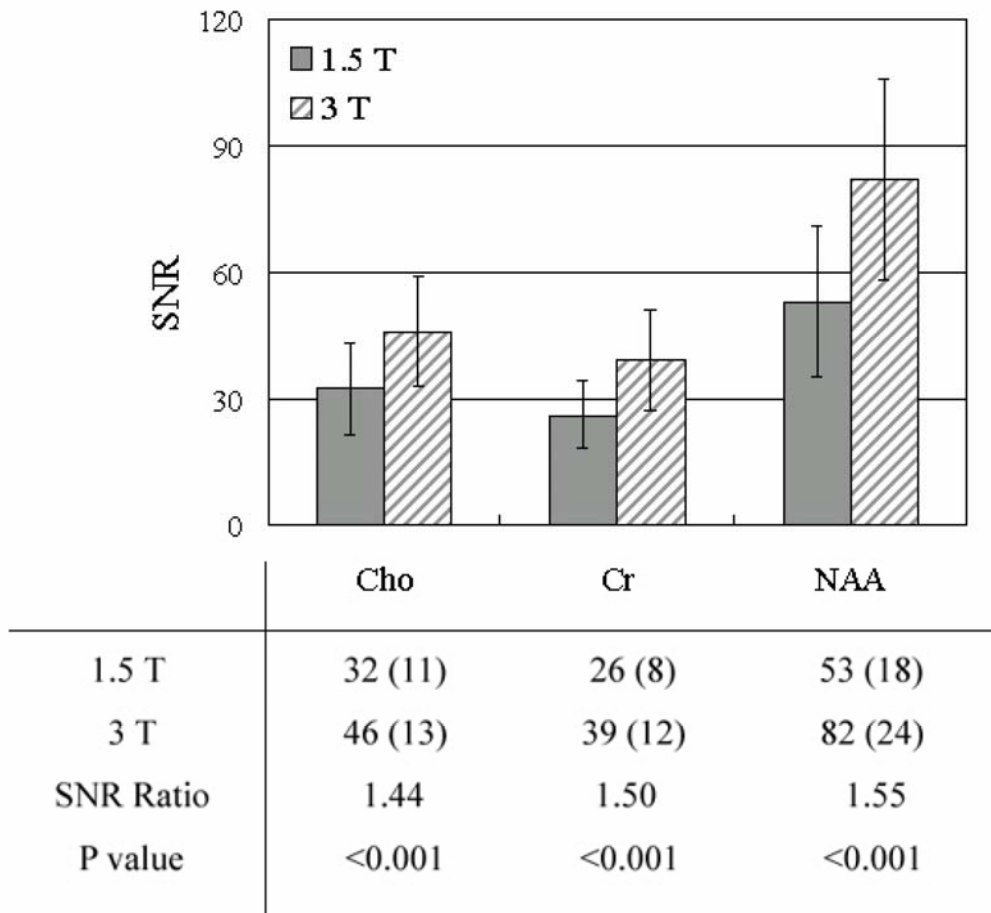


Figure 3.7 SNR of metabolites with an 8-channel coil at 1.5 T and 3 T from the normal voxels of eight primary brain tumor patients. Around 300 voxels were involved in the calculation at 1.5 T and 3 T. The SNRs of Cho, Cr and NAA at 1.5 T and 3 T are shown in the table (mean \pm standard deviation). P-values of less than 0.001 were obtained for all three metabolites for the difference of SNR at 1.5 T and 3 T by Wilcoxon rank sum tests.

Comparison of 12x12x8 and 16x16x8 Phase Encoding Arrays

The spectra acquired with different phase encoding arrays are shown in Figure 3.8. Compared with spectra acquired with the 16x16x8 array, the spectra with 12x12x8 had a lower SNR and more lipid contamination. The latter is a universal dilemma in MRSI data

with small FOV. Since the SNR is proportional to the square root of scan time, the theoretical value of the difference in SNR for spectra 16x16x8 and 12x12x8 is around 1.33. From the patients data (156 voxels), the SNRs of the Cho, Cr and NAA in the 3 T spectra that were acquired with 16x16x8 phase encoding steps was 1.19, 1.29 and 1.27 times higher than for the corresponding 12x12x8 data. The ratio from the patients was thus close to the theoretical value.

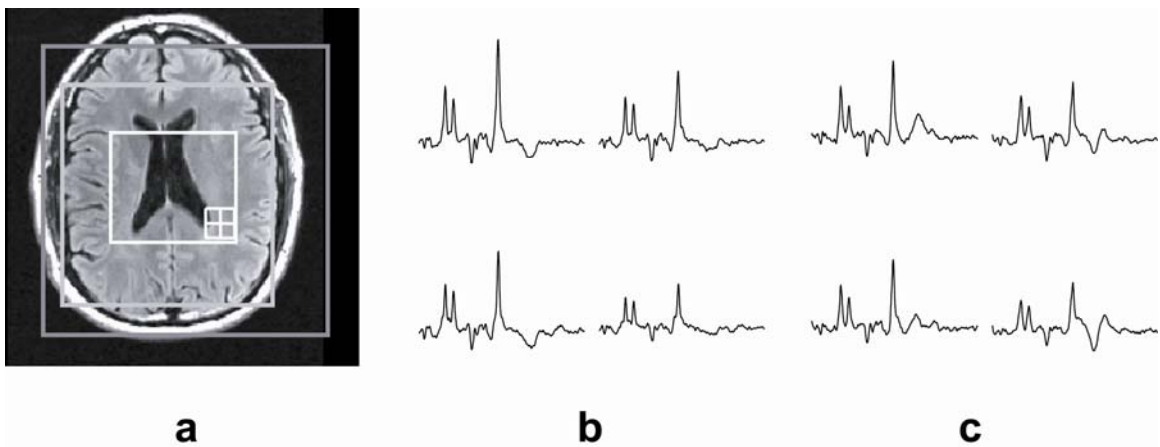


Figure 3.8 (a) MRSI data from a glioma patient with (b) 16x16x8 and (c) 12x12x8 phase encoding array. (b) The spectra with the 16x16x8 phase encoding array were positioned the same as (c) those with the 12x12x8 phase encoding array. The vertical scales of all the spectra were adjusted to equalize the noise level of the different spectra. The spectra with 16x16x8 exhibited higher SNR, while the spectra with 12x12x8 have more lipid contamination.

3.4 Discussion

Although PRESS H-1 MRSI is a powerful tool for providing metabolite profiles for patients with brain tumors, the spatial resolution obtained on 1.5 T scanners with a standard quadrature head coil is relatively coarse (1-2 cc) and the acquisition time is

typically long (10-20 minutes). The availability of higher field strength MR scanners and multi-channel radiofrequency coils offer the potential for obtaining MRSI data with higher SNR and better spectral resolution for such patients but also introduce complications in terms of the magnitude of the chemical shift artifact, increased susceptibility, differences in relaxation times and the need for more complex reconstruction algorithms. The objective of our study was to determine how these factors affect the application of MRSI to patients with brain tumors and to establish a protocol that would provide robust and good quality data.

The first issue that we considered was the effect of chemical shift artifact. Spectra simulated with ideal and empirical profiles showed the anticipated two-fold increase in effect with the field strength but this artifact decreased rapidly with increasing overpress factors. Note that the magnitude of the effect depended on whether ideal or empirical profiles were used in the simulation. This was due to the larger transition bands of the empirical pulses resulting in imperfect edge excitation. Simulations representing a uniform phantom and normal brain with empirical profiles demonstrated that 40 mm VSS suppression pulses and an overpress factor of 1.3 would be needed to eliminate the chemical shift artifact completely for selected volumes that were representative of those used in patient studies. Because it was felt that the magnitude of residual subcutaneous lipids would be unacceptable with an overpress factor of 1.3, the value used for empirical studies was 1.2.

The empirical data confirmed that the use of VSS pulses and increased overpress factors significantly reduced the chemical shift artifact in both the 8-channel and the quadrature head coils. However, as predicted by the simulations, the spectra at 3 T were

still not completely uniform. These residual effects could be corrected by applying numerical factors determined from the simulations to the edge voxels to obtain accurate Cho/NAA ratios, or by using selection pulses with higher bandwidths (such as spatial/spectral pulses) [25]. In this context it should be noted that the default overpress factor in the product pulse sequences on most manufacturer's scanners is 1.0. If the radiologist is not familiar of this effect there is a danger of over-calling tumors on one side of the selected volume and under-calling them on the other. Clearly it would be much safer to either apply appropriate overpress factors or to use other means to correct for the chemical shift artifact. While the artifact is present at both field strengths it is further accentuated at 3 T.

Another potential concern at the higher field strength has been the anticipated increase in linewidths due to larger susceptibility artifacts. In a previous paper, the authors claimed that improvements in SNR at 3 T were almost offset by the peak broadening [49]. In the current study, the estimated linewidths for Cho, Cr, and NAA at 1.5 T were 0.071 ± 0.019 ppm, 0.067 ± 0.016 ppm and 0.082 ± 0.022 ppm at 1.5 T, and at 3 T were 0.051 ± 0.011 ppm, 0.048 ± 0.009 ppm and 0.054 ± 0.010 ppm. Hence the peak separation at 3 T was still better than at 1.5 T for both normal volunteers and patients. This implies that the higher-order shimming provided by the manufacturer worked well for the PRESS selected volume, despite the presence of surgical cavities and other treatment effects.

The increased SNR at 3 T that we observed was 1.67 for phantoms and 1.36 for normal volunteers at 3 T versus 1.5 T with the quadrature head coil. Corresponding values for the 8-channel coils were 1.95 for phantoms, 1.54 for normal volunteers and

1.50 for patients. We believe that the differences in magnitude of the field strength effect between coils reflect that the 3 T quadrature coil was not optimized for data acquisition at this field strength and that the values from the 8-channel coil are more representative of the true benefits that can be obtained. Previous studies comparing 1.5 T and 3 T with single voxel and multi-voxel proton MRS obtained similar increases in SNR [49-51]. The differences in magnitude of the effect between the phantom and human studies are due to known differences in the in vivo relaxation times at the two field strengths. The T_1 values of metabolites at 3 T are longer and T_2 values are shorter than the data found at 1.5 T [52, 53], which would result in a reduction in signal when using the same TR/TE. The change of differences in SNRs due to relaxation was computed by using T_1 and T_2 values of occipital gray matter reported in papers [52, 53], respectively. The 3 T to 1.5 T signal ratio of NAA would have increased 10% in applying the T_1 correction and a further 24% in applying the T_2 correction.

Of particular interest is that the SNR obtained at 3 T with the 8-channel coil was, on average, 2.33 times higher in normal volunteers than for the current standard which is using the quadrature head coil at 1.5 T. This means that there is considerable scope for improving the spatial resolution or shortening the acquisition time for patients with brain tumors using the new hardware. Other possibilities are to use the improved spectral resolution to obtain more reliable quantification and improved detection of metabolites other than Cho, Cr and NAA [50, 51]. The improved SNR for the phased array coils [60] is because each coil element only detects tissue noise from a limited tissue volume and that the signals can be combined to provide an extended spatial coverage. In our study, we reconstructed spectra from the 8-channel coil using the empirical profiles derived

from a calibration sequence that the manufacturer provides for parallel imaging. This proved to be robust but required independent phase and frequency correction for each channel before the signals were combined.

As a first step in examining the potential for shorter acquisition times with the 3 T and 8-channel coil we compared spectra acquired from patients with two different matrix sizes that had scan times of 9 and 17 minutes. Spectra acquired with the more limited phase encode array and shorter acquisition time were found to have lower SNR that was consistent with theoretical expectations. However, due to the smaller FOV, subcutaneous lipids were more likely to be folded in with the smaller matrix using the same nominal spatial resolution. In order to benefit from the shorter data acquisition time, more robust methods need to be developed to correct for lipid. One possibility is the use of parallel imaging reconstruction methods for lipid unfolding based on sensitivity encoding (SENSE) [61]. When combined with the use of 3 T MR scanners and multi-channel radiofrequency coils, these methods will provide robust MRSI data from patients with brain tumors in a much shorter scan time.

In conclusion, we have demonstrated an increase in SNR at 3 T as well as with the 8-channel phased array head coil in 3D H-1 MRSI data. The improved SNR obtained at 3 T with the 8-channel coil could be utilized to provide finer spatial resolution with the same acquisition time or to reduce the acquisition time to the more clinically relevant range of 5-9 minutes. The development of multiple-channel coils enhances the quality of spectra. The future application of larger coil arrays and even higher field strength, such as 7 T, may further improve the SNR of such spectra, which will be discussed in subsequent chapters.

Chapter 4: Comparison of T_1 and T_2 metabolite relaxation times and metabolite concentrations in glioma and normal brain at 3 T

This chapter studies T_1 and T_2 relaxation times of metabolites in the lesions of T_2 hyperintensities in glioma patients at 3 T and investigates the differences in metabolite levels after corrections for relaxation times.

4.1 Rationale

Previous chapter has shown that the availability of higher field strength MR scanners (3 T) and multi-channel radiofrequency coils offers the potential of higher SNR and better spectral resolution [12] and thus provide more reliable quantification and improved detection of other important brain metabolites, such as, Glu, Gln and mI, which can be detected in spectra with short echo times. However, peak overlap and complex coupling patterns still make it difficult to isolate individual components. As we know, the spin echo sequence can rephase inhomogeneities and chemical shift, but the frequency difference will be maintained for the coupled spins as a function of TE and $1/J$ and complicates quantification (Figure 4.1 (a)). This is because the 180° pulse also inverts the J-coupled partner, X spin, which causes the splitting of the A spin. When only one spin experience this pulse, the coupling will refocus as shown in Figure 4.1 (b). It has been implemented as Lactate-editing with BASING PRESS [43] to separate Lac from Lip.

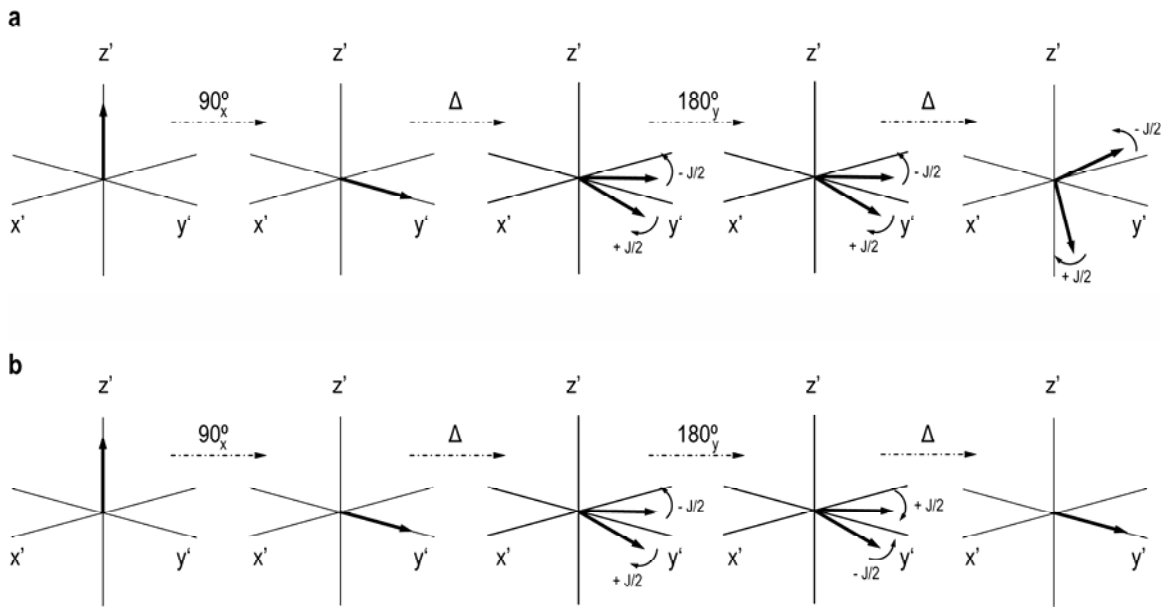


Figure 4.1 The influence of spin-echoes on spin-spin coupling as illustrated for the coupled spins A and X when both spins experience a 180° pulse (a) and when only spin A experiences a 180° pulse (b).

Two-dimensional J-resolved spectroscopy, a technique that has been performed on high-resolution NMR spectrometers for decades, more recently has been applied for in vivo MRS studies on clinical MR scanners [62, 63]. This technique enables the separation of J-coupling information from chemical shift by encoding J-coupling in the t_1 dimension of a 2D spectrum using different echo times. The addition of the second frequency dimension also allows the separation of Lac from Lip [62]. For in vivo studies, the number of echo times used for J-resolved MRS is typically 32 or 64 with F_1 spectral resolution of ~ 3 Hz based upon the coupling constant of Lac (~ 7 Hz) [64]. An example of 2D J-resolved spectra for a molecule with three spin $\frac{1}{2}$ nuclei is illustrated in Figure 4.2. However, 2D J-resolved spectroscopy is not very useful because it does not resolve the problem of overlapping.

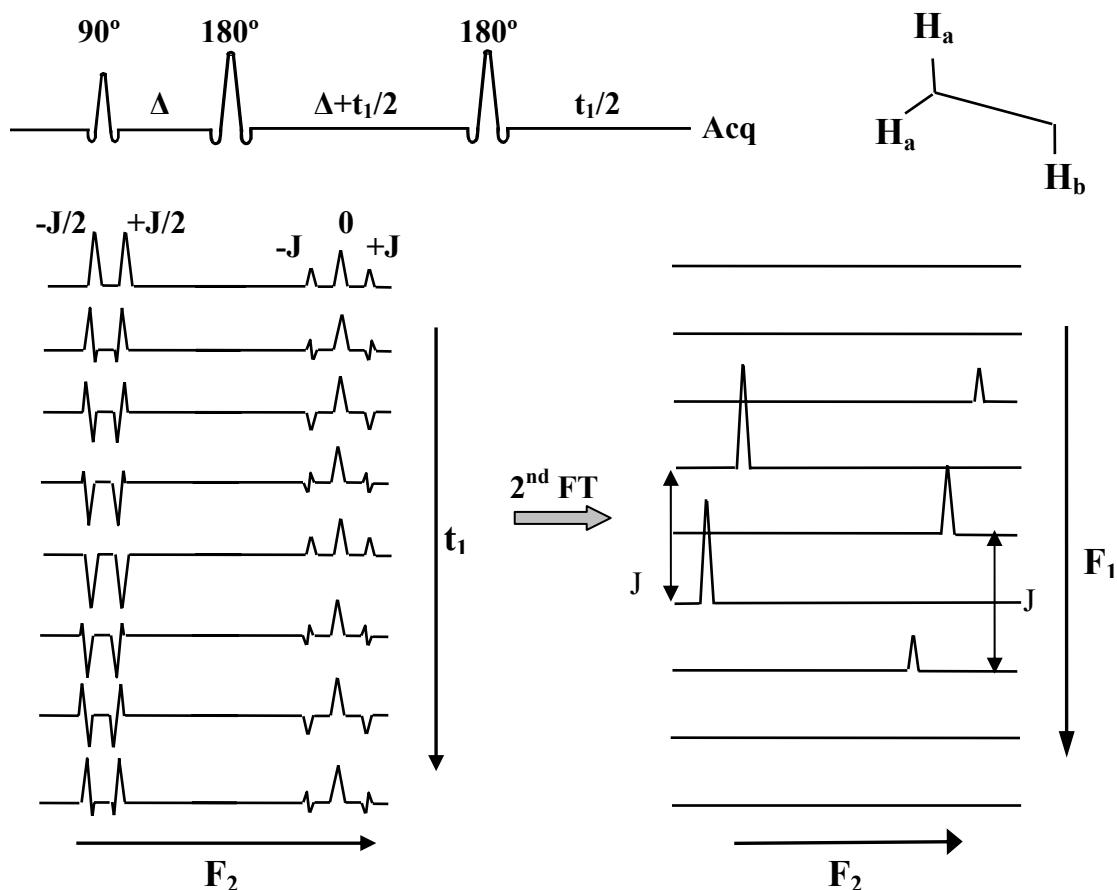


Figure 4.2 2D J-resolved spectra for a molecule with two types of protons.

Recent studies have used this sequence in conjunction with an averaging across the different echo times to offer unobstructed detection of Glu [65]. This technique offers a more reliable quantification of coupled resonances by effectively canceling the side bands of multiplets. It separates C4 protons of Glu from NAA and Gln at 2.35 ppm, and also yields a singlet of C2 protons of Glu and Gln at 3.75 ppm (Figure 4.3). Since data are acquired at multiple echo times, it also enables measurement of T_2 relaxation times for singlets, but not for metabolites with strong coupling resonances, which do not follow the single exponential decay behavior. In addition, whether the effective separation of Glu and Gln in the TE-averaged spectra depends on T_2 values has not been clarified.

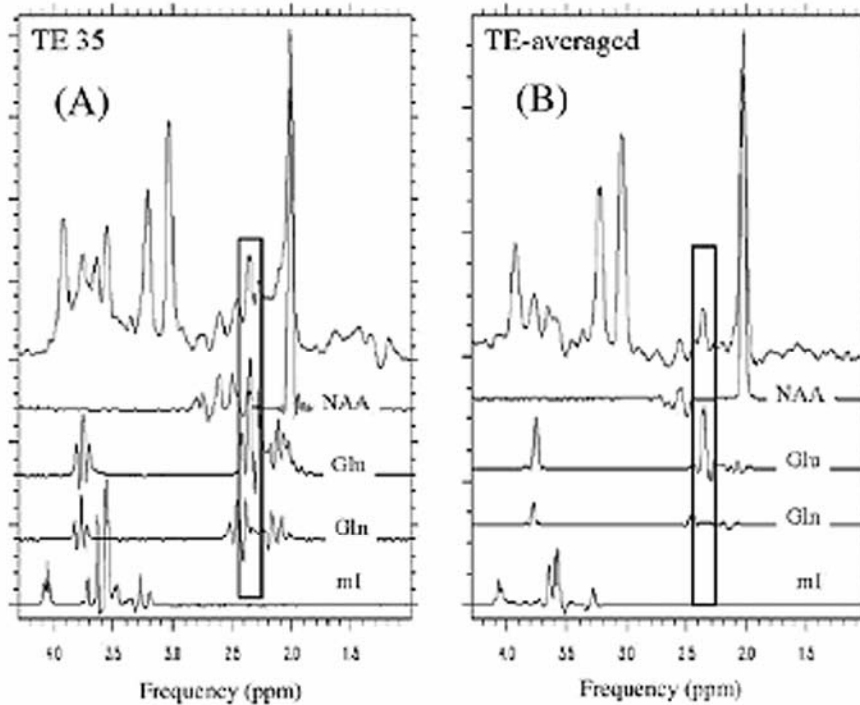


Figure 4.3 Comparison of Glu detection with conventional PRESS and TE-averaged PRESS at 3 T [66]

In planning the data acquisition parameters for using MRSI to determine the spatial extent of tumor versus normal brain tissue, it is important to consider how to select values that will emphasize the contrast between metabolites in the different regions. Because of the restrictions on clinical scan time, the repetition time (TR) for acquiring MRSI data is often set at 1~2 s and is usually only possible to acquire data with a single echo time (TE). In deciding which TE is most appropriate for a particular data acquisition it is important to consider the differences in metabolite intensities caused by the effects of T_1 and T_2 relaxation times, as well as the changes in metabolite concentrations associated with pathology. Previous studies have reported a difference in T_2 relaxation time between tumor and normal tissues in brain at 1.5 T [9, 67], but the values reported were variable and there is no literature about the T_2 relaxation times in brain tumors at 3 T.

This section aims to use single voxel 2D J-resolved PRESS with an 8-channel phased array coil at 3 T, a) to measure the longitudinal and transverse relaxation times of Cho, Cr and NAA within anatomic lesions corresponding to Grade III and Grade IV gliomas and to compare them with white matter (WM) or normal-appearing white matter (NAWM), b) to compare estimates of metabolite levels in tumor versus NAWM, and c) to evaluate the differentials in Cho, Cr and NAA with and without corrections for relaxation times.

4.2 Methods

Study population

Ten volunteers (four males and six females, median age of 28 year) and twenty-three patients (eleven males and twelve females, median age of 44 year) with gliomas at different clinical stages were studied. Tumors were graded by histological examination of tissue samples obtained during biopsy or surgical resection. Of all the patients, there were two Grade II oligodendrogliomas, five Grade III (two oligodendrogliomas, and three anaplastic astrocytomas), fifteen Grade IV (GBM) patients and one oligodendroglioma with unknown grade.

MR Data

All of the empirical data were acquired using an 8-channel phased array coil on a 3 T GE Signa scanner running the Excite software package (GE Healthcare Technologies,

Waukesha, WI). The MR exams included the acquisition of both anatomic and spectral data.

Anatomical MR images comprised T_1 -weighted sagittal scout images (TR/TE = 70/2 ms), axial FLuid Attenuated Inversion Recovery (FLAIR) (TR/TE/TI = 10002/121/2200 ms) and T_1 -weighted SPOiled GRAdient echo (SPGR) images (TR/TE = 26/3 ms).

2D J-resolved PRESS data were obtained using 64 steps with an increment time of 2.5 ms starting at TE of 35 ms [65]. With a TR of 2 s and a number of excitation (NEX) of 2, the total acquisition time was ~5 minutes. For T_1 studies, TE-averaged PRESS data was obtained with 16 steps and an increment time of 10 ms at TR = 1s with NEX = 4, TR = 2 s with NEX = 4, and TR = 8 s with NEX = 2, respectively [65, 66]. The spectral data were acquired with 2048 spectral points, and 5000 Hz spectral width. To obtain estimates of coil sensitivities for the combination of the 8-channel data, unsuppressed water spectra were acquired at an echo time of 35 ms with each of the PRESS spectra.

The 8-cc single voxels were located within WM, NAWM or regions of tumor for participants as illustrated in Table 4.1. The volume of interest (VOI) from volunteers was localized in the parietal white matter. The NAWM in patients was positioned as far as possible from the lesions and included four parietal NAWM voxels and six frontal NAWM voxels. The tumor regions were defined by T_2 hyperintensity from T_2 FLAIR images and positioned to cover as much of the lesion as possible. The number and regions of interest (ROI) investigated for each patient in the T_2 studies were shown as follows: four patients (NAWM only), six patients (NAWM and one tumor voxel) and nine patients (one tumor voxel only). Due to long acquisition times to measure T_1 values

of metabolite, relatively a small number of patients was involved in the study and these patients varied from low grade gliomas to high grade gliomas.

Table 4.1 Patient population involved in the study.

		T₂ study		T₁ study
		WM or NAWM	T ₂ hypertense lesion	T ₂ hypertense lesion
Volunteers (N=10)		N=10		N=8
Grade II (N=2)				N=2
Gliomas (N=23)	Grade III (N=5)	N=3	N=5	N=1
	Grade IV (N=15)	N=7	N=10	N=4
	unknown grade (N=1)			N=1

N=number of patient.

Postprocessing and Analysis

Post-processing was applied on a Sun workstation using the SAGE software packageTM (General Electric, Milwaukee) which is based on the IDL (Research Systems, Inc., Boulder, CO) software package. An internal water reference was used for phase and frequency correction, and apodization was applied in the F₂ dimension. 8-channel data were combined in the time-domain using the unsuppressed water signal [56]. Spectra were then zero filled and processed with a fast Fourier Transform (FFT).

Metabolite T₁ and T₂ estimation

To increase the SNR and the accuracy of the T₂ calculation, data for each echo-time were averaged with the one before and the one after in the t₁ dimension and then Fourier transformed in the t₂ dimension. The peak heights of Cho at 3.22 ppm, Cr-CH₃ at 3.02

ppm and NAA at 2.02 ppm were extracted from the spectra with TE from 57.5 ms to 190 ms, a total of 54 spectra, to reduce the contamination of macromolecules and/or J-coupled multiplets, and fitted to a single exponential function. Only the T_2 fits with variances of the fit residue smaller than 10% were included in the analysis.

T_1 metabolic relaxation times were calculated from partial T_1 saturation using a two-parameter least-squares fitting routine using the equation

$$S / S_0 = 1 - 2 \exp[-(TR - TE / 2) / T_1] + \exp(-TR / T_1) \quad (4.1)$$

where S is the signal intensity acquired at three different TRs, S_0 is the fully relaxed signal intensity, and the effective TE of the TE-averaged spectra for T_1 acquisition is 110 ms. The signal intensities of Cho, Cr and NAA were normalized for the NEX before T_1 fitting.

Estimation of Differences in Metabolite Levels

To estimate metabolite levels, the combined data were averaged in the t_1 domain before zero filling and then quantified using the LCModel package [29] and QUEST (quantitation based on quantum estimation) quantitation algorithm [30] in the Magnetic Resonance User Interface (MRUI) spectrum analysis program.

An in vitro basis set of individual metabolites, consisting of NAA, Glu, Gln, Cr, Cho and mI, was prepared for LCModel. The fitting was performed between 3.85 ppm and 1.8 ppm to minimize spectral artifact from lipid. Metabolite concentrations included in analysis were those with relative Cramér-Rao lower bounds (CRLB) lower than 5% for Cho, Cr and NAA, and 20% for mI and Glu.

For QUEST, the signals were analyzed in the time domain. To minimize the incorporation of large broad baseline components, the first data point of the free induction decay (FID) was excluded and the first twenty points were weighted by a quarter-wave sinusoid [68]. A Hankel Lanczos singular value decomposition (HLSVD) filter was applied to remove the residual water from the spectra [69]. Metabolic signals for the basis set were generated using GAMMA simulations [70] with prior knowledge of chemical shift and J-coupling [64]. Due to known differences in T_2 relaxation times between two singlets of Cr peak, Cr-CH₂ and Cr-CH₃ are separated into two spectra in the basis set. The selection criteria for QUEST estimates were defined by the output parameters from the QUEST analysis, namely a CRLB smaller than 20% and additional common damping factor smaller than 12 Hz. The calibration factors for both methods were obtained from a standard GE MRS HD phantom (12.5 mM NAA, 10 mM Cr, 3 mM Cho, 12.5 mM Glu, 7.5 mM ml and 5 mM lactate) and 50 mM NAA only phantom (50 mM phosphate buffer, pH 7.2) and were applied in all of the data sets.

To estimate the T_2 values on the effective separation of Glu and Gln in the TE-averaged spectra, the spectra were created with 2048 spectral points and spectral width of 5000 Hz and TE values starting at 35 ms in 128 steps of 2.5 ms and 64 steps of 2.5 ms. To approximate the effects of transverse relaxation time and inhomogeneities for the in vivo spectra for Glu and Gln, the time data were multiplied by a factor, $e^{-t_1/T_2} e^{-t_2/T_2^*}$, where t_1 is the echo time (TE) and t_2 is the total sampling time. T_2^* was set to 50 ms which was estimated from the mean linewidth of metabolites [12], and a simple monoexponential decay was applied to the data with T_2 values of 100 ms, 200 ms and 300 ms, respectively. A 4-Hz Lorentzian apodization, zero filling and Fourier Transform were applied and the

spectra were averaged in the t_1 domain. Figure 4.4 shows the TE-averaged spectra of Glu and Gln that were simulated using this approach. The efficacy of separation for C4 protons of Glu and Gln in TE-averaged spectra was the same for different T_2 values but the signal intensities of Gln depended on the T_2 values. This meant that the signals from the C4 protons of Gln were not fully cancelled in the simulation, but they were clearly separated from the C4 protons of Glu due to the difference in chemical shift being 0.1 ppm.

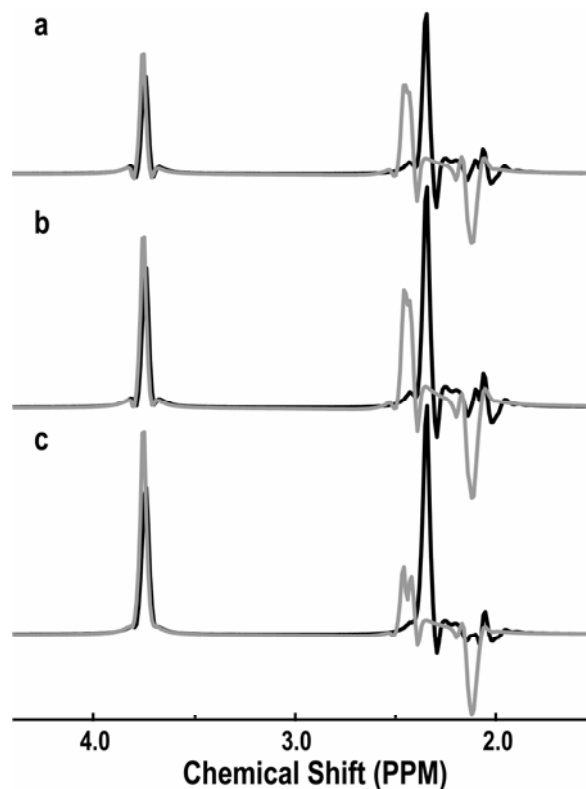


Figure 4.4 Simulation of TE-averaged PRESS spectra of Glu (black) and Gln (grey) with different T_2 relaxation times. TE-averaged PRESS spectra were simulated with 64 steps and T_2 of 100 ms (a) and 150 ms (b), and 128 steps and T_2 of 300 ms (c).

Corrections of Metabolite Levels for Relaxation Times

The metabolite levels were corrected for transverse and longitudinal relaxation times using the values estimated from the empirical data. T_2 correction was applied for levels of Cho, Cr and NAA by multiplying LCModel concentrations and QUEST parameter estimates by a factor $f_{TE} = \exp[TE \cdot (1/T_{2\text{vivo}} - 1/T_{2\text{vitro}})]$, respectively, while the effective TE of the TE-averaged spectra for T_2 acquisition was 113.75 ms, and T_1 correction factor was $f_{TR} = [1 - \exp(-TR/T_{1\text{vitro}})]/[1 - \exp(-TR/T_{1\text{vivo}})]$ for Cho, Cr and NAA. Since the metabolite signals used as a basis for QUEST were ideally simulated without any effect of T_1 and T_2 , the calibration factor only required a calculation of the in vivo T_1 and T_2 values.

Voxel Content Analysis

For the empirical data, the spectral data were referenced to the 3D SPGR image by assuming that there was no movement between the image and spectra acquisition. The FLAIR image was aligned to the corresponding 3D SPGR image. Segmentation of the brain images was performed automatically on the 3D SPGR images using a program that is based on a Markov random field model [59]. The segmented white matter mask was then used to identify voxels which had at least 75% normal appearing white matter. The masks of the region of T_2 hyperintensity were segmented using software developed in our laboratory [71]. The tumor voxels used for the study were restricted to those that had more than 80% within the T_2 hyperintensity. These were the voxels used for comparative analysis to the volunteer and patient data.

Statistics

The statistical analysis was performed using the SPSS software package (Chicago, IL). A P-value of <0.05 was regarded as significant for all the tests. For T_1 studies, nonparametric Wilcoxon rank sum tests were used to test the difference between lesions and normal tissues.

ANalysis Of VAriance (ANOVA) was utilized to determine whether T_2 values and metabolite levels differed between normal, Grade III and Grade IV. To check possible confounding effects of age and sex, these variables were added into the model. However, they did not change the effects of tumor grade and they were insignificant. And then Tukey's honestly significant difference tests were used to test these differences between tumor grades or between T_2 hyperintensity lesion and normal white matter.

The Spearman rank correlation coefficients were calculated to determine the association between the estimated metabolite concentrations of LCModel and QUEST for Cho, Cr and NAA after corrections with T_1 and T_2 relaxation times.

Changes of metabolite ratios or normalized metabolite levels by corrections with T_1 and T_2 relaxation times in each grade and overall was tested using a paired t-test. And then a t-test was used to compare whether the effect of change was dependent on tumor grade.

4.3 Results

The quality of data for the single voxel data was excellent. Figure 4.5 shows an example of the 2D J-resolved and TE-averaged spectra from a volunteer and a patient. Note the

differences in metabolite levels, with a clear reduction in the level of NAA in the voxel from tumor. At the shorter echo times peaks corresponding to Gln, Gln and mI can be observed.

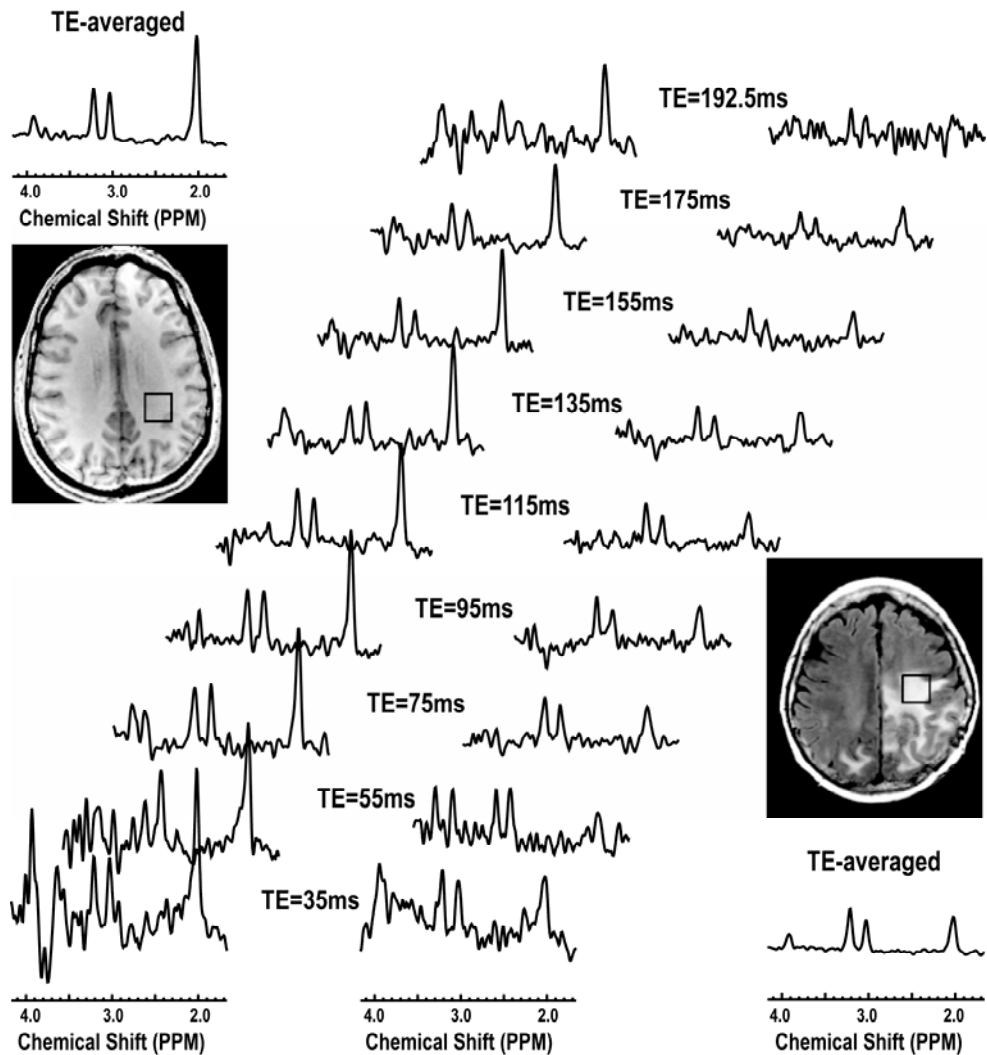


Figure 4.5 Single voxel 2D J-resolved spectra acquired from a volunteer and a GBM patient. The TE-averaged spectra were plotted along the individual echo spectra.

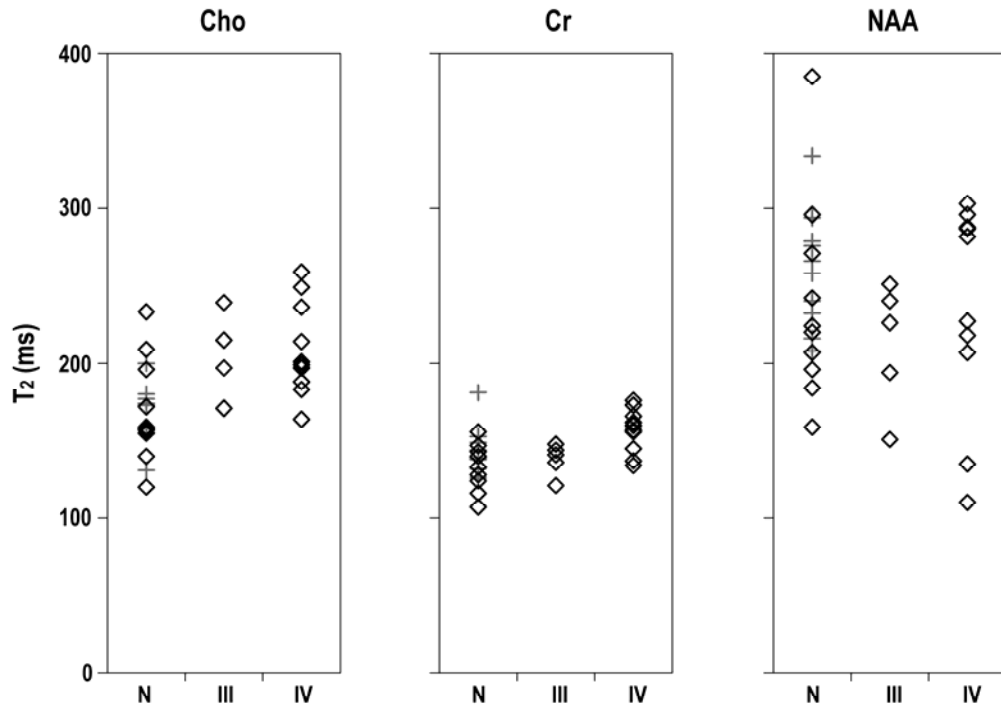
Metabolite T₁ Relaxation times

The T₁ relaxation times of metabolites were available for voxels in 8 volunteers and 8 patients. Values were 1.06±0.11 s (mean ± standard deviation, SD) versus 1.00±0.21 s for Cho, 1.38±0.13 s versus 1.37±0.20 s for Cr, and 1.38±0.13 s versus 1.38±0.21 s for NAA. There was no significant difference between these values.

Metabolite T₂ Relaxation times

For the estimation of T₂ values, there were 10 voxels in WM from volunteers, 3 voxels from NAWM in patients with Grade III glioma and 7 voxels from NAWM in patients with Grade IV glioma. The values in WM and NAWM were not significantly different and so they were pooled as normal white matter VOIs for comparison with tumor voxels. NAWM voxels from patients were treated as independent observations from the values determined in the lesions because they were selected to be clearly distinct from the lesions on T₂ weighted images and did not appear to be correlated with tumor values. The pooled white matter values for Cho were 169±27ms, for Cr were 139±16ms and for NAA were 249±53ms. There were tumor voxels from 5 different patients with Grade III glioma and 10 different patients with Grade IV glioma. The variations in T₂ relaxation values of metabolites for normal white matter and patients were shown in Figure 4.6. The range of NAA T₂ values was quite large, and was not significantly different between normal white matter and tumor voxels. For voxels from Grade III glioma the T₂ values of Cho were 199±29ms but the small sample size meant that this was not significant. For voxels from Grade IV glioma the T₂ values of Cho were 209±30ms and for Cr were 1.57±14ms.

These were significantly different from the values in normal white matter with $P=0.002$ and $P=0.013$ respectively.



	Cho	Cr	NAA
Normal	169 ± 27	139 ± 16	249 ± 53
Grade III	199 ± 29	138 ± 10	212 ± 40
Grade IV	209 ± 30	157 ± 14	235 ± 69

Figure 4.6 T_2 relaxation times of metabolites (ms). The significance was tested between normal white matter and T_2 hyperintensity lesions using Tukey's honestly significant difference test. The diamond in the figure stands for data from patients, while the cross for volunteers. N, III and IV represents for normal white matters from WM in volunteers and NAWM in patients, T_2 hyperintensity lesions in Grade III and Grade IV, respectively.

Metabolite Levels Corrected for Relaxation Times

Examples of TE-averaged spectra from normal parietal WM, Grade III glioma and Grade IV glioma that were quantified by LCModel and QUEST are shown in Figure 4.7.

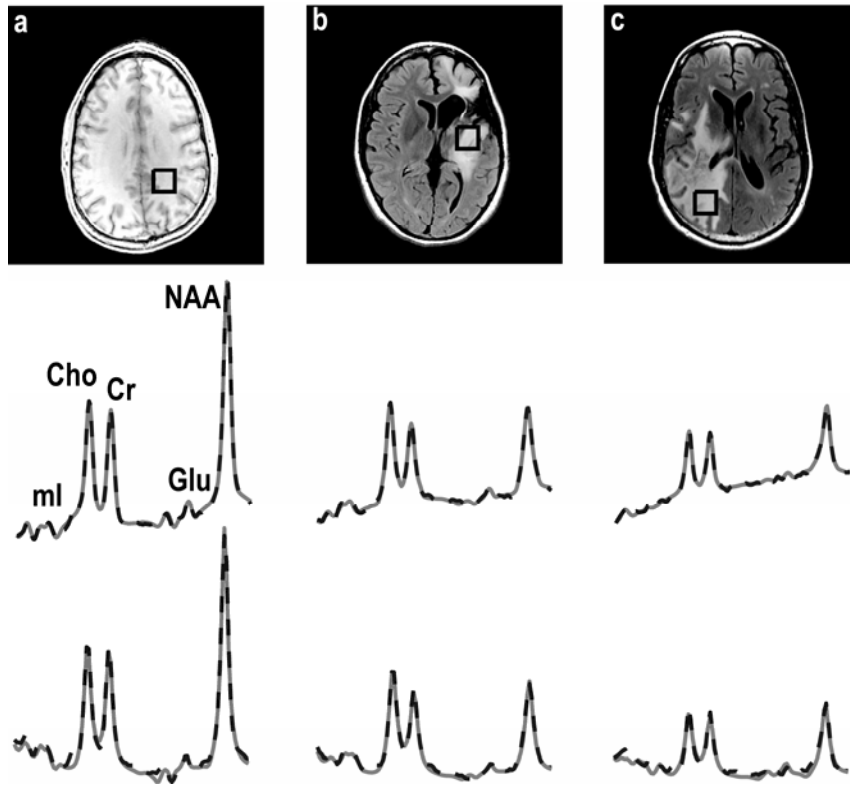


Figure 4.7 TE-averaged spectra quantified by LCModel (middle row) and QUEST (third row) corresponding to the image in a volunteer (a), Grade III (b) and Grade IV (c) patients. The fitted spectra (straight line) were related to the phased spectra (broken line).

Both algorithms fit the data well, with the differences in the plotted spectra being due to the way in which the baseline estimation is performed. Because of the different relaxation times of metabolites in the basis sets for the two methods, due to one being simulated and the other from an in vitro phantom, only the metabolite estimates with T_1 and T_2 corrections were compared between the two methods. The fact that the estimates for Cho, Cr and NAA obtained using LCModel and QUEST were consistent and is

reflected in Figure 4.8 and Figure 4.9. The Spearman rank correlation coefficients were 0.92, 0.96 and 0.97 for Cho, Cr and NAA estimates with $P < 0.001$ for all three metabolites.

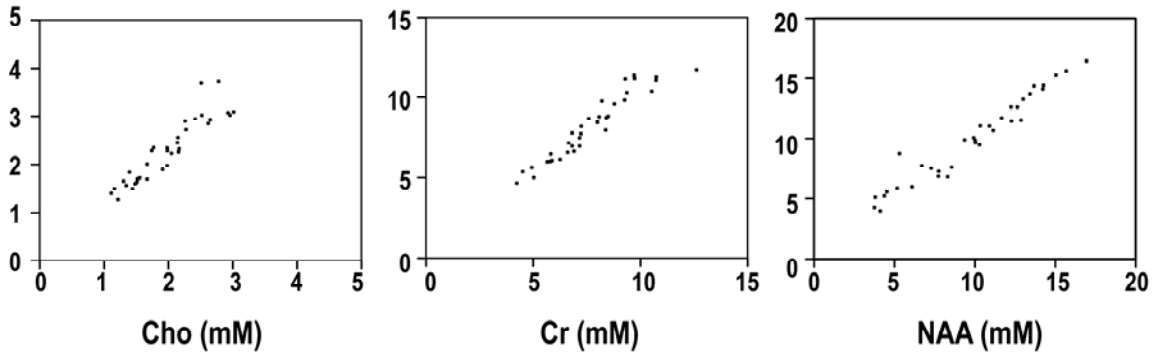


Figure 4.8 Scatter plots of Cho, Cr and NAA calculated from LCModel vs. QUEST for all the voxels in the study. Metabolite concentrations on x-axis represent those from LCModel, while y-axis for the same spectra quantified by QUEST.

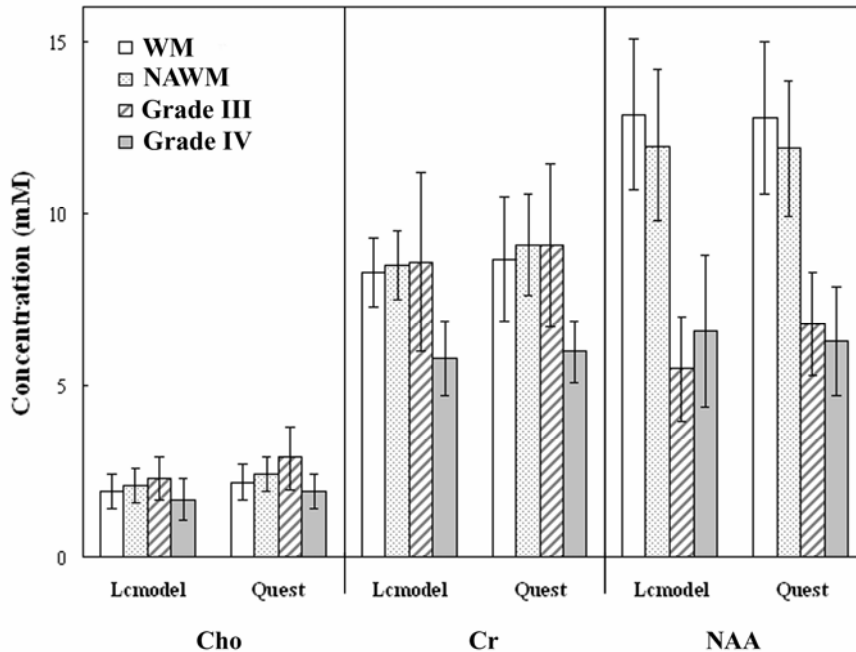


Figure 4.9 Metabolite concentrations of Cho, Cr and NAA quantified by LcModel and QUEST after T_1 and T_2 corrections for each class. The pattern of metabolite changes in each grade was similar in both methods.

The estimates of metabolite levels obtained using QUEST and LCModel were illustrated in Table 4.2 and Table 4.3.

Table 4.2 Concentrations of Cho, Cr and NAA as corrected using empirical T₁ and T₂ relaxation times and expressing the (mean±SD) in mM by QUEST and LCModel. Statistics were evaluated using Tukey’s honestly significant difference tests. N=number of patients. P^a=significance tested between normal white matter and tumor voxels, P^b=significance tested between Grade III and Grade IV.

	QUEST			LCModel		
	Cho	Cr	NAA	Cho	Cr	NAA
Normal (N=20)	2.3±0.5	8.9±1.6	12.4±2.1	2.0±0.5	8.4±1.5	12.5±2.1
Grade III (N=5)	2.9±0.9	9.1±2.4	6.8±1.5	2.3±0.6	8.6±2.6	5.5±1.5
Grade IV (N=10)	1.9±0.5	6.0±0.9	6.3±1.6	1.7±0.6	5.8±1.1	6.6±2.2
		<i>P^a<0.001</i>	<i>P^a<0.001</i>		<i>P^a<0.001</i>	<i>P^a<0.001</i>
	<i>P^b<0.01</i>	<i>P^a<0.001</i> <i>P^b<0.005</i>	<i>P^a<0.001</i>		<i>P^a=0.001</i> <i>P^b<0.01</i>	<i>P^a<0.001</i>

Table 4.3 Levels of mI, mIG, Glu and Gln as quantified by QUEST and LCModel (mean±SD). Statistics were evaluated using Tukey’s honestly significant difference tests. N=number of patients. P^a=significance tested between normal white matter and tumor voxels, P^b=significance tested between Grade III and Grade IV.

	QUEST				LCModel		
	mI	mIG	Glu	Gln	mI	Glu	Gln
Normal (N=20)	2.8±0.9	3.6±1.1	2.3±0.5	2.5±0.9	5.9±1.5	6.3±1.9	2.2±0.3
Grade III (N=5)	3.8±1.2	5.1±1.8	3.1±0.8	2.7±0.1	10.4±2.4	8.4	2.4±0.6
			<i>P^a<0.05</i>		<i>P^a<0.005</i>	<i>n/a</i>	
Grade IV (N=8)	2.8±1.7	3.3±1.6	2.1±0.5	2.3±0.7	6.4±2.7	5.4±1.5	1.5±0.5
			<i>P^b<0.05</i>		<i>P^b<0.05</i>		<i>P^b=0.05</i>

Cho and Cr were clearly increased in Grade III gliomas but decreased in Grade IV gliomas relative to normal brain. The differences in Cr between Grade III and IV lesions

was statistically significant ($P < 0.01$). The concentrations of NAA were reduced in both tumor grades ($P < 0.001$). Compared with those in normal white matter, the levels of ml estimated using LCModel were increased in Grade III gliomas ($P = 0.002$) and statistical significantly different from Grade IV ($P = 0.017$). No significance was found for the results using QUEST. The levels of Glu were significantly increased in Grade III from QUEST ($P = 0.047$), and the difference between Grade III and Grade IV for Gln was marginally significant for LCModel ($P = 0.05$).

Differences in Metabolite Ratios With & Without Corrections

Since the time available for data acquisition is relatively short in the case of in vivo MRSI data, the difference in T_2 relaxation times may contribute to the distinction between tumor and normal tissue. To investigate the magnitude of this effect we considered the differences in metabolite ratios for our single voxel data with and without correction for relaxation times. The metabolite ratios with and without corrections of relaxation values were shown in Table 4.4 and Table 4.5. In all cases the Cho/Cr, NAA/Cr and Cho/NAA ratios in tumors were larger than in normal white matter for the uncorrected compared to the corrected values, and the normalized metabolite levels of Cho and Cr in the two grades were higher than the corresponding corrected values. This implies that the differential in relaxation times between Cho, Cr and NAA increases the contrast for spectra in tumor relative to normal tissue when there is a higher degree of T_2 -weighting. Statistical significance was found for the interaction between the correction and tumor grade for all the metabolite ratios with $P < 0.001$ except for the normalized levels of Cho which was significantly difference between before and after corrections.

Table 4.4 Relative metabolite ratios (mean±SD). The ratios of Cho/Cr, NAA/Cr and Cho/NAA estimated by LCModel were compared with the same data after the corrections of T₁ and T₂ values. N, III and IV represents for normal white matters from WM in volunteers and NAWM in patients, T₂ hyperintensity lesions in Grade III and Grade IV, respectively.

	Cho/Cr		NAA/Cr		Cho/NAA	
	Before	After	Before	After	Before	After
N	0.36±0.05	0.24±0.03	1.84±0.23	1.51±0.19	0.20±0.04	0.16±0.03
III	0.47±0.13	0.28±0.08	0.80±0.37	0.71±0.33	0.70±0.35	0.47±0.23
IV	0.46±0.09	0.29±0.06	1.23±0.35	1.14±0.33	0.42±0.23	0.29±0.16

Table 4.5 Normalized metabolite levels. The metabolite levels in gliomas determined by LCModel were normalized to the corresponding mean metabolite levels in the normal white matter and were then compared with the same data after corrections for T₁ and T₂ values. III and IV represents for T₂ hyperintensity lesions in Grade III and Grade IV, respectively.

	Cho _n		Cr _n		NAA _n	
	Before	After	Before	After	Before	After
III	1.30±0.36	1.15±0.32	1.03±0.31	1.03±0.31	0.41±0.11	0.44±0.12
IV	0.98±0.34	0.85±0.29	0.77±0.14	0.70±0.13	0.52±0.17	0.53±0.18

4.4 Discussion

Gliomas are the most common primary brain tumor and primarily affect white matter. The ability to map out the spatial extent of tumor relative to normal appearing white matter is dependent upon both the variations in absolute concentrations of metabolites and in degree of T₁ and T₂ weighting in any given acquisition. Designing the most appropriate acquisition parameters for obtaining multi-voxel MRSI data requires the measurement of these variables in localized spectra from normal volunteers and patients with brain tumors.

The methods used in this study to estimate relaxation times and metabolite levels had several benefits over previous approaches. Firstly, the individual spectra that used for T_2 fitting were the mean of three spectra with a TE difference of 2.5 ms, which increased the signal-to-noise ratio (SNR), as shown in Figure 4.5. This can be expected to provide more reliable estimates of the T_2 values. Note that J-coupling differences within these three averaged spectra would have been very small and were therefore ignored. The second benefit in using the 2D refocused sequence is that the effective echo time was relatively long would therefore reduce the effects of macromolecules and decrease the contribution of J-coupled resonances of Glu located underneath the NAA peak. Although the last echo in the T_2 fit (TE = 190 ms) was not long enough to cover the complete signal decay, more points were involved in our study than in previous publications [52, 53, 72]. Thirdly, since the TE-averaged spectra have flat baseline, the possibility of overestimating T_1 values should be relatively small.

A limitation of the approach used was that the weak signal intensities of Glu and mI translated into a large variation and uncertainty in peak intensities for individual echo times and so the T_1 and T_2 of these metabolites were not able to be evaluated. To estimate the T_2 values of metabolites such as mI, Glu and Gln with complex J coupling patterns would require a metabolite specific spectral editing sequence [73, 74].

Several studies have assessed the T_1 and T_2 relaxation times of normal brain metabolites within different regions of the normal brain and at different field strengths. T_1 values were significantly longer at 3 T than at 1.5 T [53], but were not reported as showing major regional variability [72]. A distinct correlation was reported between T_2 and relative WM/GM composition for NAA and Cr-CH₃ [72]. This suggests that the T_2

of these intracellular metabolites is more affected by the integrity and composition of the tissue, whereas T_1 values are influenced by molecular tumbling, reflecting the viscosity of the medium. The T_1 relaxation times of metabolites from normal brain that were observed in our study are similar to those previously published [72], and were not significantly different from the T_1 values in gliomas. While this is consistent with observations made at 1.5 T [67] it may also be due to the limited number of cases in the study.

T_2 relaxation times in Cho and Cr were statistically significantly longer in Grade IV gliomas compared with those in normal white matter. The Cho peak resonates at 3.20 ppm and represents choline, phosphocholine (PC) and glycerophosphocholine (GPC). Previous studies have shown that a switch from GPC to PC is associated with glioma malignancy [33, 34]. This could be one reason why the observed T_2 of Cho increases in tumor. The higher T_2 of Cr in Grade IV glioma may also be associated with the changes of metabolite composition, associated with the increase of phosphocreatine (PCr) to Cr. Note that PCr contains a high energy phosphate bond, which transfers to ADP via the breakdown of PCr to Cr and that reduced PCr has been observed in gliomas [75]. This suggests that there is a high energy requirement for maintaining the growth of cells in gliomas. In the previous studies that were performed at 1.5 T, either the T_2 relaxation time of NAA and Cr were reported to be shorter in high grade gliomas [9] or the T_2 values of all of the singlets were shorter in the tumor [67]. The differences observed in our study may be because of the higher field strength used, the larger number of spectra employed in calculating the T_2 values or the application of a more effective statistic test, Tukey's honestly significant difference test, instead of a regular student t-test.

The elevation of the Cho peak and the reduction of the neuronal marker NAA are considered to be characteristic of gliomas. Our results suggest that the changes in Cho and Cr peak heights in gliomas are partially caused by T_2 effects and partially by changes in absolute concentrations, and that there is a significant interaction exists between corrections for relaxation times and tumor grade. Longer T_2 relaxation value of Cho in gliomas means that the ratio of Cho/NAA that is observed in long echo spectra is larger than that in short echo spectra and relatively larger than values in normal white matter at the same echo time. This is consistent with the previous observations at 1.5 T [76].

Two different algorithms were used to quantify the metabolic profiles in our study. LCModel uses a constrained regularization method accounting for the phase, lineshape and baseline [29]. QUEST differs from the LCModel in the method used for fitting the baseline, and is sensitive to whether a common extra-damping factor or different metabolite extra-damping are estimated [30]. In our case, we used a simulated basis set and found better results when a unique common extra-damping was estimated. Since there is little penalty for the contamination of macromolecules and lipids in the TE-averaged spectra [65, 66, 77], we used the QUEST quantification algorithm without background adjustment, but weighted the first 20 points with a quarter-wave sinusoid and discarding the first points to reduce the influence of broad resonances underlying metabolites of interest. The results of the estimates of Cho, Cr and NAA showed a very high correlation coefficient between the two methods. Compared with LCModel, QUEST gives more flexibility and reliability but has more subjective interaction, which requires the use of more prior knowledge.

As expected, there was a striking reduction in NAA for all the grades of glioma. The higher metabolite levels in Grade III compared to Grade IV glioma suggested that the levels in the higher grade lesions may be influenced by partially voluming with necrosis [78]. The mI is predominantly located within astrocytes and is a precursor for the phosphatidylinositol (PI) second messenger system [40] that is also presumed to act as an osmoregulator. It resolves as an apparent doublet at 3.6 ppm in TE-averaged spectra, which cannot be separated from the Gly peak which resonates at 3.56 ppm. Compared to the simulation, the doublet of mI from the *in vitro* solution had different effective T_2 values, which resulted in the difference of fitting outcomes between LCModel and QUEST. Changes that are associated with mI and reported in the literature show increases in mIG [8] and its ratio to Cr [41] in low-grade astrocytomas but decreased in high grade. In our results, the mI estimated from LCModel was statistically significantly higher in Grade III compared to normal white matter.

Although averaged 2D J resolved spectra have less macromolecule contamination compared with short echo acquisitions, macromolecules are always associated with gliomas and result in more uncertainty of small peaks such as Glu/Gln. The changes observed with LCModel and QUEST had a similar pattern of changes. Previous studies have showed that a significant increase in Glx was found in oligodendrogliomas and was used to discriminate them relative to low-grade astrocytomas [10]. The increase in Glu that was observed in the Grade III glioma considered in our study is consistent with the observation that glioma cells may secrete Glu, resulting in an increase in extracellular Glu [37, 38]. Increased Glu could be also associated with inflammation in the peritumor tissues since activated microglia and brain macrophages express high affinity glutamate

transporters [79] and stimulates tumor cell proliferation. Gln was also slightly increased in Grade III but the change was not statistically significant. Because Gln acts as an suppressor for apoptosis, it could contribute to block apoptosis induced by exogenous agents, such as radiation treatment and chemotherapy, and also promote tumor proliferation [39]. As predicted by the simulation, the signal intensities of Glu and Gln in the TE-averaged spectra depend on the T_2 values. The pattern of changes in Gln for gliomas would be much clearer if estimates of the T_2 of Glu and Gln were obtained. Although mobile lipids and lactate are also strongly associated with the higher grade of gliomas, it was not possible to distinguish Lac from lipid in the TE-averaged spectra. It is for this reason that we did not attempt to quantify these metabolites in the current study.

It is well known that gliomas are extremely heterogeneous. The regions of T_2 hyperintensity on the T_2 -weighted image may include edema, gliosis, inflammation, active tumors or treatment effects. While we chose to consider large tumors and required that 80% of the voxel considered was in the tumor, the effect of heterogeneity is a limitation in terms of the results of our study. Another factor that may have influenced the data is that there were four different grades of gliomas considered, which arise from different glial cells, such as oligodendrocytes and astrocytes, and could therefore result in different metabolite characterizations [10].

The results of this study demonstrated the differences in metabolite relaxation times and in metabolite concentrations both between normal white matter and tumor and between glioma of Grade III and Grade IV. These data suggest that the contrast in metabolite ratios between tumor and normal tissue would be greatest at longer echo times and, if the signal to noise is high enough, the use of long echo times may have

benefits over short echo times. Our results are encouraging but further studies are required to provide more information about the spatial variations in metabolite concentrations within tumor and peritumor regions using multi-voxel acquisitions in populations of patients with gliomas.

Chapter 5: Three-dimensional J-resolved H-1 magnetic resonance spectroscopic imaging of volunteers and patients with brain tumors at 3 T

This chapter presents a method that combines 2D J-resolved spectroscopy with three spatial dimensions MRSI to measure J-coupled metabolites of Glu, Gln, mI and Lac in the brain and to simultaneously obtain T_2 values of Cho, Cr and NAA.

5.1 Rationale

The study presented in the previous chapter has employed 2D J-resolved spectroscopy to measure the transverse relaxation times of uncoupled resonances, Cho, Cr and NAA. It also allowed the separation of J-coupling information from chemical shift and improved distinction between Glu and Gln in the TE-averaged spectra [65]. This method has been implemented as both a single voxel acquisition with 8 cm³ spatial resolution [65] and a 2D J-resolved MRSI pulse sequence [80] with one spatial dimension being acquired using phase encoding and the other using a flyback echo-planar trajectory [81] at 3 T. The latter was acquired with 1.8 cm³ nominal spatial resolution. The flyback trajectory is valuable here because it speeds up the acquisition by mapping one spatial dimension and the spectral dimension during a single readout. Data collected in the positive lobes of the readout gradient are used, while the negative lobe (rewind lobe) of gradient returns to the starting of k-space as soon as possible (Figure 5.1). The TE-averaged PRESS has been

applied to brain tumors in a single voxel acquisition mode in the previous chapter, however, the extreme heterogeneity of gliomas means that multi-voxel spectroscopic imaging with higher spatial resolution is required to provide more detailed information within the tumoral and peritumoral regions.

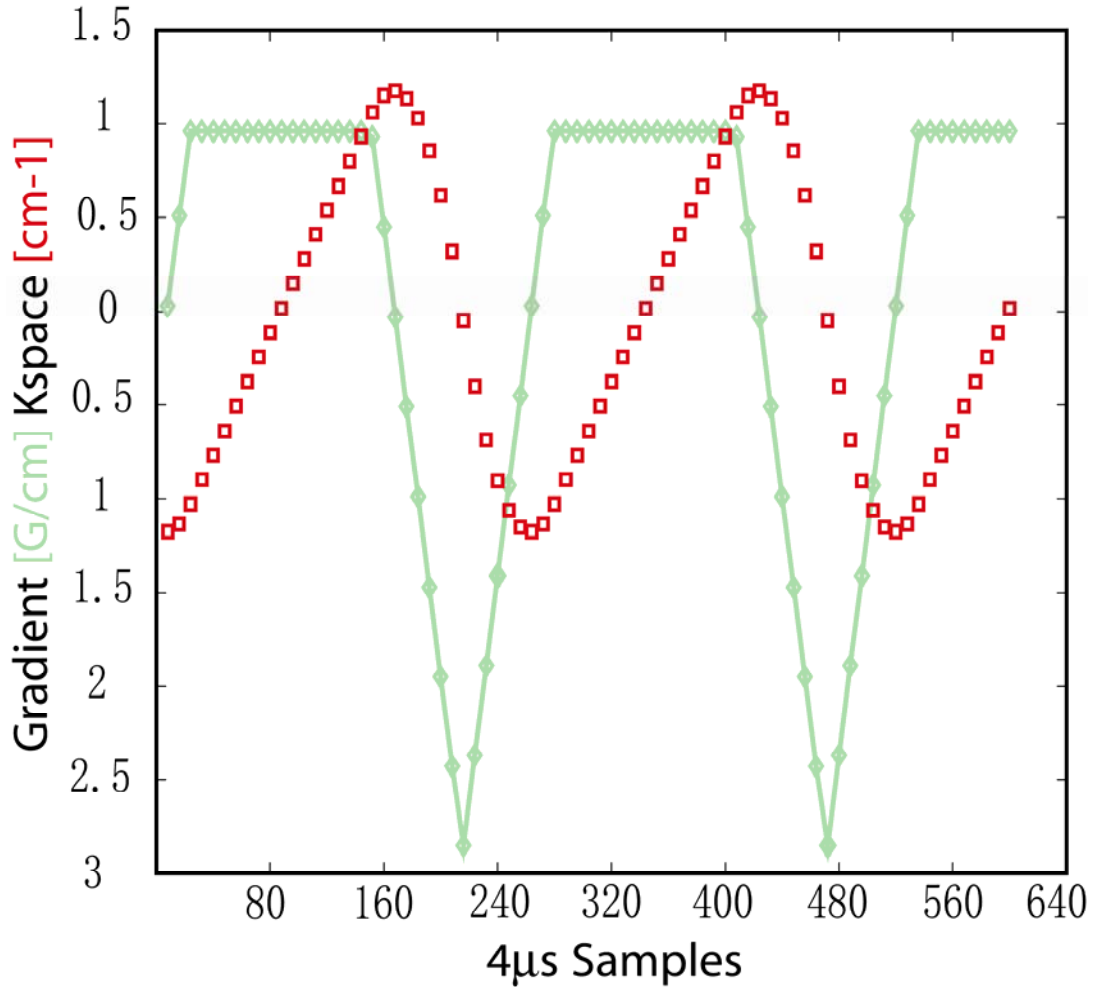


Figure 5.1 Flyback echo-planar trajectory [81]. The green line represents the gradient form, and red dotted line represents the position in k-space. Data collected in the positive lobes of the readout gradient are used, while the negative lobe (rewind lobe) of gradient returns to the starting of k-space as soon as possible.

The current section aims to develop a new acquisition scheme that can provide data within a clinically feasible acquisition time and to develop post-processing methods to interpret 2D J-resolved PRESS MRSI data with three spatial dimensions. This includes the development of strategies for improving the quantification of metabolites from these spectra using prior information concerning the J-coupling of metabolites such as Glu, mI and Lac, as well as correcting for relaxation times of metabolites whenever possible.

5.2 Methods

Simulated Data

PRESS spectra of Glu and Gln with TE values starting at 35 ms in 6 steps of 40 ms were simulated using GAMMA software [70] using prior knowledge of peak locations and J-coupling constants [64]. The spectra were created with 1024 spectral points and a spectral width of 2000 Hz. A 4-Hz Lorentzian apodization, zero filling to 2048 points and Fourier Transform were applied and the resultant data were averaged in the t_1 dimension.

MR Data

All the empirical studies were performed using a transmit body coil and eight-channel phased array coil for signal reception with a 3 T GE Signa scanner. The MR scans included the acquisition of both anatomic and spectroscopic imaging data.

Anatomical MR images comprised T_1 -weighted sagittal scout images (TR/TE = 70/2 ms at 3 T), axial FLuid Attenuated Inversion Recovery (FLAIR) (TR/TE/TI

=10002/127/2200 ms) and T₁-weighted SPOiled GRAdient Echo (SPGR) image (TR/TE =26/3 ms). In addition, proton density-weighted gradient echo images were acquired using the manufacturer provided parallel imaging calibration sequence to obtain the estimates of coil sensitivities (TR/TE = 150/2 ms) for the combination of the spectral data from each of the eight channels.

The J-resolved spectra were localized in three spatial dimensions using PRESS volume selection. In order to show the reliability of the relative position of metabolites, a single-voxel 2D J-resolved acquisition was performed in the metabolite phantoms with 2000 Hz spectral width and 1024 spectral point, resulting in spectral resolution in the F₂ dimension of ~1.95 Hz. The increment delay ($t_1/2$) of the J-resolved acquisition was added before and after the final refocusing RF pulse in the PRESS sequence to encode t_1 . The initial echo time was 35 ms. Six increments in the t_1 dimension were acquired over a 25 Hz spectral bandwidth to yield an F₁ resolution of 4.17 Hz per point.

The 3D J-resolved MRSI data were acquired utilizing a flyback echo-planar gradient trajectory [81], which allowed the encoding of one spatial dimension and the spectral dimension during a single readout in order to speed up the acquisition time. The flyback echo-planar gradient was designed to provide a spatial resolution of 1 cm and was applied in the right/left direction for an FOV of 16 cm (16 spatial points). The spectral data were collected with 712 spectral points and 988 Hz spectral width, which provides ~1.39 Hz spectral resolution per point in the F₂ dimension. The 3D spectral array size was 16 x 12 x 8 (RL x AP x SI) and the nominal spatial resolution was 1 cm³. With a TR of 1.2 s and a NEX of 2, the total acquisition time for 3D J-resolved MRSI was 23 min.

Study Population

An in vitro basis set from phantoms containing individual metabolites (50 mM Cho, 50 mM Cr, 50 mM NAA, 100 mM Glu, 100 mM Gln, 200 mM mI and 200 mM Lac) was prepared by performing single voxel 2D J-resolved acquisition on each phantom. To test the hypothesis that the 2D spectral cross-peaks of Lac can be separated from the overlapping lipids, the Lac phantom was covered with a thick piece of bacon and data was acquired using single voxel 2D J-resolved acquisition.

A standard GE MRS phantom (12.5 mM NAA, 10 mM Cr, 3 mM Cho, 12.5 mM Glu, 7.5 mM mI and 5 mM Lac), six healthy volunteers and four patients with different kinds of primary brain tumors were included in the study. Patient diagnoses were: one undefined glioma (patient A) and three glioblastoma multiforme (GBM) patients (patients B, C and D). To test the reproducibility of such data, we scanned the head phantom and two of the volunteers twice while positioning the excited volumes in similar regions.

Postprocessing and Analysis

Postprocessing was performed on a Linux Cluster in our laboratory [13 Sun Fire V60x Intel Xeon servers (2 x 2.8 GHz, 1GB Memory), 4 Sun Fire V20z AMD Opteron servers (2 x 2.4 GHz, 4GB Memory)] running Sun's N1 Grid Engine. Spectral arrays from the eight-channel coil were processed in parallel on separate CPUs and the signals were combined using in-house developed software that weighted the data by their coil sensitivities [12]. Relative metabolite ratios were quantified using the LCModel package [29] for voxels within the PRESS box (8x8x4) on a single SunBlade 1000 Workstation (Sun Microsystems, Santa Clara, CA).

The single voxel data were processed with phase and frequency corrections using the internal water signal, apodized with a 4-Hz Lorentzian function, zero filled to 2048 points and fast Fourier Transformed (FFT) in the t_2 dimension. A second FFT was applied in the t_1 dimension and a 45° rotation of the 2D spectra was performed to separate chemical shift and J-coupling information.

The 3D J-resolved MRSI data that were acquired using flyback readout trajectory were reordered to correspond to a rectilinear grid with resampling and phase corrections [81], followed by processing with first-point phasing and apodization in the t_2 domain. The eight-channel data were then combined in the t_2 domain. To estimate relative metabolite levels, the combined data were averaged in the t_1 domain and then quantified using the LCModel package. Spectra were fitted between 4.0 ppm and 1.0 ppm. Metabolite ratios included in the analysis were those with relative Cramér-Rao lower bounds (CRLB) lower than 5% for Cho, Cr and NAA, 20% for mI and Glu, and 25% for Glx (Glu+Gln). The peak heights of Cho, Cr, NAA and Glu were computed automatically using in-house software for each voxel within the excited region from the TE-averaged data [28]. The SNR of individual metabolites were estimated by dividing the heights of the peaks by the standard deviation of the noise from the peak-free region at the right end of the spectrum.

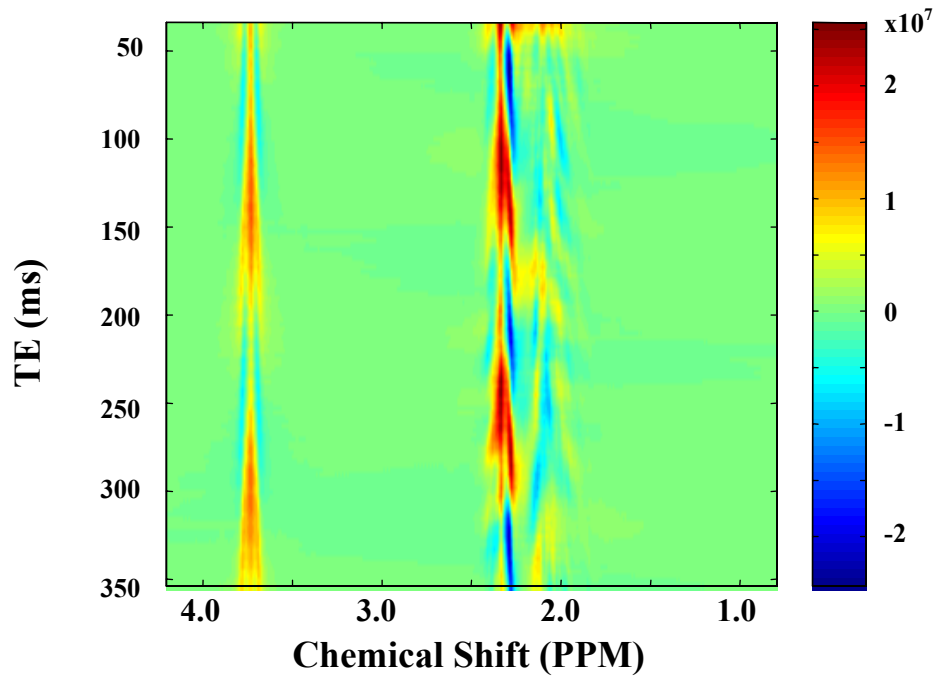
Six different echo-time spectra of the 3D J-resolved MRSI were each processed prior to averaging in the t_1 dimension to estimate the T_2 of each metabolite. The peak heights of Cho at 3.22 ppm, Cr-CH₃ at 3.02 ppm and NAA at 2.02 ppm were estimated from each echo-time spectra [28], and then fitted to a single exponential function to calculate T_2 metabolic relaxation times using the SAGE software packageTM (General Electric,

Milwaukee). The 2D spectra with three spatial dimensions were generated by applying a second FFT and 45° rotation in the t_1 dimension. Only the T_2 values with variances of the fit residue smaller than 10% were included in the analysis.

The coefficient of variance (CV) for reproducibility was calculated using the formula, $CV = \sqrt{\sum_{i=1}^m SD_i^2 / m} / \bar{X} \times 100\%$, where the SD_i are the standard deviations of normalized peak heights in the voxel between two measurements, \bar{X} is the mean of the total voxels, and m is the number of the voxels. In addition, the CV's for the T_2 values of metabolites in the phantoms were calculated using the standard deviation divided by the mean.

The 3D J-resolved MRSI data were referenced to the 3D SPGR image by assuming that there was no movement between the image and spectra acquisition. The FLAIR image was aligned to the corresponding 3D SPGR image. Segmentation of the 3D SPGR brain images were performed automatically using a hidden Markov random field model with an expectation-maximization algorithm [59]. The segmented white matter mask was then used to identify voxels that had at least 85% normal appearing white matter or 85% grey matter. The tumor lesions were restricted to the voxels within the T_2 hyperintensities defined by T_2 -weighted images. To avoid errors in identification of normal voxels, the edges of the PRESS box and ventricles were excluded from the analysis. Voxels that satisfied the above criteria were used for comparative analyses in the volunteer and patient data. Nonparametric Wilcoxon rank sum tests were used to assess the differences for the metabolic relaxation times, with a P-value of 0.05 considered to be significant.

Glu



Gln

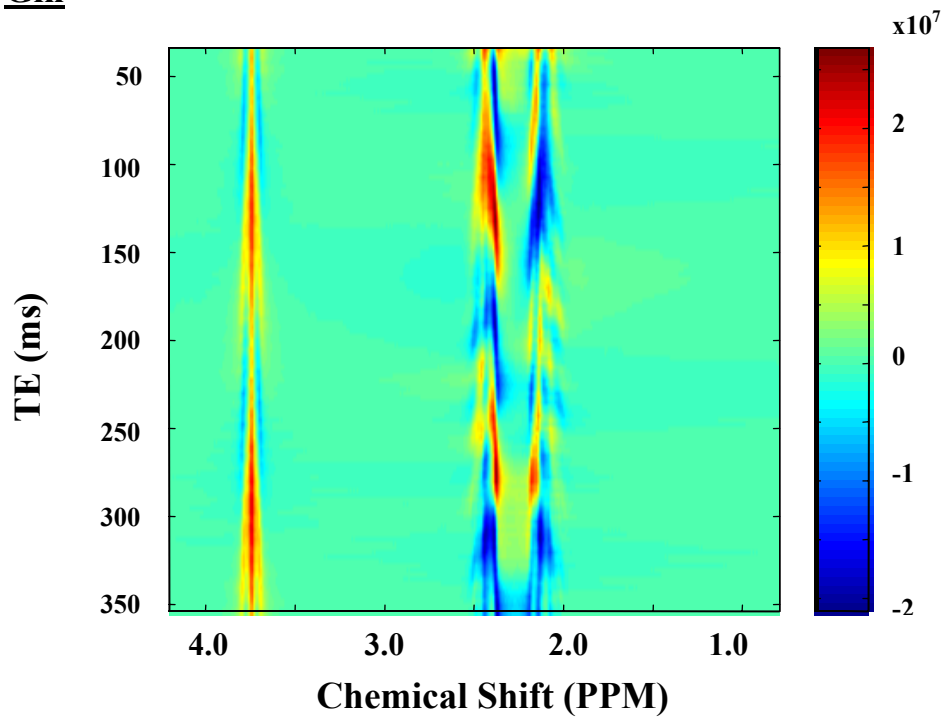


Figure 5.2 Glu and Gln simulation using GAMMA along with the increase of TE.

5.3 Results

The oscillating coupling patterns for ^2CH and $^4\text{CH}_2$ protons of Glu and Gln appear as pseudotriplets in the simulation (Figure 5.2), which makes it possible to leave only the center signal after averaging spectra with different echo times. The TE-averaged spectra of GAMMA simulations and single voxel phantom studies for pure Glu and Gln are shown in Figure 5.3. The $^4\text{CH}_2$ Glu resonance is clearly resolved from the $^4\text{CH}_2$ Gln resonance both in simulations and in phantom studies with a chemical shift difference of 0.1 ppm.

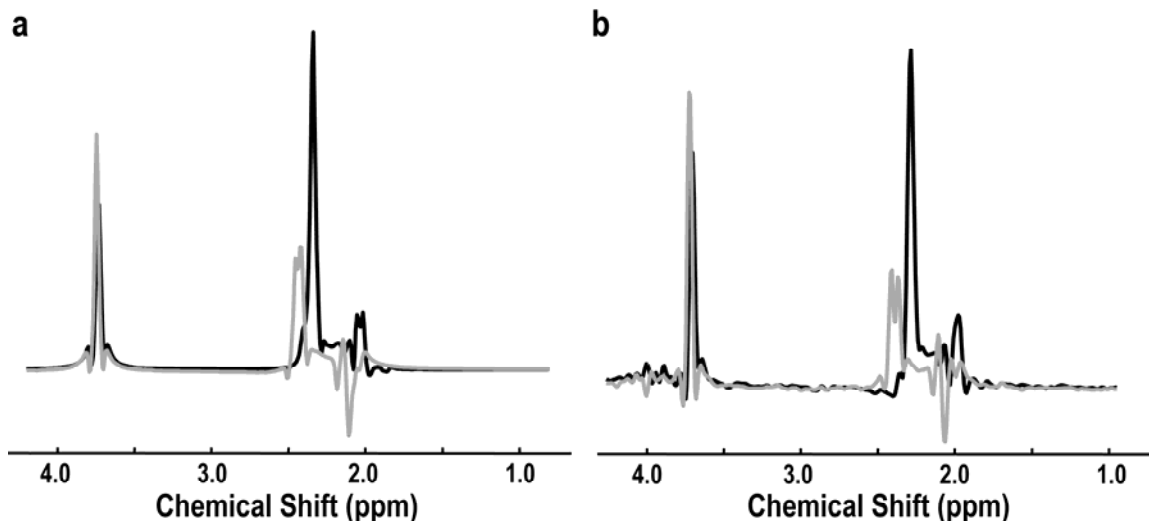


Figure 5.3 Simulated (a) and phantom (b) TE-averaged PRESS spectra of Glu (black) and Gln (grey). The $^4\text{CH}_2$ Glu resonance is clearly resolved from the $^4\text{CH}_2$ Gln resonance in both simulations and phantom studies with a chemical shift difference of 0.1 ppm

Figure 5.4 shows the 2D J-resolved spectra recorded from the lactate phantoms with two localizations, one in the center of the lactate phantom (voxel A) and the other contaminated with a part of bacon (voxel B). The J cross-peaks caused by the methyl

group of lactate in the 2D spectrum were separated from the overlapping lipid peaks, which were compared with the 1D spectra extracted from $J = 0.0$ Hz (TE-averaged spectrum). For comparison with resonances without J couplings, the TE-averaged spectrum of the NAA phantom was co-plotted with the lactate spectrum. As expected, the doublet resonances of Lac were cancelled in the TE-averaged spectra, but successfully displayed in the 2D spectrum.

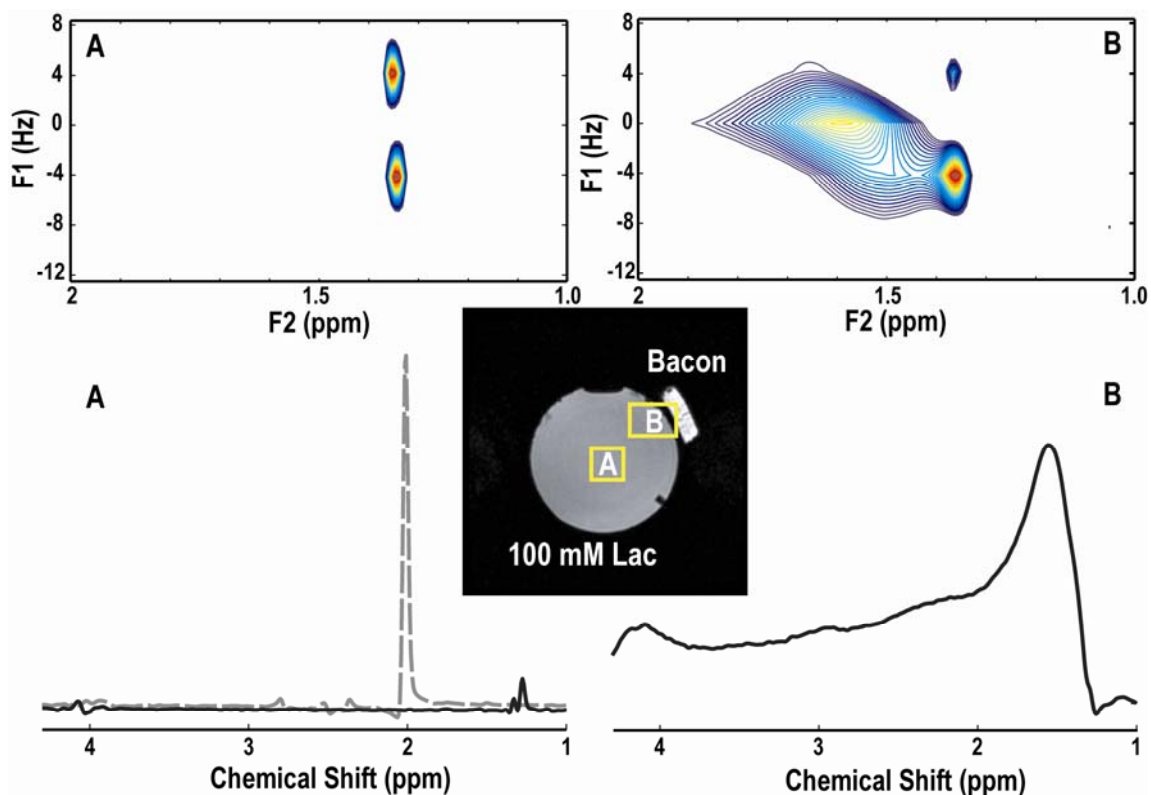


Figure 5.4 Single voxel 2D J -resolved spectra from a 100 mM Lac phantom with two localizations (voxel A and voxel B). The 2D spectrum and the corresponding 1D spectrum were plotted. The TE-averaged spectra from 50 mM NAA phantom (dotted line) were co-plotted with the Lac spectra. Voxel A was acquired with the voxel size of 8 cm^3 , a NEX of 4 and a TR of 10 s (total acquisition time ~ 4 min), and Voxel B was acquired with voxel size of 20 cm^3 , a NEX of 2 and a TR of 1.2 s (total acquisition time ~ 2 min).

The estimates of reproducibility were obtained using a voxel-by-voxel comparison of the peak heights of different metabolites. The values of CVs were 4% for Cho, 5% for Cr, 6% for NAA and 9% for Glu in the phantom, compared with 15%, 16%, 12% and 35% in vivo. The CVs were relatively higher in vivo, especially for Glu.

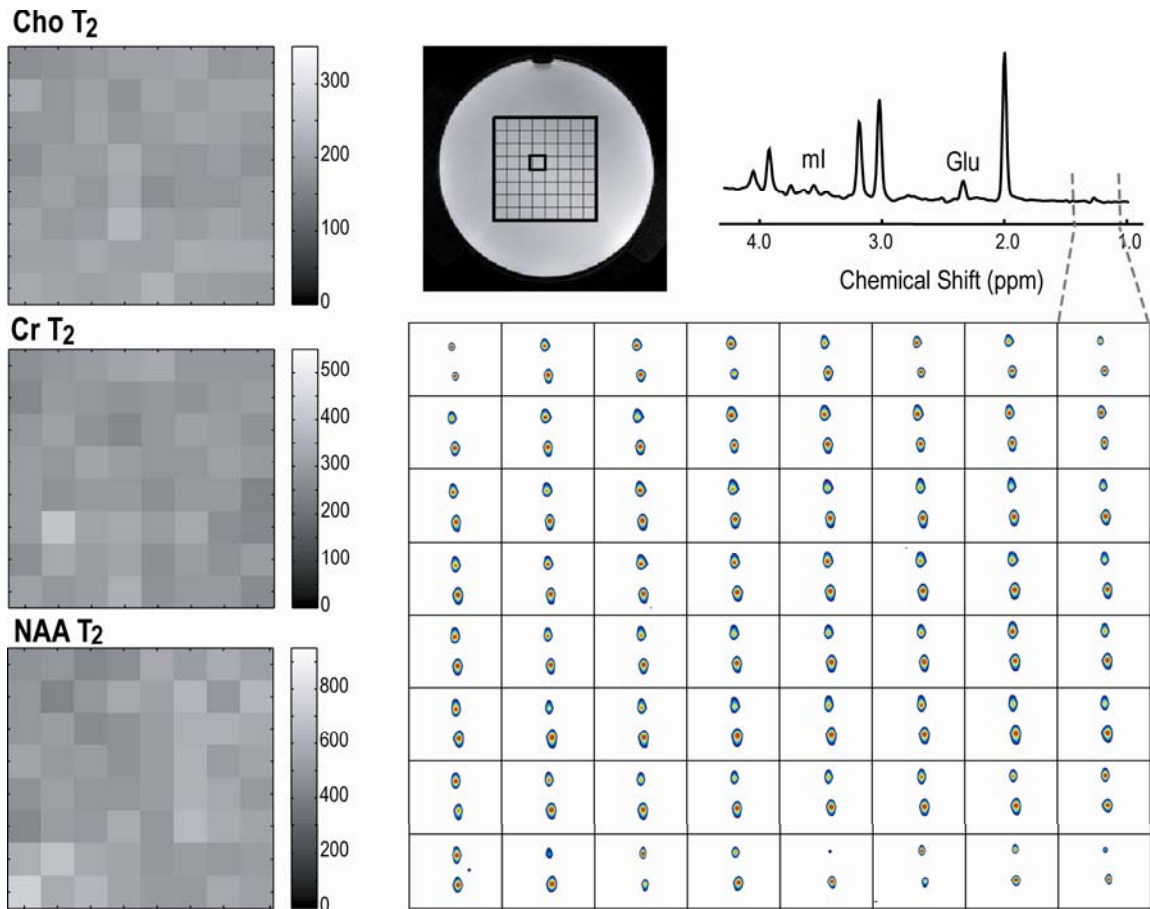


Figure 5.5 3D J-resolved MRSI acquired from the head phantom. The cross-peaks of Lac in the 2D spectra with the region between $F2 = 1.5$ ppm and $F2 = 1.0$ ppm were displayed in the 3D spatial dimensions, which was compared with the $J=0$ Hz spectra extracted from the 2D spectra (TE-averaged spectra). The T₂ values of Cho, Cr and NAA in the phantom were distributed uniformly in the spatial dimension.

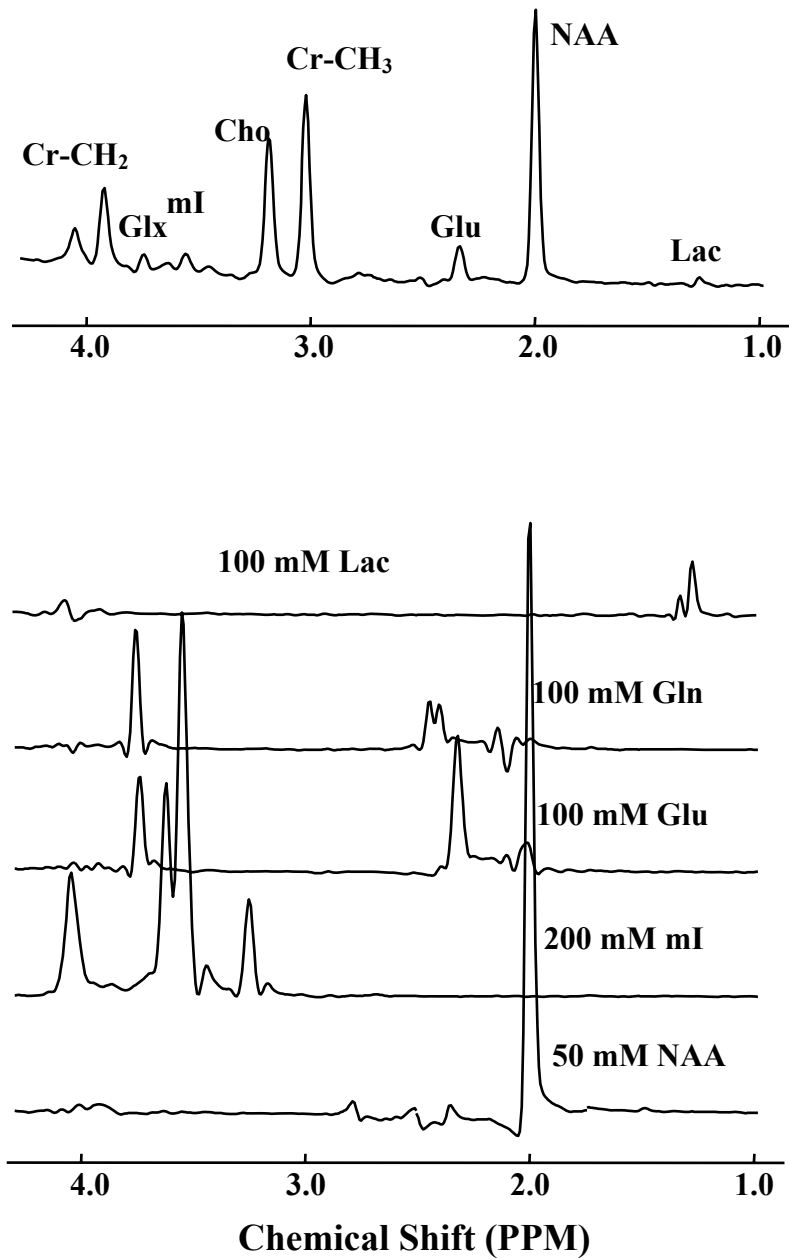


Figure 5.6 The TE-averaged spectrum of a standard head phantom along with the spectra of metabolic phantoms.

Figure 5.5 illustrates the result of 3D J-resolved MRSI data acquired from the phantom and TE-averaged spectra are aligned with the metabolic phantoms in Figure 5.6. The TE-averaged spectra offered an unobstructed single Glu peak and a doublet of mI. The cross-peaks of Lac in the 2D spectrum in the region between $F_2 = 1.5$ ppm and $F_2 = 1.0$ ppm were distinctly visualized within the three spatial dimensions despite the fact that there were only 6 echo times recorded. The T_2 values of Cho, Cr and NAA in the phantom were 194 ± 14 ms, 296 ± 26 ms and 550 ± 72 ms (mean \pm SD). With CVs of 7% for Cho, 9% for Cr and 13% for NAA, the T_2 values of metabolites were markedly uniform in the spectral array and could be used to reflect the regional T_2 difference in vivo.

In vivo TE-averaged MRSI data were obtained with good SNR over the entire spectral array. The SNR values of Cho, Cr, NAA, and Glu in volunteers were 17.0 ± 4.9 , 15.8 ± 4.5 , 33.4 ± 11.5 and 4.3 ± 2.0 , respectively. An example of white matter and grey matter voxels from the volunteer acquired with 3D J-resolved MRSI is given in Figure 5.7. Compared with each individual echo spectra, the TE-averaged spectra had flat baselines but maintained the metabolites that had relatively shorter T_2 values and thus provided more accurate quantification. The Glu/Cr levels were obviously higher in the grey matter voxel than those in white matter from the metabolic maps shown in Figure 5.7. The ratios of mean metabolite levels in grey matter relative to white matter from 6 volunteers without corrections of relaxation times were 1.0 ± 0.2 for Cho, 1.2 ± 0.1 for Cr, 0.9 ± 0.1 for NAA, 1.3 ± 0.2 for Glu and 1.2 ± 0.2 for mI.

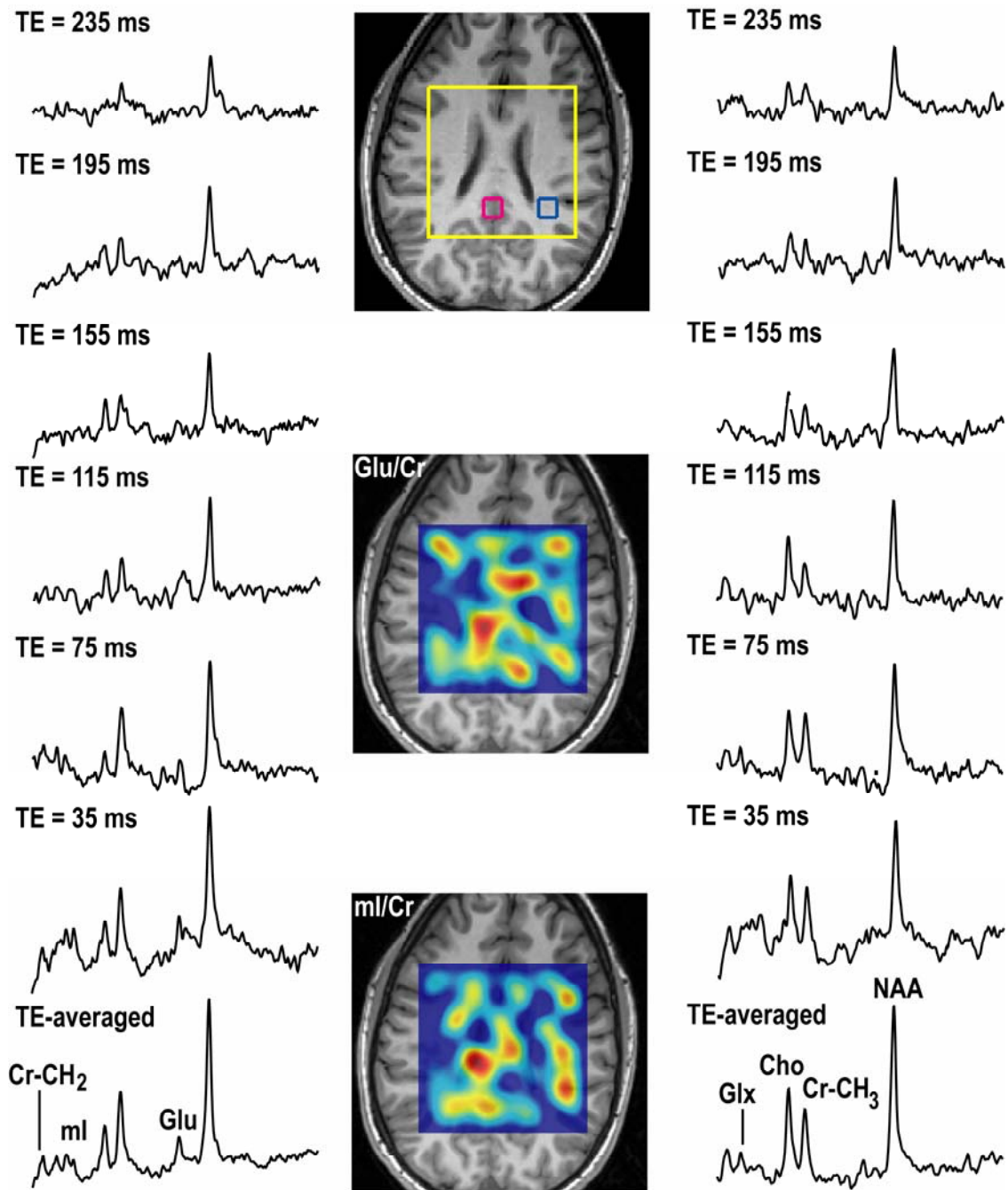


Figure 5.7 3D J-resolved MRSI acquired from a volunteer. The TE-averaged spectra from two voxels, grey matter and white matter, were plotted along each individual echo spectra. The metabolic maps were quantified using LCModel without corrections of relaxation time and plotted with the range between 0 and 2.20 for Glu/Cr and between 0 and 1.90 for ml/Cr.

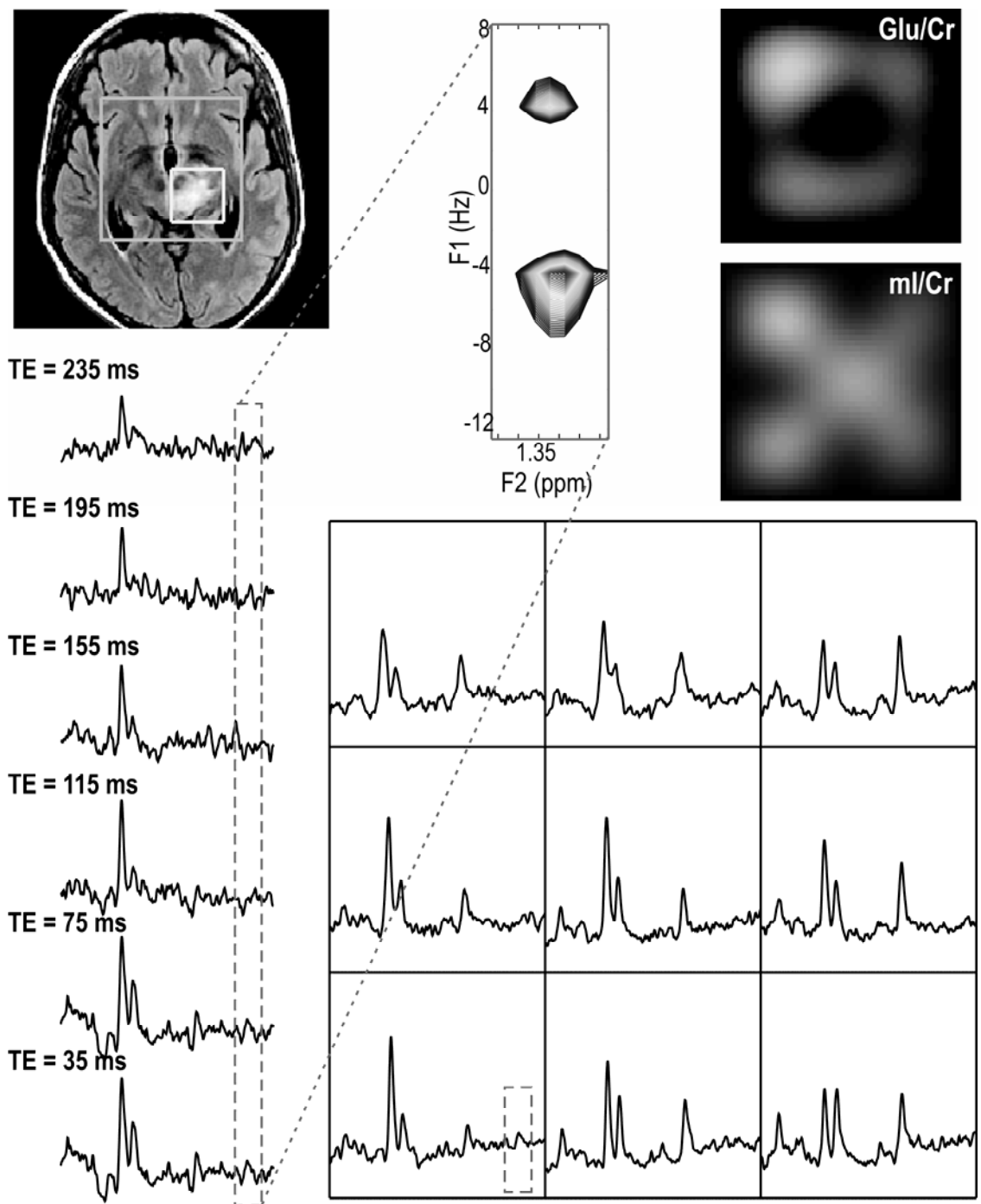


Figure 5.8 3D J-resolved MRSI acquired from a patient with glioma. The TE-averaged spectra corresponds to the location in the T₂-weighted image. The 2D spectrum with the expanded region centered at 1.35 ppm extracted from the labeled voxel, which was compared with six individual echo time spectra. The metabolic maps of Glu/Cr and ml/Cr are plotted with the same scale as in the Figure 5.7.

Figure 5.8 shows the TE-averaged spectra corresponding to the regions shown on the T₂-weighted MRI image from a glioma patient. The spectra demonstrated good quality, and metabolic ratio maps represented the changes in the corresponding spectra well. The resonances of the Lac methyl group from the tumor could not be observed in the TE-averaged spectra but appeared as cross-peaks in the 2D spectrum. The relative metabolite ratios in patients quantified by LCModel without corrections of relaxation time compared with those in volunteers are shown in Table 5.1. As expected, the levels of Cho/Cr and mI/Cr increased in the tumor lesions compared to the levels in the normal tissues, and NAA/Cr decreased.

Table 5.1 Relative metabolite levels quantified by LCModel without corrections for relaxation time from six normal volunteers and four patients with primary brain tumors. Numbers refers to mean±SD.

	Cho/Cr	NAA/Cr	Glu/Cr	Glx/Cr	mI/Cr
WM	0.34±0.08	2.17±0.50	1.77±0.68	2.33±1.29	1.48±0.53
GM	0.26±0.06	1.62±0.45	1.91±0.75	2.69±1.34	1.38±0.46
Patient A	0.57±0.16	1.14±0.33	1.47±0.57	2.12±1.36	1.61±0.66
Patient B-D	0.40±0.10	1.21±0.39	1.63±0.68	2.97±3.01	1.57±0.60
Total T₂ lesions	0.45±0.14	1.20±0.38	1.58±0.64	2.74±2.67	1.58±0.62

Figure 5.9 illustrates the T₂ maps of Cho, Cr and NAA from a volunteer. The T₂ values of Cho were shown to be statistically significantly higher in grey matter (P=0.004) relative to white matter, while those of NAA were significantly higher in the white matter (P<0.001). Compared with Cho and NAA, the T₂ values of Cr showed less tissue differences. Table 5.2 shows the T₂ values of Cho, Cr and NAA in the segmented white matter, grey matter from the volunteers and T₂ hyperintensity lesions from patients. Consistent with previous studies [13], the T₂ relaxation times of normal brain metabolites were different from the T₂ values in gliomas. The T₂ values of Cho and Cr in the lesions

were statistically significantly longer than those in normal white matter ($P < 0.005$), while T_2 values of NAA were shorter, although without statistical significance.

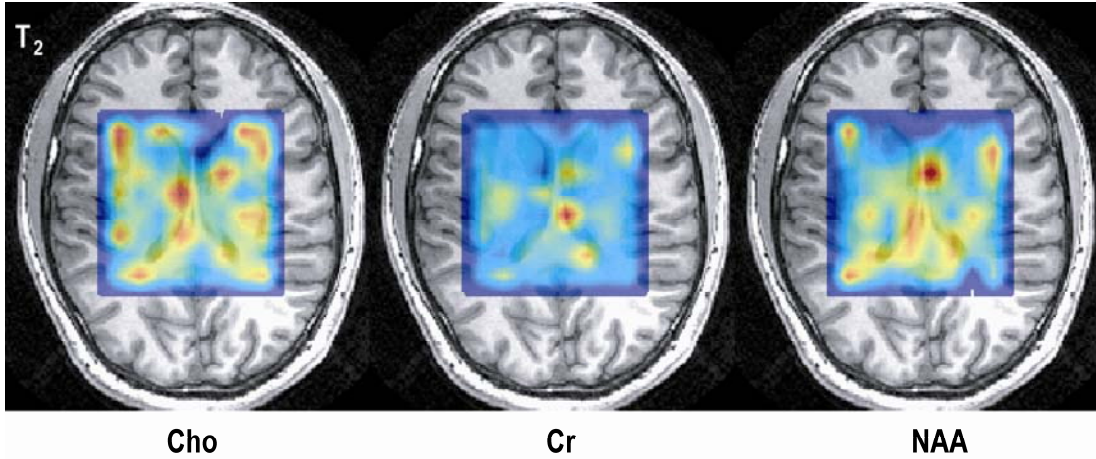


Figure 5.9 T_2 maps of Cho, Cr and NAA from a volunteer

Table 5.2 T_2 relaxation times of metabolites (ms) from six volunteers and four primary brain tumor patients. Numbers refers to mean \pm SD (median), and N represents the number of voxel involved in the group.

	Cho	Cr	NAA
WM	205 \pm 77 (192) N=217	148 \pm 35 (145) N=219	314 \pm 105 (299) N=298
GM	265 \pm 81 (248) N=12	155 \pm 41 (142) N=27	221 \pm 66 (216) N=39
Total T_2 lesions	245 \pm 94 (222) N=83	174 \pm 50 (166) N=46	322 \pm 160 (260) N=59

5.4 Discussion

A J-resolved MRSI sequence with localization in three spatial dimensions was implemented within a clinically feasible scan time at 3 T (23 min). Post-processing methods were applied for interpretation and quantification of metabolites from these

spectra for normal volunteer and patients with brain tumor. This technique allows simultaneous quantification of Glu independent of Gln, visualization and quantification of lactate methyl protons in 2D spectra, as well as evaluation of changes of metabolite T_2 relaxation time, on a voxel by voxel (1 cm^3 resolution) basis in a large three dimensional volume, typically $\sim 256 \text{ cm}^3$.

J-resolved spectroscopy is one of the simplest 2D sequences, which allows separation of metabolites based on both chemical shift and J-modulation. A major drawback of this acquisition is its relatively long acquisition time due to numerous t_1 increments required for wide bandwidth in the F_1 dimension to avoid aliasing and fine spectral resolution for the separation of J-coupling resonances. Previously developed measurements based upon TE-averaged PRESS, offered effective separation of the Glu signal from NAA and Gln at 3 T by canceling the side bands of triplets or quintuplets [65], as well as suppressing the doublet, such as from the methyl group of Lac. To implement this technique in three spatial dimensions within a feasible total scan time, relatively few points in t_1 are required. The t_1 values used in this study were modified both to optimize for detection of Glu in the TE-averaged spectra and to visualize Lac in the 2D spectrum, in addition to using the fewest number of t_1 points that allowed coverage in three spatial dimensions. Even spacing of 40 ms of echo time offers the possibility to visualize the Lac in the 2D spectrum, while more echo time points can provide more accurate T_2 fitting. If only the TE-averaged spectra are of interest, the last echo time spectra can be omitted. The bandwidth in the F_1 domain was small ($\sim 25 \text{ Hz}$) but large enough for the separation of methyl groups of Lac that have a spectral resolution of $\sim 4.17 \text{ Hz}$.

The incorporation of the flyback echo-planar gradient readout scheme [81] was necessary to acquire the J-resolved MRSI data in human studies because it speeds up the data acquisition (23 min). The slight disadvantage of this method is the 12-22% loss in SNR per unit time for the flyback MRSI as compared with the conventional MRSI [81]. In this case, the fast acquisition was critical to acquire the patient data and the SNR obtained from the in vivo data was adequate for quantification of the metabolites targeted in our study. Since sixteen spatial encodings are achieved in the flyback readout at 1 cm spatial resolution (16 cm FOV), aliasing from subcutaneous lipid into the region of interest can be eliminated along this direction (R/L). One of the potential limitations of this technique is the need to trade off spectral bandwidth with spatial resolution and sampling efficiency. With the gradient system available on our clinical system, at spatial resolution of 1cm^3 , the spectral bandwidth for the waveform designed for this study was 988 Hz, which was large enough to cover the metabolites of interest in the brain. Although the total acquisition time was shortened, there still could be some motion artifacts. The multiple-echoes were chosen to be the inner loop while the phase encoding steps were chosen to be the outer loop in order to minimize errors between echo times, but some spatial distortions may still exist and would be reflected as a smearing in the spatial domain.

Compared to short echo MRSI data, the TE-averaged spectra have less contamination from macromolecules and offer unobstructed Glu, which allows more accurate quantification. The simplification of spectra is at the cost of generating a large dataset, which complicates the post-processing and may be time-consuming or require parallel processing. In this study, only the TE-averaged spectra ($F_1 = 0$ Hz) were

quantified using LCModel [29] instead of using two-dimensional fitting, such as ProFit [82], which may further improve quantitative accuracy. The methyl group of Lac was visualized in the 2D spectra and could also be quantified from the spectra extracted from the 2D spectra at $J = \pm 4.17$ Hz.

Estimates of reproducibility for Cho, Cr and NAA demonstrated excellent results in phantoms, 4% for Cho, 5% for Cr, 6% for NAA and 9% for Glu. These CV values were calculated based on a voxel-by-voxel basis using the peak heights of metabolites. The estimates for Cho, Cr and NAA in vivo were 15%, 16% and 12%, respectively, slightly higher than those in the phantoms. Registration of the position of the PRESS localization volume between two scans [83] may help to improve these results. Although the TE-averaged spectra offered a single peak for Glu and less macromolecular contamination, it was possible that Glu was overestimated because of the inclusion of the short echo data in the TE-averaged spectra. The relatively large CV for Glu suggests that baseline fitting is still necessary for quantifying the TE-averaged spectra.

Ratios of relative metabolite levels without corrections of relaxation time were estimated in the regions of normal grey matter and white matter from volunteers and T_2 hyperintense lesions from gliomas. As expected, the ratio of Glu/Cr was slightly higher in the grey matter, while ml/Cr was higher in the white matter due to the Cr being higher in grey matter. The ratios of mean metabolites for Glu and ml were higher in the grey matter, which is consistent with a previous study [80]. Data from three GBM patients showed that Glx/Cr was increased in the T_2 hyperintense lesions and Glu/Cr was reduced, which suggests an increase of Gln in these patients. These in vivo studies demonstrated good quality and are extremely promising.

The T_2 relaxation times of Cho, Cr and NAA were also estimated from these 3D data. The small variances obtained from the phantom suggested that the procedure used to estimate T_2 values was reliable. The mean T_2 values of metabolites were similar to prior studies [72], and the differences in T_2 values between normal white matter and T_2 hyperintensity lesions were consistent with previous work [13]. This may offer a new index for characterizing tumors.

In conclusion, phantoms and in vivo experiments showed that the 2D J-resolved approach was successful in detecting unobstructed metabolite peaks corresponding to Cho, Cr, NAA, mI, Glu and Lac from the simplified spectra along with the flat baseline, and simultaneously allowed estimation of T_2 values of the singlets. The SNR of the 2D J-resolved 3D MRSI performed on the human clinical 3 T scanner was able to provide excellent spatial and spectral resolution within the human brain. After establishing procedures for the acquisition, reconstruction and quantification of 2D J-resolved PRESS MRSI with three spatial dimensions, this methodology can be incorporated into protocols being used to evaluate patients with glioma and may provide improved characterization of the tumors.

Chapter 6: Proton spectroscopy of human brain at 3 T and 7 T comparing of signal-to-noise ratios, spectral linewidths and relaxation times

This chapter assesses the benefits of a 7 T scanner for acquiring proton spectra from the brains of volunteers with the concerns of the effects of relaxation times, susceptibility and signal-to-noise ratio (SNR).

6.1 Rationale

With the availability of the improved hardware and techniques, in vivo single-voxel ^1H -MRS and multi-voxel magnetic resonance spectroscopic imaging (MRSI) can offer new possibilities at a field strength of 7 T. This has the potential of providing higher SNR and/or improved spectral resolution. Recent applications have involved animals [84-86], healthy volunteers [87-91] and brain tumor patients [92].

While higher field could provide more reliable quantification and improved detection of metabolites, it also introduces complications in terms of larger chemical shift artifact, increased susceptibility and differences in longitudinal and transverse relaxation times of metabolites. The question arises as to how much these effects would compromise the anticipated increase of field strength in the data. New pulse sequences have been developed and designed for high field to reduce chemical shift artifact and specific absorption rate (SAR) [89, 93], and optimized high-order shimming and improved

performance of the gradient system are also imperative for the spectral acquisition. The constraints of acquisition time and relative long echo time mean that spectral signals are usually not allowed to be fully relaxed. This means that T_1 and T_2 values are required to obtain absolute metabolite concentrations, and that they may have significant effects on SNR. T_2 values also play an important role on spectral resolution since the linewidth of peak is inversely proportional to T_2^* . The field-dependent trends of the T_1 and the T_2 relaxation times of metabolites has been demonstrated in a rat brain study [86], but they have been fewer studies concerning the comparisons of relaxation times at the two field strengths for the human brains.

This section aims to estimate the T_1 and T_2 relaxation times of Cho, Cr and NAA at both 3 T and 7 T, to evaluate the effects of relaxation times in the long echo time acquisition, to examine the differences in SNR between 3 T and 7 T and to investigate how the acquisition parameters influence the quality of the spectra that are obtained.

6.2 Methods

Study Population

Table 6.1 Methodology and population involved in the study.

	T₁ studies	T₂ studies
3 T	TE-averaged spectra (16 steps, TR = 2s) N=8	2D J-resolved spectra (64 steps, TR = 2s) N=10
7 T	Spectral-spatial pulse (TE/TR = 90/2000 ms) N=8	2D J-resolved spectra (48 steps, TR = 2s) N=12

N=number of volunteer.

Twenty-one volunteers (eleven males and ten females) were recruited in the study. The volume of interest (VOI) with the voxel size of 8 cm^3 was localized in the parietal white matter. The details are shown in Table 6.1.

MR Data

All the empirical studies were performed using an 8-channel receive-only phased-array coil on a 3 T GE Signa scanner running Excite software (GE Healthcare Technologies, Waukesha, WI) and a commercially available 8-channel array and a volume transmit head coil (NOVA Medical, Wilmington, MA) on a 7 T GE scanner. The MR data included the acquisition of anatomical and spectra data.

Anatomical MR images that were acquired included T_1 -weighted sagittal scout images (TR/TE = 70/2 ms at 3 T and TR/TE = 5/1 ms at 7 T), T_1 -weighted spoiled gradient echo (SPGR) images (TR/TE = 26/3 ms) at 3 T, and T_2/T_2^* -weighted gradient recalled echo (GRE) (TR/TE = 250/11 ms) at 7 T.

2D J-resolved point resolved spectral selection (PRESS) spectra were utilized to measure T_2 relaxation of metabolites at both 3 T and 7 T. The t_1 was incremented from 35 ms to 192.5 ms in 64 steps with an increment of 2.5 ms at 3 T [66], while the spectra were acquired with 48 steps with an increment time 5 ms starting at TE of 35 ms at 7 T. With a TR of 2 s and a number of excitations (NEX) of 2, the total acquisition time was ~ 5 minutes at 3 T and ~ 4 minutes at 7 T. An overpress factor of 1.2 at 3 T [12] and 1.4 at 7 T were utilized to reduce chemical shift artifact, and very selective suppression (VSS) pulses [27] of 40 mm width were prescribed around the prescribed volume for outer volume suppression at both field strengths. The manufacturer's linear autoshim procedure was applied at 3 T, and higher-order shimming using a program based on B_0 field map

that was calculated by software developed in house using the “Reconstruction of Multichannel Phase” (ROMP) [94] method was performed at 7 T.

For T_1 studies at 3 T, the TE-averaged PRESS data was obtained with 16 steps and an increment time of 10 ms at TR=1 s with NEX=4, TR=2 s with NEX=4 and TR=8 s with NEX=2, respectively [66]. At 7 T, the custom-designed spectral-spatial pulses [93] with improved B1 insensitivity and greatly reduced chemical shift artifact were used with a TE of 90 ms at TR=2 s, 4 s and 10 s and NEX=1.

All the spectral data were acquired with 2048 spectral points, and 5000 Hz spectral width at both scanners for T_1 and T_2 studies. To obtain estimates of coil sensitivities for the combination of the 8-channel data, unsuppressed water spectra were acquired at an echo time of 35 ms with each of the PRESS spectra at 3 T, and proton density-weighted GRE images were acquired using the manufacturer-provided parallel imaging calibration sequence (TR/TE=100/1 ms) at 7 T.

Postprocessing and Analysis

Post-processing was applied on a single SunBlade 1000 Workstation (Sun Microsystems, Santa Clara, CA). Eight-channel data were combined in the time-domain using the unsuppressed water signal [56] at 3 T, and using in-house developed software which utilized the theory based on a sensitivity encoding (SENSE) reconstruction with a reduction factor (R) of 1.0 as described in a previous article [12] at 7 T. The spectral data were apodized by a 4 Hz Lorentzian filter at both 3 T and 7 T, and then spectra were processed with a Fast Fourier Transform (FFT). The data was quantified using a previously published methodology [28, 66].

To calculate the T_2 values, the peak heights of Cho at 3.22 ppm, Cr-CH₃ at 3.02 ppm and NAA at 2.02 ppm were extracted from the spectra fitted to a mono-exponential function using the SAGE software packageTM (General Electric, Milwaukee). At 3 T, the fitting started from TE of 55 ms to 192.5 ms, a total of 56 spectra, to reduce the contamination of macromolecules and/or J-coupled multiplets. The T_2 for 7 T was estimated from TE of 55 ms to the spectra with SNR just smaller than 2*noise, a minimum of 22 spectra. The NAA intensities were fitted from 55 ms to 270 ms (44 spectra). In addition, only the T_2 fits with variances of the fit residue smaller than 10% were included in the analysis.

For the T_1 studies at 3 T, the data acquired with J-resolved PRESS were firstly averaged in the t1 dimension and then the signal intensities were quantified and normalized for the NEX before the fitting. The T_1 values were calculated from partial T_1 saturation using a two-parameter least-square fitting routine to Equation 4.1. The effective TE was 110 ms at 3 T and 90 ms at 7 T, respectively.

To compare the SNR and linewidth of spectra between 3 T and 7 T, the TE-averaged spectra was generated using TE starting from 35 ms to 190 ms, spacing of 5 ms at both field strength, a total of 32 echoes. The peak parameters of the metabolites were computed automatically within the excited voxel using in-house software [28]. The SNR of individual metabolites were estimated by dividing the peak heights of Cho, Cr and NAA, by the standard deviation of the noise from the peak-free region at the right end of the spectrum [28]. The effects of differences in T_2 between 3 T and 7 T was corrected by multiplying the estimated SNR ratios 7 T over 3 T for Cho, Cr and NAA by a factor,

$$f_{T_2} = \exp(-TE / T_{2(3T)}) / \exp(-TE / T_{2(7T)}) \quad (6.1)$$

while the effective TE is 112.5 ms, and T₁ correction factor was

$$f_{T_1} = \frac{1 - 2 \exp[-(TR - TE / 2) / T_{1(3T)}] + \exp(-TR / T_{1(3T)})}{1 - 2 \exp[-(TR - TR / 2) / T_{1(7T)}] + \exp(-TR / T_{1(7T)})} \quad (6.2)$$

Statistics

Nonparametric Wilcoxon rank sum tests were applied to evaluate differences in SNR, T₁ and T₂ relaxation times between 3 T and 7 T with a P value of 0.05 being considered significant.

6.3 Results

An example of the 2D J-resolved data from volunteers acquired at 3 T and 7 T is shown in Figure 6.1. Note that the spectra are scaled by the estimated noise in each dataset and plotted with the same spectral resolution in parts per million (PPM). Compared to the 3 T data, the 7 T spectra demonstrated higher SNR. Along with the increase of the echo time, the signal intensities of Cho, Cr and NAA decay at a faster rate at 7 T compared with the data set from 3 T.

Table 6.2 T₁ and T₂ relaxation values of Cho, Cr and NAA at 3 T and 7 T (mean±SD).

	T ₁ (s)			T ₂ (ms)		
	Cho	Cr	NAA	Cho	Cr	NAA
3 T	1.06±0.11	1.38±0.13	1.38±0.13	170±18 ^b	151±15	262±37
7 T	1.11±0.20 ^a	1.75±0.19	1.63±0.15	131±16	121±12	170±11
P		0.002	0.003	<0.001	<0.001	<0.001

^a N=5. Three data points were excluded due to poor water suppression.

^b N=9. One data point was excluded due to variance of the fit residue larger than 10%.

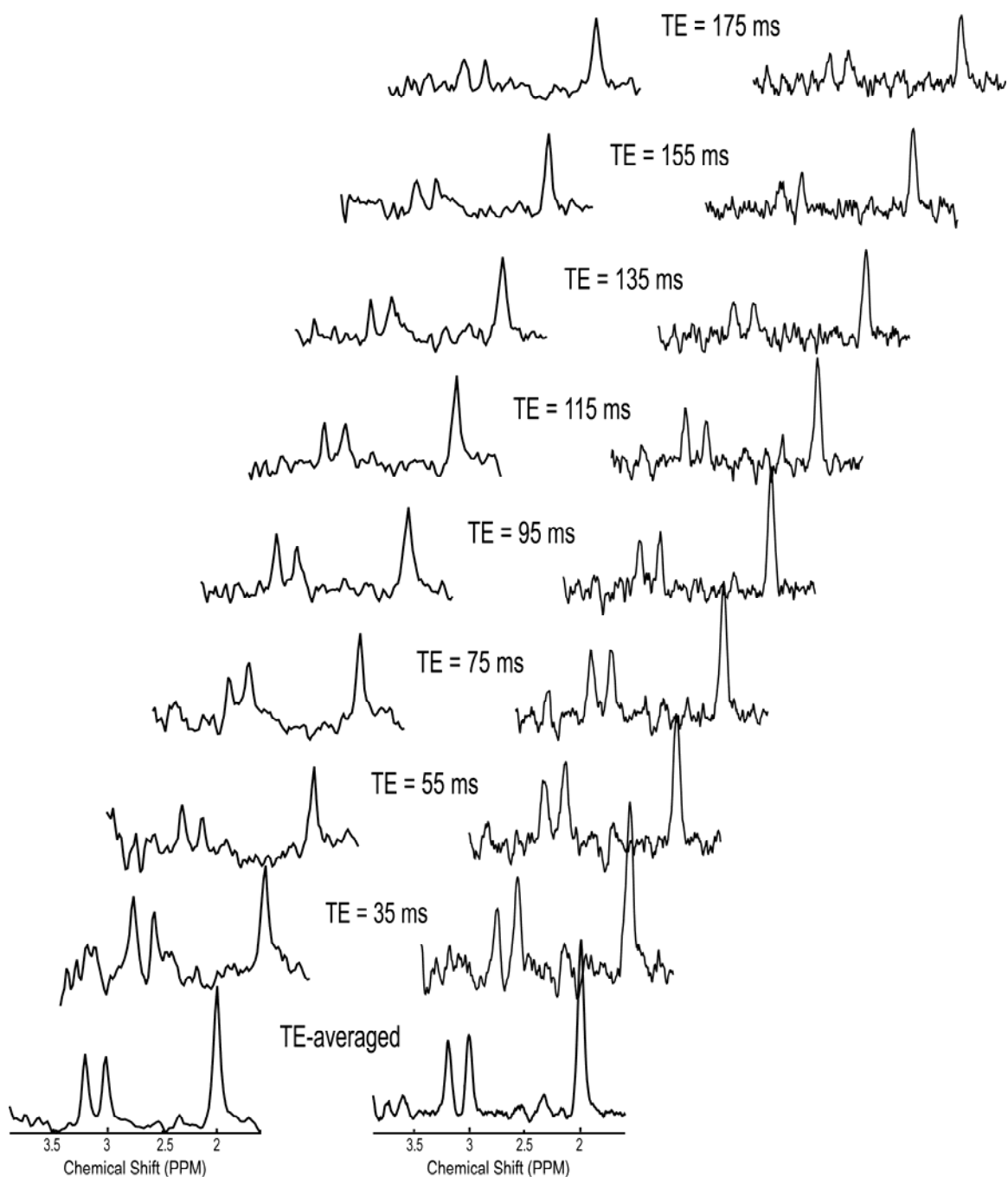


Figure 6.1 2D J-resolved spectra acquired at 3 T (left) and 7 T (right). The spectra were displayed with the same PPM scale, and the vertical scales of all the spectra were normalized to the noise level of the different spectra. Note that the scale between individual echo spectra and the TE-averaged spectra were different, with the TE-averaged spectra scaled up for better visualization.

Figure 6.2 illustrates an example of T_2 fitting using the metabolite peak heights from a volunteer at 7 T, and meanwhile, the T_1 effects and calculation at 7 T is shown in Figure 6.3. As demonstrated in the figures, the data points for the estimations of the T_1 and T_2 values converged to the fitting curve well. The T_1 and T_2 relaxation values of Cho, Cr and NAA at both 3 T and 7 T are given in Table 6.2. As expected, the T_1 values of metabolites increased at 7 T relative to those at 3 T while the T_2 values were shorter. Statistical significance was found for both the T_1 and T_2 relaxation values between 3 T and 7 T for Cho, Cr and NAA with $P < 0.005$ except for the T_1 value of Cho which was relatively longer at 7 T but not statistically significant.

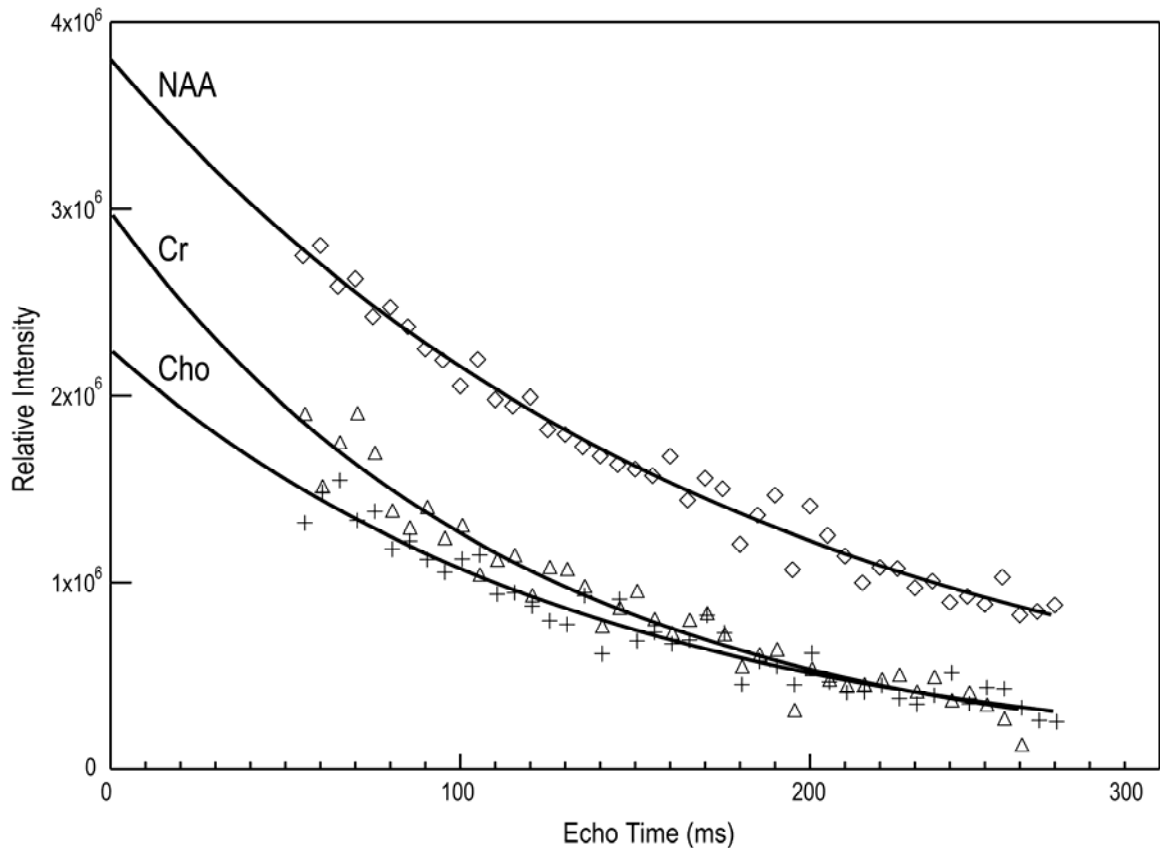


Figure 6.2 T_2 fits for Cho, Cr and NAA data from a volunteer acquired at 7 T using mono-exponential function.

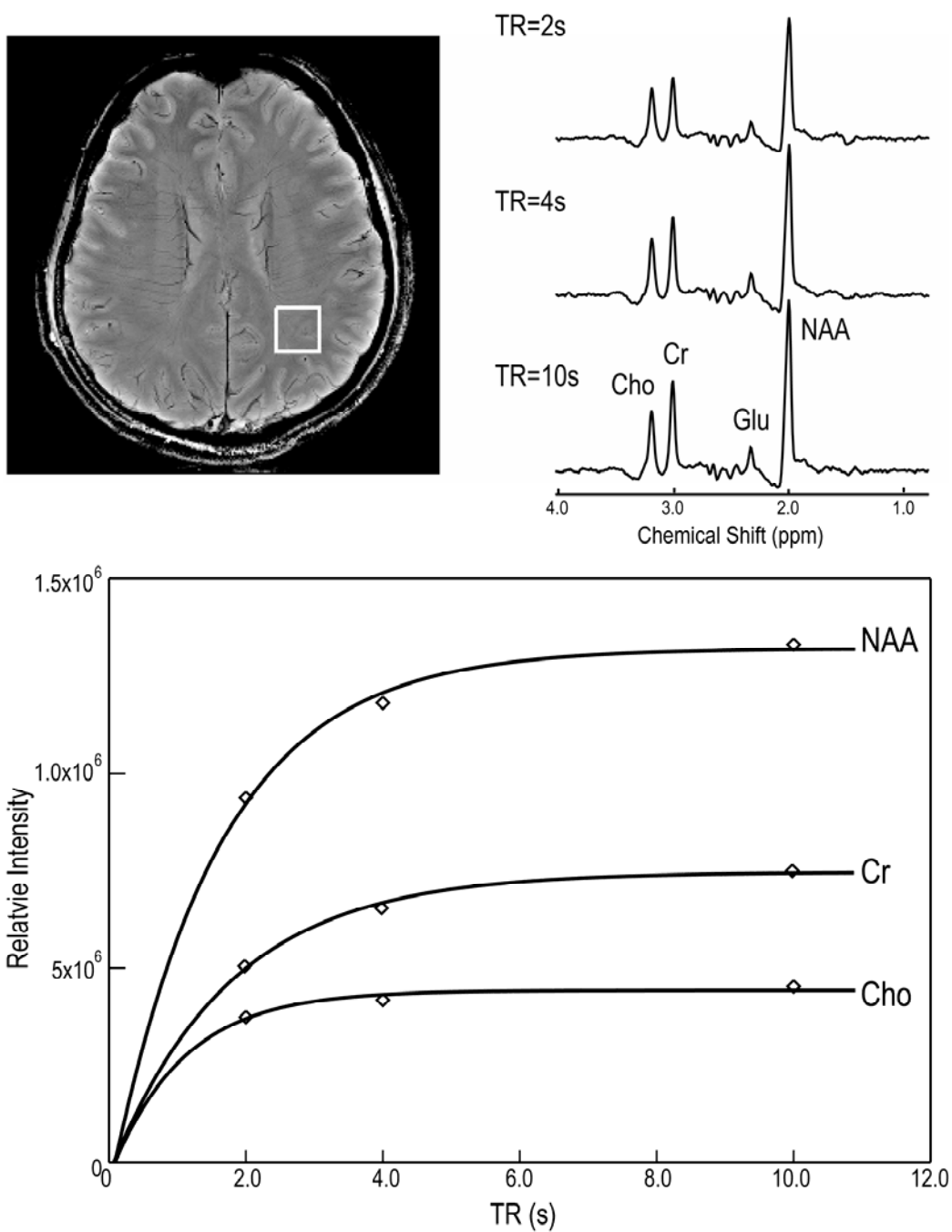


Figure 6.3 Representative T_1 -dependent spectra acquired using spectral-spatial pulse at TE of 90 ms (right) and the corresponding voxel location (top left) from a volunteer. The peak heights of metabolites were used to estimate the T_1 values for Cho, Cr and NAA (bottom).

When corrected for filtering, the estimated linewidths for Cho, Cr and NAA were 4.8 ± 0.7 Hz, 6.3 ± 0.6 Hz and 6.7 ± 0.4 Hz at 3 T, and at 7 T were 19.5 ± 3.6 Hz, 21.0 ± 3.9 Hz and 20.7 ± 3.0 Hz (values expressed as mean \pm S.D.) in the TE-averaged spectra (32 echoes). When expressed in terms of PPM, the ratios of linewidths at 7 T relative to 3 T were 1.74, 1.43 and 1.32. The estimated linewidths in the spectra acquired with spectral-spatial pulses and TE of 90 ms at 7 T were much narrower, namely 11.2 ± 5.2 Hz, 11.9 ± 3.5 Hz and 16.6 ± 4.0 Hz for Cho, Cr and NAA, respectively. There were slightly better than those at 3 T in terms of PPM.

Table 6.3 SNRs of metabolites at 3 T and 7 T (mean \pm SD). The SNR ratios of Cho, Cr and NAA between 7 T and 3 T from the TE-averaged spectra (32 echoes) were compared with the same data after the corrections of relaxation values.

	Cho	Cr	NAA
3 T	61 \pm 11	65 \pm 12	140 \pm 25
7 T	64 \pm 30	76 \pm 34	172 \pm 57
SNR 7 T : 3 T	1.049	1.169	1.229
T ₁ effects	1.017	1.130	1.087
T ₂ effects	1.218	1.203	1.262
7 T : 3 T	1.30	1.59	1.69

The SNRs of metabolites from the TE-averaged spectra are given in Table 6.3. Only 5%-23% were gained for the SNR at 7 T relative to that at 3 T. The effective TE of the TE-averaged spectra was 112.5 ms and the TR was 2 s. Since statistical significance of relaxation values were found between 3 T and 7 T as shown above, the corrections for relaxation times for those acquired with long TE and short TR are imperative. After the corrections of the effects of T₁ and T₂ relaxation values, SNR ratios between 7 T and 3 T were raised by an average of 1.53. Although this was less than the theoretical values, 2.33, the differences could be explained by the large linewidths that were observed at 7 T.

After multiplying the SNR ratio to the linewidth differences in PPM, the average SNR ratios would be 2.25. The SNR of NAA in the spectra acquired with spectral-spatial pulses from volunteers with a TR of 2 s was 206 ± 46 , and after corrections of T_2 difference between two acquisitions, TE=112.5 ms vs. TE=90 ms, it was 5% higher than that in the TE-averaged spectra (32 echoes).

6.4 Discussion

In this study, measurements and quantitative analysis were performed to evaluate the gains due to the increase of field strength from 3 T to 7 T, and to determine the potential factors affecting the in vivo application of MRS at high field. It has been demonstrated that improved SNR at 7 T relative to 3 T could be used to provide data with finer spatial resolution with the same acquisition time or to reduce the total acquisition time.

The spectra in the study were acquired using the standard MRS localization technique, PRESS. Spatial variations in metabolite ratios in 3 D acquisition may occur with band-selective RF pulses. These errors are also dependent on the resonant frequency and will therefore become more prominent as the field strength increases. It has been well demonstrated at 3 T [12], and was reduced by prescribing a PRESS box larger than the region of interest (ROI) (overpress) and to use very selective suppression (VSS) pulses [27] for suppressing the signals arising from beyond the ROI. Another way to minimize this error is to utilize selection pulses with higher spatial bandwidth, such as spectral-spatial pulses [93]. The chemical shift artifact is larger at 7 T. Although this was not fully explored in this project due to the use of a single voxel acquisition, a larger overpress

factor we considered, 1.4, was used. Further studies are necessary to investigate the effects of chemical shift artifact when acquiring 3D MRSI data.

Another issue that we considered was anticipated increase in linewidths due to larger susceptibility artifacts at higher field. The estimated linewidths for Cho, Cr and NAA in TE-averaged spectra were 0.038 ± 0.006 , 0.049 ± 0.005 and 0.053 ± 0.003 ppm, respectively, at 3 T, and were 0.065 ± 0.012 , 0.071 ± 0.013 and 0.069 ± 0.010 , respectively at 7 T. For the spectra acquired spectral-spatial pulses at 7 T they were 0.038 ± 0.017 , 0.040 ± 0.012 and 0.056 ± 0.013 ppm. The linewidths in the TE-averaged spectra at 3 T was close to those reported [12], however, the linewidths in the TE-averaged spectra was worse than those in the spectral-spatial spectra at 7 T. This could be the result of small frequency offsets between spectra from different echo times in the TE-averaged acquisition. Although the spectral-spatial pulses offer slightly narrower spectral linewidth at 7 T than that at 3 T, the longer TE and smaller spectral width (712 Hz) for this RF pulse would limit its application. The larger overpress factor used at 7 T could also bring in inhomogeneities outside of ROI which may also lead to broader linewidths.

Increased SNRs were, on average, 1.15 for the TE-averaged spectra at 7 T versus 3 T, and were 1.53 after the corrections for the differences of relaxation times. The increase in SNR ratio for Cho is the smallest at 7 T relative to 3 T, and the linewidth broadening is also the largest for Cho. Since the Cho peak resonating at 3.22 ppm represents choline, phosphocholine (PC) and glycerophosphocholine (GPC), larger spectral dispersion at high field has the potential to separate different components of Cho, which may be not observable but may result in an increase in the linewidth for Cho peak. After multiplying the linewidth differences between 3 T and 7 T, the SNR ratios raised up to 2.25 on

average, with 2.26 for Cho, 2.27 for Cr and 2.23 for NAA, respectively, which is close to the theoretic value of 2.33. In a previous paper, the authors stated that they were able to achieve a 2-fold improvement in SNR and had much narrower linewidths at 7 T [91]. This suggests that we may be able to obtain improved data by going to a multi-voxel acquisition.

From our study, the T_1 and T_2 relaxation times of metabolites at 3 T were similar to those published [72], and the trend of changes in T_1 and T_2 relaxation values upon the increase of field strengths from 3 T to 7 T are close to the studies reported in the rat brain [86]. The T_1 values of Cr and NAA were anticipated to be significantly longer at 7 T, while the change for Cho is small and not significant compared with those at 3 T. This is consistent with the previous finding in the rat brain [86] and may be due to broadening of Cho at 7 T results in that using peak heights for calculating Cho T_1 value was less sensitive. On the other hand, the T_2 values of all the metabolites were dramatically shortened at 7 T relative to those at 3 T. The longer T_1 relaxation times and shorter T_2 relaxation times mean that metabolite resonances were more saturated at 7 T compared to those at 3 T. This is illustrated in Table 6.3 and suggests that longer TR and shorter TE are obligatory for spectral acquisition at 7 T in order to utilize the SNR gain upon the increase of field strength.

Overall, this study provides valuable preliminary data from normal volunteers at 7 T, which includes the estimation of T_1 and T_2 relaxation times of brain metabolites, and the comparisons of their SNR ratios, linewidth and relaxation times between 3 T and 7 T. These data will be helpful for optimization of the acquisition parameters for future

MRS/MRSI studies at 7 T that may further improve the sensitivity and specificity of this technique.

Chapter 7: Summary

The research being performed during my Ph.D. study has focused on the development, optimization and application of acquisition, post-processing, and quantification methods for in vivo MRS data with the objective of increasing the information that can be obtained from patients with brain tumors using this non-invasive technique in conjunction with conventional MRI. This has included the assessment of advantages in making a transition to new hardware using higher field strength and new radiofrequency coils, implementation of a new proton spectroscopy acquisition method and understanding how metabolite levels differ in tumors relative to normal tissue.

The use of high field strength and new coils has been shown to provide a considerable advantage over conventional hardware for the acquisition of three-dimensional PRESS proton MRSI [12]. The combined effect of using a 3 T MT scanner and an eight-channel radiofrequency coil provided an increase in the SNR of more than 2.33 times the corresponding acquisition at 1.5 T with a quadrature volume head coil. Very selective suppression pulses (VSS) with a thickness of 40 mm and an overpress factor of at least 1.2 were also shown to be required for reducing artifacts due to chemical shift effects and lipid contamination. The increase in SNR that is obtained will be critical for clinical applications of MRSI in patients with brain tumors because it can be used to either decrease acquisition time to the more clinically relevant range of 5-9 minutes or improve the spatial resolution of the metabolic data [95]. The estimated linewidths of metabolites were much narrower at 3 T than those at 1.5 T in the unit of PPM, which

implies improved peak separation despite the presence of surgical cavities and other treatment effects upon using the high-order shimming provided by the manufacturer.

Elevations in levels of choline containing compounds (Cho) and reductions in levels of NAA have been established as markers that distinguish regions of tumor from normal brain tissue. However, the ability to map out the spatial extent of tumor relative to NAWM is dependent upon both the variations in absolute concentrations of metabolites and in degree of T_1 and T_2 weighting. We have studied the differences in relaxation values between for patients with gliomas [13]. Metabolite T_1 relaxation values in gliomas were not significantly different from values in normal white matter. The T_2 of Cho and Cr were statistically significantly longer for Grade IV gliomas than for normal white matter but the T_2 of NAA was similar. These differences were large enough to impact the corrections of metabolite levels for relaxation times with tumor grade in terms of metabolite ratios ($P < 0.001$). The differential increase in T_2 for Cho and Cr relative to NAA means that the ratios of Cho/NAA and Cr/NAA are higher in tumor at longer echo times relative to values in normal appearing brain. Having this information may be useful in defining the acquisition parameters for optimizing contrast between tumor and normal tissue in MRSI data, where limited time is available and only one echo time can be used. The interpretation of such data should take into account that the observed differences in uncorrected metabolite ratios are due to the combination of changes in both relaxation time and metabolite concentrations.

Brain metabolites, such as Glu, Gln and mI, are known to appear in spectra with short echo times, but peak overlap and complex coupling patterns make it difficult to isolate individual components, even at higher field strength. To address this difficulty we

have developed a new data acquisition scheme that can provide a 3-D spatial array of 2D J-resolved PRESS MRSI data [14]. Relatively few points in the t_1 dimension (6 echo times) and a flyback echo-planar trajectory were incorporated in the acquisition to speed up the total acquisition time to be within a clinically feasible range (23 minutes). This approach was successful in detecting unobstructed metabolite peaks corresponding to Cho, Cr, NAA, mI and Glu from the simplified spectra (TE-averaged spectra) because of its relatively flat baseline, visualizing the J cross-peaks from the methyl group of lactate in the 2D spectra, and in simultaneously allowing estimation of T_2 values of the singlet peaks. The SNR of the 2D J-resolved 3D MRSI performed on the human clinical 3 T scanner was able to provide excellent spatial and spectral resolution within the human brain. This new methodology can be incorporated into protocols being used to evaluate patients with glioma and may provide improved characterization of the tumors.

Finally, we have focused on obtaining preliminary data using spectroscopic imaging from normal volunteers at a field strength of 7 T. We have found that brain metabolite SNR was improved at 7 T relative to 3 T, but the increase in SNR observed was less than linear with respect to B_0 , mainly due to the differences in linewidth. This suggests that improved shimming is needed for acquiring these data. Statistical significance was found for the differences in the T_1 and T_2 values of metabolites between 3 T and 7 T except for the Cho T_1 value. This significant difference in relaxation times suggests that longer TR and shorter TE are beneficial for acquiring spectral data at 7 T. The results from this study may be helpful for designing future MRS studies that will further improve the sensitivity and specificity of this technique.

In conclusion, we have explored effects of acquisition parameters, post-processing methods, accurate metabolite quantification and new hardware for MRS in the patients with brain tumors, for the purpose of correlating the molecular levels detected by MRS techniques with the clinical outcome. The results of this dissertation can be utilized to increase the information that can be obtained from patients with brain tumors using MRSI techniques and to improve the accuracy of spectral quantification for addressing tumor characterization.

References

1. *CBTRUS 1998-2002 data*. Central Brain Tumor Registry of the United States, 2005-2006.
2. Fulham, M.J., A. Bizzi, M.J. Dietz, et al., *Mapping of brain tumor metabolites with proton MR spectroscopic imaging: clinical relevance*. *Radiology*, 1992. **185**(3): p. 675-86.
3. Preul, M.C., Z. Caramanos, D.L. Collins, et al., *Accurate, noninvasive diagnosis of human brain tumors by using proton magnetic resonance spectroscopy*. *Nat Med*, 1996. **2**(3): p. 323-5.
4. Nelson, S.J., S. Huhn, D.B. Vigneron, et al., *Volume MRI and MRSI techniques for the quantitation of treatment response in brain tumors: presentation of a detailed case study*. *J Magn Reson Imaging*, 1997. **7**(6): p. 1146-52.
5. Preul, M.C., Z. Caramanos, R. Leblanc, et al., *Using pattern analysis of in vivo proton MRSI data to improve the diagnosis and surgical management of patients with brain tumors*. *NMR Biomed*, 1998. **11**(4-5): p. 192-200.
6. Nelson, S.J., *Multivoxel magnetic resonance spectroscopy of brain tumors*. *Mol Cancer Ther*, 2003. **2**(5): p. 497-507.
7. Pirzkall, A., X. Li, J. Oh, et al., *3D MRSI for resected high-grade gliomas before RT: tumor extent according to metabolic activity in relation to MRI*. *Int J Radiat Oncol Biol Phys*, 2004. **59**(1): p. 126-37.
8. Howe, F.A., S.J. Barton, S.A. Cudlip, et al., *Metabolic profiles of human brain tumors using quantitative in vivo 1H magnetic resonance spectroscopy*. *Magn Reson Med*, 2003. **49**(2): p. 223-32.
9. Isobe, T., A. Matsumura, I. Anno, et al., *Quantification of cerebral metabolites in glioma patients with proton MR spectroscopy using T2 relaxation time correction*. *Magn Reson Imaging*, 2002. **20**(4): p. 343-9.

10. Rijpkema, M., J. Schuurings, Y. van der Meulen, et al., *Characterization of oligodendrogliomas using short echo time 1H MR spectroscopic imaging*. NMR Biomed, 2003. **16**(1): p. 12-8.
11. McKnight, T.R., S.M. Noworolski, D.B. Vigneron, et al., *An automated technique for the quantitative assessment of 3D-MRSI data from patients with glioma*. J Magn Reson Imaging, 2001. **13**(2): p. 167-77.
12. Li, Y., J.A. Osorio, E. Ozturk-Isik, et al., *Considerations in applying 3D PRESS H-1 brain MRSI with an eight-channel phased-array coil at 3 T*. Magn Reson Imaging, 2006. **24**(10): p. 1295-302.
13. Li, Y., R. Srinivasan, S. Chang, et al. *Characterization of high grade gliomas using TE-averaged PRESS at 3 T*. In: Proceedings of the 14th Annual Meeting of ISMRM, Seattle, WA, USA, 2006. (Abstract 1778).
14. Li, Y., A.P. Chen, J.C. Crane, et al., *Three-dimensional J-resolved H-1 magnetic resonance spectroscopic imaging of volunteers and patients with brain tumors at 3T*. Magn Reson Med, 2007. **58**(5): p. 886-92.
15. Li, Y., D. Xu, A.P. Chen, et al. *Proton Spectroscopy of human brain at 3T and 7T: signal-to-noise ratio, spectral linewidth and relaxation times*. In: Proceedings of the 16th Annual Meeting of ISMRM, Toronto, ON, Canada, 2008. (Abstract 411).
16. Kleihues, P., D.N. Louis, B.W. Scheithauer, et al., *The WHO classification of tumors of the nervous system*. J Neuropathol Exp Neurol, 2002. **61**(3): p. 215-25; discussion 226-9.
17. Dumas-Duport, C., B. Scheithauer, J. O'Fallon, et al., *Grading of astrocytomas. A simple and reproducible method*. Cancer, 1988. **62**(10): p. 2152-65.
18. Stupp, R., W.P. Mason, M.J. van den Bent, et al., *Radiotherapy plus concomitant and adjuvant temozolomide for glioblastoma*. N Engl J Med, 2005. **352**(10): p. 987-96.
19. Bernstein, M.A., K.F. King, and Z.J. Zhou, *Handbook of MRI pulse sequences*. 2004, Burlington, MA: Elsevier Academic Press. xxii, 1017 p.

20. Oh, J., S. Cha, A.H. Aiken, et al., *Quantitative apparent diffusion coefficients and T2 relaxation times in characterizing contrast enhancing brain tumors and regions of peritumoral edema*. J Magn Reson Imaging, 2005. **21**(6): p. 701-8.
21. Bottomley, P.A., *Spatial localization in NMR spectroscopy in vivo*. Ann N Y Acad Sci, 1987. **508**: p. 333-48.
22. Haase, A., J. Frahm, W. Hanicke, et al., *1H NMR chemical shift selective (CHESS) imaging*. Phys Med Biol, 1985. **30**(4): p. 341-4.
23. Ernst, T. and J. Hennig, *Improved water suppression for localized in vivo 1H spectroscopy*. J Magn Reson B, 1995. **106**(2): p. 181-6.
24. Star-Lack, J., S.J. Nelson, J. Kurhanewicz, et al., *Improved water and lipid suppression for 3D PRESS CSI using RF band selective inversion with gradient dephasing (BASING)*. Magn Reson Med, 1997. **38**(2): p. 311-21.
25. Star-Lack, J., D.B. Vigneron, J. Pauly, et al., *Improved solvent suppression and increased spatial excitation bandwidths for three-dimensional PRESS CSI using phase-compensating spectral/spatial spin-echo pulses*. J Magn Reson Imaging, 1997. **7**(4): p. 745-57.
26. Duyn, J.H., J. Gillen, G. Sobering, et al., *Multisection proton MR spectroscopic imaging of the brain*. Radiology, 1993. **188**(1): p. 277-82.
27. Tran, T.K., D.B. Vigneron, N. Sailasuta, et al., *Very selective suppression pulses for clinical MRSI studies of brain and prostate cancer*. Magn Reson Med, 2000. **43**(1): p. 23-33.
28. Nelson, S.J., *Analysis of volume MRI and MR spectroscopic imaging data for the evaluation of patients with brain tumors*. Magn Reson Med, 2001. **46**(2): p. 228-39.
29. Provencher, S.W., *Estimation of metabolite concentrations from localized in vivo proton NMR spectra*. Magn Reson Med, 1993. **30**(6): p. 672-9.
30. Ratiney, H., M. Sdika, Y. Coenradie, et al., *Time-domain semi-parametric estimation based on a metabolite basis set*. NMR Biomed, 2005. **18**(1): p. 1-13.

31. Smith, T.A., S. Eccles, M.G. Ormerod, et al., *The phosphocholine and glycerophosphocholine content of an oestrogen-sensitive rat mammary tumour correlates strongly with growth rate*. Br J Cancer, 1991. **64**(5): p. 821-6.
32. Galons, J.P., C. Job, and R.J. Gillies, *Increase of GPC levels in cultured mammalian cells during acidosis. A 31P MR spectroscopy study using a continuous bioreactor system*. Magn Reson Med, 1995. **33**(3): p. 422-6.
33. Usenius, J.P., P. Vainio, J. Hernesniemi, et al., *Choline-containing compounds in human astrocytomas studied by 1H NMR spectroscopy in vivo and in vitro*. J Neurochem, 1994. **63**(4): p. 1538-43.
34. Aboagye, E.O. and Z.M. Bhujwalla, *Malignant transformation alters membrane choline phospholipid metabolism of human mammary epithelial cells*. Cancer Res, 1999. **59**(1): p. 80-4.
35. Baslow, M.H., *N-acetylaspartate in the vertebrate brain: metabolism and function*. Neurochem Res, 2003. **28**(6): p. 941-53.
36. Neale, J.H., R.T. Olszewski, L.M. Gehl, et al., *The neurotransmitter N-acetylaspartylglutamate in models of pain, ALS, diabetic neuropathy, CNS injury and schizophrenia*. Trends Pharmacol Sci, 2005. **26**(9): p. 477-84.
37. Ye, Z.C. and H. Sontheimer, *Glioma cells release excitotoxic concentrations of glutamate*. Cancer Res, 1999. **59**(17): p. 4383-91.
38. Takano, T., J.H. Lin, G. Arcuino, et al., *Glutamate release promotes growth of malignant gliomas*. Nat Med, 2001. **7**(9): p. 1010-5.
39. Mates, J.M., C. Perez-Gomez, I. Nunez de Castro, et al., *Glutamine and its relationship with intracellular redox status, oxidative stress and cell proliferation/death*. Int J Biochem Cell Biol, 2002. **34**(5): p. 439-58.
40. Kofman, O. and R.H. Belmaker, *Ziskind-Somerfeld Research Award 1993. Biochemical, behavioral, and clinical studies of the role of inositol in lithium treatment and depression*. Biol Psychiatry, 1993. **34**(12): p. 839-52.

41. Castillo, M., J.K. Smith, and L. Kwock, *Correlation of myo-inositol levels and grading of cerebral astrocytomas*. AJNR Am J Neuroradiol, 2000. **21**(9): p. 1645-9.
42. Li, X., D.B. Vigneron, S. Cha, et al., *Relationship of MR-derived lactate, mobile lipids, and relative blood volume for gliomas in vivo*. AJNR Am J Neuroradiol, 2005. **26**(4): p. 760-9.
43. Star-Lack, J., D. Spielman, E. Adalsteinsson, et al., *In vivo lactate editing with simultaneous detection of choline, creatine, NAA, and lipid singlets at 1.5 T using PRESS excitation with applications to the study of brain and head and neck tumors*. J Magn Reson, 1998. **133**(2): p. 243-54.
44. Kelley, D.A., L.L. Wald, and J.M. Star-Lack, *Lactate detection at 3T: compensating J coupling effects with BASING*. J Magn Reson Imaging, 1999. **9**(5): p. 732-7.
45. Hattori, N., K. Abe, S. Sakoda, et al., *Proton MR spectroscopic study at 3 Tesla on glutamate/glutamine in Alzheimer's disease*. Neuroreport, 2002. **13**(1): p. 183-6.
46. Gruber, S., V. Mlynarik, and E. Moser, *High-resolution 3D proton spectroscopic imaging of the human brain at 3 T: SNR issues and application for anatomy-matched voxel sizes*. Magn Reson Med, 2003. **49**(2): p. 299-306.
47. Jeun, S.S., M.C. Kim, B.S. Kim, et al., *Assessment of malignancy in gliomas by 3T 1H MR spectroscopy*. Clin Imaging, 2005. **29**(1): p. 10-5.
48. Wellard, R.M., R.S. Briellmann, C. Jennings, et al., *Physiologic variability of single-voxel proton MR spectroscopic measurements at 3T*. AJNR Am J Neuroradiol, 2005. **26**(3): p. 585-90.
49. Barker, P.B., D.O. Hearshen, and M.D. Boska, *Single-voxel proton MRS of the human brain at 1.5T and 3.0T*. Magn Reson Med, 2001. **45**(5): p. 765-9.
50. Gonen, O., S. Gruber, B.S. Li, et al., *Multivoxel 3D proton spectroscopy in the brain at 1.5 versus 3.0 T: signal-to-noise ratio and resolution comparison*. AJNR Am J Neuroradiol, 2001. **22**(9): p. 1727-31.

51. Srinivasan, R., D. Vigneron, N. Sailasuta, et al., *A comparative study of myo-inositol quantification using LCmodel at 1.5 T and 3.0 T with 3 D 1H proton spectroscopic imaging of the human brain*. Magn Reson Imaging, 2004. **22**(4): p. 523-8.
52. Mlynarik, V., S. Gruber, and E. Moser, *Proton T (1) and T (2) relaxation times of human brain metabolites at 3 Tesla*. NMR Biomed, 2001. **14**(5): p. 325-31.
53. Ethofer, T., I. Mader, U. Seeger, et al., *Comparison of longitudinal metabolite relaxation times in different regions of the human brain at 1.5 and 3 Tesla*. Magn Reson Med, 2003. **50**(6): p. 1296-301.
54. Wald, L.L., S.E. Moyher, M.R. Day, et al., *Proton spectroscopic imaging of the human brain using phased array detectors*. Magn Reson Med, 1995. **34**(3): p. 440-5.
55. Nelson, S.J., D.B. Vigneron, J. Star-Lack, et al., *High spatial resolution and speed in MRSI*. NMR Biomed, 1997. **10**(8): p. 411-22.
56. Wright, S.M. and L.L. Wald, *Theory and application of array coils in MR spectroscopy*. NMR Biomed, 1997. **10**(8): p. 394-410.
57. Natt, O., V. Bezkorovaynyy, T. Michaelis, et al., *Use of phased array coils for a determination of absolute metabolite concentrations*. Magn Reson Med, 2005. **53**(1): p. 3-8.
58. Pruessmann, K.P., M. Weiger, M.B. Scheidegger, et al., *SENSE: sensitivity encoding for fast MRI*. Magn Reson Med, 1999. **42**(5): p. 952-62.
59. Zhang, Y., M. Brady, and S. Smith, *Segmentation of brain MR images through a hidden Markov random field model and the expectation-maximization algorithm*. IEEE Trans Med Imaging, 2001. **20**(1): p. 45-57.
60. de Zwart, J.A., P.J. Ledden, P. van Gelderen, et al., *Signal-to-noise ratio and parallel imaging performance of a 16-channel receive-only brain coil array at 3.0 Tesla*. Magn Reson Med, 2004. **51**(1): p. 22-6.

61. Ozturk-Isik, E., J.C. Crane, S. Cha, et al., *Unaliasing lipid contamination for MR spectroscopic imaging of gliomas at 3T using sensitivity encoding (SENSE)*. Magn Reson Med, 2006. **55**(5): p. 1164-9.
62. Thomas, M.A., L.N. Ryner, M.P. Mehta, et al., *Localized 2D J-resolved 1H MR spectroscopy of human brain tumors in vivo*. J Magn Reson Imaging, 1996. **6**(3): p. 453-9.
63. Jensen, J.E., B.D. Frederick, L. Wang, et al., *Two-dimensional, J-resolved spectroscopic imaging of GABA at 4 Tesla in the human brain*. Magn Reson Med, 2005. **54**(4): p. 783-8.
64. Govindaraju, V., K. Young, and A.A. Maudsley, *Proton NMR chemical shifts and coupling constants for brain metabolites*. NMR Biomed, 2000. **13**(3): p. 129-53.
65. Hurd, R., N. Sailasuta, R. Srinivasan, et al., *Measurement of brain glutamate using TE-averaged PRESS at 3T*. Magn Reson Med, 2004. **51**(3): p. 435-40.
66. Srinivasan, R., N. Sailasuta, R. Hurd, et al., *Evidence of elevated glutamate in multiple sclerosis using magnetic resonance spectroscopy at 3 T*. Brain, 2005. **128**(Pt 5): p. 1016-25.
67. Sijens, P.E. and M. Oudkerk, *1H chemical shift imaging characterization of human brain tumor and edema*. Eur Radiol, 2002. **12**(8): p. 2056-61.
68. Knijn, A., R. de Beer, and D. van Ormondt, *Frequency-selective quantification in the time domain*. J Magn Reson, 1992. **97**(2): p. 444-450.
69. Pijnappel, W.W.F., A. van den Boogaart, R. de Beer, et al., *SVD-based quantification of magnetic resonance signals*. J Magn Reson, 1992. **97**(1): p. 122-134.
70. Smith, S.A., T.O. Levante, B.H. Meier, et al., *Computer Simulations in Magnetic Resonance. An Object-Oriented Programming Approach*. J Magn Reson, 1994. **106**(1): p. 75-105.
71. Saraswathy, S., F. Crawford, and S.J. Nelson. *Semi-Automated Segmentation of Brain Tumor Lesions in MR Images*. In: Proceedings of the 14th Annual Meeting of ISMRM, Seattle, WA, USA, 2006. (Abstract 1609).

72. Traber, F., W. Block, R. Lamerichs, et al., *1H metabolite relaxation times at 3.0 tesla: Measurements of T1 and T2 values in normal brain and determination of regional differences in transverse relaxation*. J Magn Reson Imaging, 2004. **19**(5): p. 537-45.
73. Choi, C., N.J. Coupland, P.P. Bhardwaj, et al., *T2 measurement and quantification of glutamate in human brain in vivo*. Magn Reson Med, 2006. **56**(5): p. 971-7.
74. Choi, C., N.J. Coupland, P.P. Bhardwaj, et al., *Measurement of brain glutamate and glutamine by spectrally-selective refocusing at 3 Tesla*. Magn Reson Med, 2006. **55**(5): p. 997-1005.
75. Negendank, W., *Studies of human tumors by MRS: a review*. NMR Biomed, 1992. **5**(5): p. 303-24.
76. Kaminogo, M., H. Ishimaru, M. Morikawa, et al., *Diagnostic potential of short echo time MR spectroscopy of gliomas with single-voxel and point-resolved spatially localised proton spectroscopy of brain*. Neuroradiology, 2001. **43**(5): p. 353-63.
77. Bolan, P.J., L. DelaBarre, E.H. Baker, et al., *Eliminating spurious lipid sidebands in 1H MRS of breast lesions*. Magn Reson Med, 2002. **48**(2): p. 215-22.
78. Kinoshita, Y. and A. Yokota, *Absolute concentrations of metabolites in human brain tumors using in vitro proton magnetic resonance spectroscopy*. NMR Biomed, 1997. **10**(1): p. 2-12.
79. Piani, D., K. Frei, K.Q. Do, et al., *Murine brain macrophages induced NMDA receptor mediated neurotoxicity in vitro by secreting glutamate*. Neurosci Lett, 1991. **133**(2): p. 159-62.
80. Srinivasan, R., C. Cunningham, A. Chen, et al., *TE-Averaged two-dimensional proton spectroscopic imaging of glutamate at 3 T*. Neuroimage, 2006.
81. Cunningham, C.H., D.B. Vigneron, A.P. Chen, et al., *Design of flyback echo-planar readout gradients for magnetic resonance spectroscopic imaging*. Magn Reson Med, 2005. **54**(5): p. 1286-9.

82. Schulte, R.F. and P. Boesiger, *ProFit: two-dimensional prior-knowledge fitting of J-resolved spectra*. NMR Biomed, 2006. **19**(2): p. 255-63.
83. Hancu, I., D.J. Blezek, and M.C. Dumoulin, *Automatic repositioning of single voxels in longitudinal 1H MRS studies*. NMR Biomed, 2005. **18**(6): p. 352-61.
84. Tkac, I., Z. Starcuk, I.Y. Choi, et al., *In vivo 1H NMR spectroscopy of rat brain at 1 ms echo time*. Magn Reson Med, 1999. **41**(4): p. 649-56.
85. Herigault, G., S. Zoula, C. Remy, et al., *Multi-spin-echo J-resolved spectroscopic imaging without water suppression: application to a rat glioma at 7 T*. Magma, 2004. **17**(3-6): p. 140-8.
86. de Graaf, R.A., P.B. Brown, S. McIntyre, et al., *High magnetic field water and metabolite proton T1 and T2 relaxation in rat brain in vivo*. Magn Reson Med, 2006. **56**(2): p. 386-94.
87. Tkac, I., P. Andersen, G. Adriany, et al., *In vivo 1H NMR spectroscopy of the human brain at 7 T*. Magn Reson Med, 2001. **46**(3): p. 451-6.
88. Michaeli, S., M. Garwood, X.H. Zhu, et al., *Proton T2 relaxation study of water, N-acetylaspartate, and creatine in human brain using Hahn and Carr-Purcell spin echoes at 4T and 7T*. Magn Reson Med, 2002. **47**(4): p. 629-33.
89. Tkac, I. and R. Gruetter, *Methodology of 1H NMR Spectroscopy of the Human brain at Very High Magnetic Fields*. AAPL Magn Reson, 2005. **29**(1): p. 139-57.
90. Mangia, S., I. Tkac, R. Gruetter, et al., *Sensitivity of single-voxel 1H-MRS in investigating the metabolism of the activated human visual cortex at 7 T*. Magn Reson Imaging, 2006. **24**(4): p. 343-8.
91. Otazo, R., B. Mueller, K. Ugurbil, et al., *Signal-to-noise ratio and spectral linewidth improvements between 1.5 and 7 Tesla in proton echo-planar spectroscopic imaging*. Magn Reson Med, 2006. **56**(6): p. 1200-10.
92. Nelson, S.J., D. Xu, K.E. Hammond, et al. *3-D MRSI of Patients with Gliomas Using a 7T Whole Body MR Scanner*. In: Proceedings of the 15th Annual Meeting of ISMRM, Berlin, Germany, 2007. 1241.

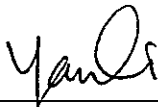
93. Cunningham, C.H., D.B. Vigneron, A.P. Chen, et al. *Spectral-spatial excitation and refocusing for reduced volume mis-registration at 7 Tesla*. In: Proceedings of the 14th Annual Meeting of ISMRM, Seattle, WA, 2006. 72.
94. Hammond, K.E., J.M. Lupo, D.A.C. Kelley, et al. *Comparison of the B₀ Field and Shimming in human brain at 3T and 7T*. In: Proceedings of the 14th Annual Meeting of ISMRM, Seattle, WA, USA, 2006. Abstract 2352.
95. Osorio, J.A., E. Ozturk-Isik, D. Xu, et al., *3D 1H MRSI of brain tumors at 3.0 Tesla using an eight-channel phased-array head coil*. J Magn Reson Imaging, 2007. **26**(1): p. 23-30.

Publishing Agreement

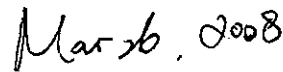
It is the policy of the University to encourage the distribution of all theses and dissertations. Copies of all UCSF theses and dissertations will be routed to the library via the Graduate Division. The library will make all theses and dissertations accessible to the public and will preserve these to the rest of their abilities, in perpetuity.

Please sign the following statement:

I hereby grant permission to the Graduate Division of the University of California, San Francisco to release copies of my thesis or dissertation to the Campus Library to provide access and preservation, in whole or in part, in perpetuity.



Author Signature



Date